The Local Group and its dwarf galaxy members in the standard model of cosmology

by

Azadeh Fattahi
B.Sc., Sharif University of Technology, 2011

A Dissertation Submitted in Partial Fulfillment of the
Requirements for the Degree of

DOCTOR OF PHILOSOPHY

in the Department of Physics and Astronomy

The Local Group and its dwarf galaxy members in the standard model of cosmology

by

Azadeh Fattahi
B.Sc., Sharif University of Technology, 2011

Supervisory Committee

Dr. J. Navarro, Supervisor
(Department of Physics and Astronomy)

Dr. A. McConnachie, Departmental Member
(Department of Physics and Astronomy)

Dr. M. Laca, Outside Member
(Department of Mathematics and Statistics)

ABSTRACT

According to the current cosmological paradigm, “Lambda Cold Dark Matter” (ΛCDM), only $\sim 20\%$ of the gravitating matter in the universe is made up of ordinary (i.e. baryonic) matter, while the rest consists of invisible dark matter (DM) particles, which existence can be inferred from their gravitational influence on baryonic matter and light. Despite the large success of the ΛCDM model in explaining the large scale structure of the Universe and the conditions of the early Universe, there has been debate on whether this model can fully explain the observations of low mass (dwarf) galaxies. The Local Group (LG), which hosts most of the known dwarf galaxies, is a unique laboratory to test the predictions of the ΛCDM model on small scales.

I analyze the kinematics of LG members, including the Milky Way-Andromeda (MW-M31) pair and dwarf galaxies, in order to constrain the mass of the LG. I construct samples of LG analogs from large cosmological N-body simulations, according to the following kinematics constraints: (a) the separation and relative velocity of the MW-M31 pair; (b) the receding velocity of dwarf galaxies in the outskirts of the LG. I find that these constraints yield a median total mass of $2 \times 10^{12}\,\mathrm{M}_\odot$ for the MW and M31, but with a large uncertainty. Based on the mass and the kinematics constraints, I select twelve LG candidates for the APOSTLE simulations project. The APOSTLE project consists of high-resolution cosmological hydrodynamical simulations of the LG candidates, using the EAGLE galaxy formation model. I show that dwarf satellites of MW and M31 analogs in APOSTLE are in good agreement with observations, in terms of number, luminosity and kinematics.

There have been tensions between the observed masses of LG dwarf spheroidals and the predictions of N-body simulations within the ΛCDM framework; simulations tend to over-predict the mass of dwarfs. This problem is known as the “too-big-to-fail” problem. I find that the enclosed mass within the half-light radii of Galactic classical dwarf spheroidals, is in excellent agreement with the simulated satellites in APOSTLE, and that there is no too-big-to-fail problem in APOSTLE simulations. A few factors contribute in solving the problem: (a) the mass of haloes in hydrodynamical simulations are lower compared to their N-body counterparts; (b) stellar mass-halo mass relation in APOSTLE is different than the ones used to argue for the too-big-to-fail problem; (c) number of massive satellites correlates with the virial mass of the host, i.e. MW analogs with virial masses above $\sim 3 \times 10^{12}\,\mathrm{M}_\odot$ would have faced too-big-to-fail problems; (d) uncertainties in observations were underestimated

in previous works.

Stellar mass-halo mass relation in APOSTLE predicts that all isolated dwarf galaxies should live in haloes with maximum circular velocity ($V_{\rm max}$) above $20\,{\rm km\ s^{-1}}$. Satellite galaxies, however, can inhabit lower mass haloes due to tidal stripping which removes mass from the inner regions of satellites as they orbit their hosts. I examine all satellites of the MW and M31, and find that many of them live in haloes less massive than $V_{\rm max} = 20\,{\rm km\ s^{-1}}$. I additionally show that the low mass population is following a different trend in stellar mass-size relation compared to the rest of the satellites or field dwarfs. I use stellar mass-halo mass relation of APOSTLE field galaxies, along with tidal stripping trajectories derived in Penarrubia et al., in order to predict the properties of the progenitors of the LG satellites. According to this prediction, some satellites have lost a significant amount of dark matter as well as stellar mass. Cra II, And XIX, XXI, and XXV have lost 99 per-cent of their stellar mass in the past.

I show that the mass discrepancy-acceleration relation of dwarf galaxies in the LG is at odds with MOdified Newtonian Dynamics (MOND) predictions, whereas tidal stripping can explain the observations very well. I compare observed velocity dispersion of LG satellites with the predicted values by MOND. The observations and MOND predictions are inconsistent, in particular in the regime of ultra faint dwarf galaxies.

Contents

List of Tables

List of Figures

ACKNOWLEDGEMENTS

Many individuals deserve to be named here for their support throughout my graduate school.

First, and foremost, I would like to thank my advisor, Julio Navarro, for his constant support and guidance, for his trust in me, for his patience, and for introducing me to a very interesting project, through which I got the chance to collaborate with amazing scientists. Julio's knowledge, insight, and unique way of thinking taught me so much, beyond words, in the past years. I learned something new, every time I came out of our weekly meetings. I came a long way from being a fresh student with no research experience, to being a researcher; all this was possible because of Julio's guidance and patience. It has been a privilege to work with you and learn from you, Julio! Muchas Gracias!

I also would like to thank:

my supervisory committee members Alan McConnachie and Marcelo Laca. Alan has been my point of reference for any observational questions I have had, and he always responded to them very patiently. Thank you!

Carlos Frenk, who has been almost a co-supervisor to me during my PhD program. I am very grateful for having the chance to work with him through the APOSTLE project. I also would like to acknowledge his support and hospitality during my multiple visits to the Institute for Computational Cosmology in Durham, UK.

Faculty members, Kim Venn, Chris Pritchet, Sara Ellison, and John Willis who were always supportive. I learned a lot from little chats or science discussions we had.

Till Sawala, whose efforts in pushing the APOSTLE project forward were phenomenal. He patiently taught me so many things and responded to my endless questions.

Else Starkenburg, whom I am very grateful for having the chance to work closely with at the start of my graduate program. Her knowledge combined with her warm disposition made my first research experiences very positive. Thank you, Else, for being very approachable!

Jorge Peñarrubia, Alejandro Benítez-Llambay, and Matthieu Schaller. I enjoyed, and learned a lot from, working with them. Jorge, thank you for making a research experience enjoyable and fun! Alejandro and Matthieu, thank you for responding to my questions patiently and thoroughly!

My academic twin, friend, and office-mate, Kyle Oman. I am more than grateful *for sharing 4 years of my PhD with Kyle. He has always been very helpful with his knowledge, reliability and kindess. We shared many laughs and nags, enjoyable science discussions and stressful moments. I also like to thank Marie-Claire for her support and warm presence, and for sending delicious desserts for us.*

Chris Barber, my other academic twin. I am also grateful for sharing my MSc years with Chris. We worked on many assignments and projects together, and shared many laughs. Thank you, Chris, for being willing to have crazy fun chats with me!

All my fellow graduate students whom I had the privilege to meet, and who made my academic life enjoyable.

All my friends in Victoria. The love and support I received from them and the good memories we shared were the reason I enjoyed my life in Victoria. In particular, Sanaz T., Ebad S., Mohammad H., Cate L., Salma E., Nima M., Shadi Ch., Azadeh H., thank you all for brightening my days in Victoria! Behnam R., thank you for your patience and support during my thesis writing days.

I would like to thank my astronomy teachers, Mostafa Bagheri, Masoud Seificar, Shahin Jafarzadeh, Taghi Mirtorabi, Mir Abbas Jalali, Pouria Nazemi, and Pejman Norouzi, whose enjoyable classes are the reason I decided to be an astronomer.

Last, but not least, I would like to thank my wonderful parents, Rahman and Shirin, who are my all-time supporters and do everything they can for me to achieve my dreams and goals. Thanks to my lovely sister, Hengameh, who always sends her love along my way.

DEDICATION

I dedicate my dissertation to my parents, Shirin and Rahman,
to my sister, Tara,
and
to my teachers, Mostafa Bagheri and Shahla Kooshki.

I was able to pursue my passion for astronomy, because of their love and support.

Chapter 1

Introduction

1.1 The standard model of cosmology

1.1.1 Basics

Cosmology is a relatively young science which is only a century old. Observing the expansion of the Universe and revealing the existence of other galaxies, who had been assumed to be nebulae within our own galaxy, and the development of the general theory of relativity, were the key starting points of this field. No major progress, however, was made before 1970s, when "precision cosmology" era began by conducting large redshift surveys of galaxies and measurements of cosmic microwave background radiation (CMB).

Today's standard model of cosmology, known as Λ Cold Dark Matter (ΛCDM), consists of a few key components; (i) the Universe expanded from a very hot and dense state, known as the "hot big bang"; (ii) the expansion of the Universe went through an inflation phase, with a rapid exponential growth, at the very beginning; (iii) the energy budget of the Universe at the present time is divided between normal baryonic matter, non-baryonic cold dark matter (CDM), and dark energy (Λ); and (iv) the hierarchical, or bottom-up, growth of structure that is seeded by quantum fluctuations in the matter density at the end of the inflation era.

Baryonic matter, which makes up gas and stars in the galaxies and intergalactic medium, contributes only ~ 5 per cent in the energy-matter density of the Universe; while dark matter and dark energy contribute ~ 25 and ~ 70 per cent, respectively. Radiation contributes a negligible fraction in the present day, but used to be dominant at the early Universe.

The expansion rate of the Universe at any given time in its history is measured by $H(t) \equiv \dot{a}(t)/a(t)$, where $a(t)$ is the scale factor of the Universe. Evolution of $H(t)$ is given by the Friedmann equation, which can be written as:

$$\frac{H(t)^2}{H_0^2} = \Omega_\Lambda + \frac{1-\Omega_0}{a(t)^2} + \frac{\Omega_m}{a(t)^3} + \frac{\Omega_r}{a(t)^4} \tag{1.1}$$

H_0 is the well known Hubble constant, $H_0 = 100h$ km s^{-1} Mpc^{-1}; Ω_Λ, Ω_m and Ω_r correspond to present day densities of dark energy, matter (baryonic and non-baryonic), and radiation, respectively, in units of the critical density[1]; and $\Omega_0 \equiv \Omega_\Lambda + \Omega_m + \Omega_r$. Ω_0 dictates the geometry of the Universe. The CMB anisotropy measurements, which give the most precise values of Ω's, yield $\Omega_0 = 1$ indicating a flat geometry for the present day Universe.

The hot big bang model was established after the detection of the CMB, the relic from the early hot Universe, by Penzias and Wilson in 1964 (Penzias & Wilson, 1965; Dicke et al., 1965). This radiation had been in equilibrium with ionized matter at the early Universe, before the Universe became cold enough, as the result of expansion, for neutral hydrogen to form. Then, photons decoupled from the matter and started travelling freely in the Universe. We observe this cosmic radiation, almost isotropically, and redshifted to temperature of $T = 3K$ as CMB.

The strength of the ΛCDM framework lies in its ability to explain a few independent observations, with high precision. The cosmological parameters inferred from the CMB temperature anisotropies can explain the Baryonic Acoustic Oscillation observations (see, e.g., Anderson et al., 2014), the shape of the matter power spectrum (e.g. Tegmark et al., 2004), the redshift-luminosity relation (e.g. Riess et al., 1998), the peculiar velocity field of galaxies (Bean et al., 1983; Davis & Nusser, 2016), and the large scale distribution of galaxies (Peebles, 1986; Peacock et al., 2001). Moreover, the baryonic matter density inferred from CMB matches the Big Bang nucleosynthesis (BBN) predictions for formation of light elements at the early Universe (Boesgaard & Steigman, 1985).

On the other hand, the dark matter density inferred from cosmology, i.e. the difference between the total matter density and the baryonic density, turns out to be the exact right amount required to explain the mass discrepancy, or the missing mass problem, found in galaxy clusters and galaxies based on dynamical tracers. I will discuss in more detail the evidence for dark matter and its properties in the next

[1]Critical density, $\rho_{\rm crit}$ is defined as the energy density of a flat Universe, $\rho_{\rm crit} = 3H^2/8\pi G$

sections.

Cosmological numerical simulations enabled the study of the formation of large scale structure and galaxies in ΛCDM and played a crucial role in the establishment of this theory. I will return to numerical simulations in Sec. 1.3.

1.1.2 Evidence for dark matter

The mass discrepancy between the dynamical mass of clusters inferred from the line-of-sight velocities of their galaxy members, and their luminous mass were known since the work of Fritz Zwicky in 1933 on Coma cluster (Zwicky, 1933). The dynamics of cluster members indicated much more mass than expected from the luminosity of galaxies; hence the missing mass problem. This problem got more attention since 1970s when the rotation curves of spiral galaxies were observed out to large enough radii . The rotation curves, which indicate the enclosed mass within the measured radii ($V_{\rm circ} = \sqrt{GM(< r)/r}$), were shown to stay flat beyond the radii of galaxies, instead of falling in as $1/r^2$, pointing out to a significant missing dark mass beyond the observable part of galaxies (Rubin & Ford, 1970; Rogstad & Shostak, 1972; Rubin et al., 1978; Bosma & van der Kruit, 1979)

These observations, along with advancements on the cosmology side for measuring Ω_m and BBN predictions for Ω_b, led to the establishment of non-baryonic dark matter. In more recent years, the gravitational lensing of galaxy clusters (see, Massey et al., 2010, for a review) and the dynamical measurements of dwarf galaxies in the local Universe had been added to the set of observations that confirms the existence of dark matter.

On the other hand, studies in particle physics proposed candidate particles for dark matter such as neutrinos (Bond et al., 1980), axions (Preskill et al., 1983), and supersymmetric particles (Ellis et al., 1984; Blumenthal et al., 1982). Dark matter candidates are divided into three broad categories of hot, warm, and cold, depending on their rest mass which determines their velocities at the early Universe. Light candidates, such as neutrinos, with mass $m_p \sim$ eV fall into the hot dark matter category, while heavier $\sim$ keV and $\sim$ GeV candidates are considered warm and cold, respectively.

Hot dark matter candidates were discarded relatively early. The large free streaming length of these candidates prevents the collapse of small objects in the early universe. Galaxy clusters are the first objects to form in a hot dark matter universe.

Then, smaller haloes and galaxies form later from fragmentation of bigger objects, i.e. top to bottom formation. Distribution of galaxies in such a universe is at odds with observations (White et al., 1983). Warm dark matter candidates were also shown to be inconsistent with observations of the large scale structure of the Universe, unless the particles are not "too warm" (Viel et al., 2008, 2010).

Pressure-less cold dark matter particles, however, will allow formation of small objects at the early universe and imply a hierarchical growth of structure. Studying galaxy and structure formation within the lambda + cold dark matter model has shown that its predictions are in excellent agreement with the observations of the large scale structure probed by large galaxy surveys, and Lyman-α absorption features of distant quasars, known as "Lyman-α forest" (see the review of Springel et al., 2006). read more on

Weakly Interacting Massive Particle or WIMP, is a broad category of candidates, mainly outside of standard model of particles, for cold dark matter particles. Search for these candidates still continues, using particle colliders such as LHC, or recoil detectors built to detect the rare interaction of a specific class of dark matter particles with standard model particles, or indirect detection using the annihilation signal of particle-antiparticle interactions.

1.2 Properties of cold dark matter haloes

1.2.1 Hierarchical growth of haloes

Galaxies and haloes form hierarchically in the ΛCDM model, where smaller dark matter haloes form first and larger haloes form and grow through smooth accretion and mergers of smaller haloes. In this hierarchical framework, first proposed by White & Rees (1978), sub-dominant baryons follow the gravitational potential of dark matter. Baryonic gas, then, can lose energy through cooling and fall into the centre of the potential well of dark matter haloes, where the stars form from the condensed cold gas clouds in the disk. Galaxies are, therefore, embedded within larger and more massive dark matter haloes.

The consequence of the hierarchical growth is that haloes host a rich substructure of smaller dark matter clumps (subhaloes), which were accreted into the main dark matter halo (Moore et al., 1998, 1999a; Klypin et al., 1999; Helmi et al., 2002; Gao et al., 2004), and survived tidal disruption. Galaxies in a cluster, or dwarf galaxies orbiting the Milky Way (MW), are hosted by these subhaloes.

1.2.2 Density profiles

Navarro et al. (1996b, 1997, NFW here after) have shown that the density profile of cold dark matter haloes follow a universal form of:

$$\rho(r) = \frac{\rho_{\rm crit}\,\delta_c}{(r/r_s)(1+r/r_s)^2} \tag{1.2}$$

where $\delta_c = \frac{200}{3}\frac{c^3}{ln(1+c)-c/(1+c)}$, and the concentration, c, relates the scale radius, r_s to the virial radius [2] of the halo, $r_s = r_{200}/c$. Additionally, the concentration is correlated with virial mass (or virial radius), with a relatively tight scatter (Neto et al., 2007; Ludlow et al., 2014). Therefore, the virial mass of a halo uniquely specifies its density profile, or equivalently the circular velocity profile, mass profile, and gravitational potential profile.

The NFW profile can also be parametrized using $V_{\rm max}$ and $r_{\rm max}$. $V_{\rm max}$ is the peak of the circular velocity of a NFW halo, which occurs at the radius $r_{\rm max}$. Given the correlation between mass and concentration, $V_{\rm max}$ is a unique proxy for M_{200}.

In the central region of a halo ($r << r_s$), density increases towards the centre as a power law with slope of -1, a behaviour known as cuspy.

1.2.3 Abundance of haloes and subhaloes

ΛCDM predicts that smaller haloes are dominant in terms of their number over more massive haloes, at all redshifts and all mass scales relevant to astrophysics[3]. More precisely, the mass function is a power law, $dN/dV/dM \propto M^{-\beta}$, with the slope of $\beta \sim -1.9$ below $M_{200} \sim 10^{13}$ at $z = 0$ (Jenkins et al., 2001). The mass function drops above this mass scale, as the larger haloes are under formation at z=0 .

Subhaloes of a given halo also follow a power law mass function with the slope of $\beta \sim -1.9$ (Helmi et al., 2002; Springel et al., 2008; Gao et al., 2004). The slope of

[2]Virial radius defines the virialized region of a halo. Different definitions have been used for virial radius. A common definition is the radius where the enclosed mean density is 200 times the critical density. We adopt this definition throughout this document. The virial quantities are defined with a 200 subscript. Virial mass is defined as the enclosed mass within the virial radius, $M_{200} = 200\rho_{\rm crit}4/3\pi r_{200}^3$

[3]This statement does not hold at small halo masses. The cut off depends on the mass of the dark matter particle. For a 100 GeV particle the cut off is at an earth mass.

the power law implies that most of the mass is in the most massive subhaloes/haloes, whereas the less massive ones are more abundant.

The properties mentioned above have all been studied using numerical simulations, which are the essential tools in cosmology. I bring a brief review of this method in the next section.

1.3 Numerical simulations

1.3.1 Basics

The formation of structure in the Universe is a highly nonlinear process. Numerical simulations, therefore, played a key role in studies of structure and galaxy formation, and were critical in the establishment of the standard model of cosmology.

Simulations start from initial conditions and numerically integrate the properties of dark matter and baryonic matter forward in time, given the gravitational and hydro-dynamical forces (i.e. pressure) involved. In the astrophysical and cosmological contexts, matter behaves like a fluid. The common approaches to solve the related equations are through discretization of either space or mass. In other words, the fluid can be realized as either spatial cells or particles. I will focus more on particle-based methods, since they are used in this dissertation.

Cosmological simulations use initial conditions motivated by the standard model of cosmology: random Gaussian perturbations in the density at the early universe, combined with the cosmological parameters, i.e. Ω's and expansion rate, set by the observations of the CMB (see, e.g., Planck Collaboration et al., 2015). The simulation volumes are typically chosen to be cubical in shape with periodic boundary conditions. If the volume is large enough ($\gtrsim 100^3$ Mpc^3), the periodic boundary condition is justified by the cosmological principle of homogeneity of the Universe on large scales.

1.3.2 Dark matter only simulations

The universal density of dark matter is 5 times larger than the baryonic matter density. The growth of structure is, therefore, driven by the gravitational force of dark matter. Cosmological simulations often ignore the effect of baryons, and treat the entire matter density as dark matter. For astrophysical purposes, cold dark matter is a pressure-less (or collision-less) fluid that interacts only gravitationally with itself and baryonic matter. As a result, the so called “dark matter only” (DMO or N-Body) simulations are computationally simpler to perform. DMO simulations were the main tools used by astrophysicists and cosmologist for studying structure formation in different cosmological models (e.g., White, 1976; White et al., 1983; Davis et al., 1985).

The growth history of dark matter haloes are easily accessible in simulations, by tracking haloes forward or backward in time and building merger trees from snapshots at different redshifts. Semi-analytic models of galaxy formation use these merger trees combined with prescriptions for physical processes involved in galaxy formation, e.g. gas accretion and star formation rates, to study properties of galaxy populations without including baryons in the simulations (Cole, 1991; Governato et al., 1998; Kauffmann et al., 1999; Benson et al., 2000). Even though semi-analytic models are useful to study global properties of galaxy populations, they can not fully capture galaxy formation physics.

1.3.3 Hydrodynamical simulations

Studying the details of galaxy formation requires including baryons and relevant hydrodynamical and galaxy formation physics in the simulations. The most important challenge, before the computational expense of such simulations, is the lack of full understanding of the physical processes involved in galaxy formation. Scannapieco et al. (2012) showed that starting from an identical initial conditions, galaxy formation codes from various major research groups yielded very different galaxies; indicating the lack of a consensus understanding of galaxy formation. Hydrodynamical simulations that can produce relatively realistic galaxy populations in terms of mass and size, have not been available until very recently (Schaye et al., 2015; Vogelsberger et al., 2014).

As mentioned earlier, baryons in astrophysical simulations are modelled by finite resolution elements, i.e. particles or cells, that impose a spatial scale below which physical processes are not resolved. Depending on the resolution of simulations, this scale varies by orders of magnitude. This scale is a few orders of magnitude larger than the region where a single star forms, even in the highest resolution galaxy formation simulations (Sawala et al., 2016a; Wetzel et al., 2016; Wheeler et al., 2015; Grand et al., 2017). As a result, a series of important processes involved in galaxy formation is implemented in hydrodynamical simulations by predefined prescriptions for resolution elements, known as subgrid physical model. The subgrid model is the most uncertain part of the hydrodyamical numerical simulations. The key components of all the successful subrid physics models, to this date, include cooling of gas, star formation, feedback from evolving stars and supernovae, cosmic UV-Xray background, feedback from super-massive black holes. Various research groups, however, have different assumptions and parameters in the implementation of these processes, (see, e.g., Schaye et al., 2015; Vogelsberger et al., 2014; Hopkins et al., 2017; Stinson et al., 2013; Zolotov et al., 2012).

The common approach for choosing the assumptions and parameters is calibrating the model to reproduce global properties of galaxies, such as mass, size and stellar-to-halo mass ratio.

1.3.4 Zoom-in simulations

Studying faint objects or the inner structure of galaxies and haloes, requires increasing the resolution of the numerical simulations in order to resolve small spatial or mass scales. Increasing the resolution of a simulation comes with increasing the computational cost of running it, such that hydrodynamical simulations of a full cosmological volume at the desired resolution for studying galaxies fainter than the MW, is not plausible with the current hardware and software.

In particle-based simulations, the technique known as "zoom-in" initial conditions allows simulating a cosmological volume while increasing the resolution *only* in a region of interest (Power et al., 2003). In this method, mass resolution is increased in a specific region of the cosmological box, while the rest of the box is sampled with coarser resolution elements (i.e. more massive particles). Moreover, the region of interest can include hydrodynamics and galaxy formation physics, while the rest of the cosmological box includes only coarser DMO particles. Since the tidal forces of the large scale is preserved in this technique, the region of interest evolves in a consistent fashion. This method has been proven to be extremely useful: most studies involving faint dwarf galaxies take advantage of this method (see, e.g., Springel et al., 2008; Sawala et al., 2010; Hopkins et al., 2017).

1.4 Near Field Cosmology

1.4.1 A review of the Local Group of galaxies

Our very own MW and its nearest massive neighbour, Andromeda (M31), along with over 100 fainter (dwarf) galaxies, form the Local Group (LG) of galaxies, within a region of radius ~ 2 Mpc. The LG is a bound system, where the MW and M31 are approaching each other in their first orbit (Li & White, 2008; Kahn & Woltjer, 1959). The LG system is relatively isolated. The neighbouring large galaxy, M82, is at the distance of 3.5 Mpc (Tully et al., 2013), and the nearest cluster is Virgo at ~ 17 Mpc (Tonry et al., 2001).

Dwarf galaxies of the LG either are satellites of the MW or M31, or live in relative isolation and are mainly falling into the LG for the first time [4]. According to the line-of-sight velocities of dwarfs, the zero-velocity surface [5] of the LG is at approximately 1.2 Mpc (McConnachie, 2012) from the barycentre of the LG.

Dwarf galaxies are defined based on their luminosity. They are less luminous than $M_V \sim -18$ mag or $M_{\rm star} \sim 10^9\,{\rm M}_\odot$, equivalent to the luminosity of the Large Magellanic Cloud (LMC), and the faintest ones discovered so far are as faint as $\sim 10^2\,{\rm M}_\odot$ (e.g. Seg I, Belokurov et al., 2007; Martin et al., 2008). The faintest dwarfs, known as ultra faint dwarfs, with stellar masses below $10^5\,{\rm M}_\odot$, have comparable luminosities to star clusters, in particular globular clusters (GCs). The dark matter content is what differentiates the two classes of objects. The mass of star clusters are entirely made up of their stars, as opposed to dwarf galaxies which contain significant amount of dark matter. Observationally, velocity dispersion measurements of the GCs indicates total mass-to-light ratios on the order of $M/L \sim 1$, whereas velocity dispersions of dwarf galaxies point to high mass-to-light ratios; at times, as high as $M/L \sim 1000$ (e.g. Simon et al., 2011). Additionally, GCs are on average more compact, composed of single stellar populations[6] (Misgeld & Hilker, 2011), with a smaller spread in their metallicity distribution (Willman & Strader, 2012; Leaman, 2012). Dwarf galaxies on the other hand are larger by almost an order of magnitude and have longer periods of star formation, at times as long as the age of the Universe (Weisz et al., 2011)

[4] There are debates about a few cases on whether they have interacted with the MW and/or M31 in the past (Teyssier et al., 2012).

[5] An approximately spherical region centred on the barycentre of the LG, where enclose objects have negative radial velocities, and further objects are expanding with the Hubble flow.

[6] Color Magnitude Diagram of a few GCs, show 2 or 3 distinct stellar populations

At the beginning of the 21st century, only ~ 40 dwarf galaxies were known in the LG (Mateo, 1998). This number has increased threefold since then, thanks to large surveys or dedicated ones such as Sloan Digital Sky Survey (SDSS), VLT-ATLAS, Pan-STARRS, Pan-Andromeda Archaelogocal Survey (PAndAS McConnachie et al., 2009), Dark Energy Survey (DES), and SMASH (Bechtol et al., 2015; Drlica-Wagner et al., 2015; Koposov et al., 2015; Kim et al., 2015; Kim & Jerjen, 2015; Martin et al., 2015; Belokurov et al., 2014; Laevens et al., 2014, 2015b,a).

Due to their faint nature, dwarf galaxies below stellar mass of $\sim 10^7\,\mathrm{M}_\odot$ have been discovered only in and around the LG. Moreover, the proximity of these objects in the LG allows detailed measurements of their properties. In particular, resolved stellar photometry and spectroscopy of these objects are only possible for LG members. The LG is, therefore, considered a a unique laboratory for testing predictions of the standard model of cosmology on small scales, and for gaining a better understanding of galaxy formation models on the scale of dwarfs.

Despite the outstanding success of ΛCDM in explaining cosmological observations and galaxy formation on large scales, there has been debate on whether this paradigm can fully explain the observations of dwarf galaxies, or the behaviour of dark matter in the central regions of galaxies. I summarize these issues, known as "small scale problems", in the following section.

1.4.2 Small scale problems of ΛCDM

1.4.2.1 The missing satellites problem

The first CDM numerical simulations of Galactic haloes soon revealed that these haloes include thousands of subhaloes (Moore et al., 1999a; Klypin et al., 1999). Even though subhaloes are potential hosts of dwarf galaxies, only 10 satellites had been identified around the MW back then. The large discrepancy in the number of subhaloes and observed dwarf satellites of the MW is known as the missing satellites problem. A more general form of this problem can be seen in the entire LG: while the LG in CDM is filled by thousands of low mass haloes, only ~ 100 dwarfs are known (McConnachie, 2012).

Bullock et al. (2000) and Benson et al. (2003) showed that this problem is resolved by the cosmic UV/X-ray background and feedback processes from supernovae and evolving stars. These processes are effective in removing gas from the shallow potential well of the low mass haloes, and preventing star formation to occur or continue. In particular, photoionization due to the cosmic UV/Xray background at high redshift (reionization at $z \sim 10$) has been shown to heat up gas and prevent galaxy formation in haloes less massive than $V_{\rm max} \sim 10\,{\rm km\ s^{-1}}$.

Reionization and supernova/stellar feedback are the essential ingredients of the current models of galaxy formation, and the missing satellites are not considered a problem anymore. Galaxy formation models, however, should be able to produce the correct luminosity function of galaxies.

1.4.2.2 The core-cusp problem

As mentioned in Sec. 1.2.2, the density profile in the inner regions of CDM haloes is "cuspy", and is increasing towards the centre as $\rho \propto r^{\alpha}$ with $\alpha = -1$. There has been a long debate whether dark matter density profile of galaxies, inferred from their observed rotation curves, show a similar behaviour (Moore, 1994; Moore et al., 1999b; Ostriker & Steinhardt, 2003; Oh et al., 2011; Adams et al., 2014; Pontzen & Governato, 2014). These observations are mainly based on deriving the gas rotational velocity as a function of radius, using spectroscopic techniques. By assuming that the rotational velocity traces the enclosed mass, subtracting the contribution of baryons from the rotation curve will yield the dark matter mass profile (or density profile). The dark matter density profiles derived in this procedure, are flat in the central regions ("cored", $\alpha = 0$) for *some* of the dwarf galaxies. The problem is known as "core-cusp" problem.

It is less trivial to measure the density profile of dispersion supported systems, e.g. dwarf spheroidals, whose rotation curves are not observable. Therefore, existence of cores in these galaxies, that include most of MW and M31 satellites, are unclear. Walker & Peñarrubia (2011) claim that Fornax and Sculptor dwarf spheroidals (two of the MW brightest satellites) have dark matter cores, while Strigari et al. (2017) argue that their velocity dispersion profiles are consistent with CDM cuspy (sub)haloes.

Numerical and analytic studies have shown that the frequent changes of gravitational potential in the central regions of haloes, caused by bursty star formation and mass ejection driven by supernovae feedback, can change the distribution of CDM in the central regions and produce cored dark matter profiles (Navarro et al., 1996a; Pontzen & Governato, 2012, 2014). These baryon induced cores are produced in ΛCDM hydrodynamical simulations, depending on the details of the subgrid model of star formation. Simulations with bursty star formations produce cores in dwarf galaxies with stellar masses above $\sim 10^{6-7}\,\mathrm{M}_\odot$ (Di Cintio et al., 2014; Madau et al., 2014; Zolotov et al., 2012; Brooks & Zolotov, 2014; Chan et al., 2015), while quieter implementations of star formation do not produce any cores in dwarf galaxies (Schaller et al., 2015b; Oman et al., 2015; Vogelsberger et al., 2014; Grand et al., 2017).

Given the difficulties in the interpretation of the observational results and the lack of an agreement in the theoretical/computational models, the existence of dark matter cores is still highly debated.

1.4.2.3 The too-big-to-fail problem

Boylan-Kolchin et al. (2011b, 2012) N-Body simulations of MW-sized haloes from the Aquarius Project (Springel et al., 2008) to show that the Aquarius MW analogs host ~ 8 massive ($V_{\mathrm{max}} > 25\,\mathrm{km\ s}^{-1}$) subhaloes that do not match any of the MW bright satellite. The lack of observable counterparts for these massive subhaloes implies that these subhaloes are devoid of stars *if* they exist around the MW. They are however "too massive to fail" forming stars according to the current models of galaxy formation. This problem is known as the "too-big-to-fail" (TBTF) problem. A similar problem about the low mass of M31 satellites was pointed out by Tollerud et al. (2014) and Collins et al. (2013).

Different solutions for TBTF have been proposed in previous work. Wang et al. (2012b) show that assuming a lower virial mass for the MW will solve the problem by decreasing the number of massive satellites (Vera-Ciro et al., 2013; Jiang & van den Bosch, 2015; di Cintio et al., 2011; Cautun et al., 2014, see, also,). The virial mass of the MW is indeed quite uncertain (Wang et al., 2015). The mass of the MW is known only in the inner ~ 50 kpc where a number of dynamical tracers, such as halo stars or globular clusters, are observable, i.e. ~ 50 kpc. The virial mass, however, requires dynamical tracers at much larger distances of 200-300 kpc. Except for 2 dwarf galaxies with uncertain tangential velocity measurements, there are no dynamical tracers at large distances.

One of the main solutions proposed for solving the TBTF problem is dark matter cores. The effect of baryons were neglected in the original simulations were the TBTF was discussed, and some studies argue that the baryon induced dark matter cores are the solution to the TBTF problem (Chan et al., 2015; Oñorbe et al., 2015; Wetzel et al., 2016; Zolotov et al., 2012). Additionally, Brooks & Zolotov (2014) argue that the baryonic disk of the host galaxy enhances tidal stripping in the presence of the shallow (cored) dark matter profiles of satellites; therefore, bringing down the central total mass of simulated satellites into agreement with observations (Zolotov et al., 2012; Arraki et al., 2014, see, also,).

On the other hand, some studies suggest that baryons can not significantly change the inner structure of dwarf galaxies, on the scales relevant to the TBTF (Parry et al., 2012; Garrison-Kimmel et al., 2013).

Garrison-Kimmel et al. (2013) argue that the isolated dwarf galaxies of the LG also have lower masses compared to the N-body LG simulations of the ELVIS project (Garrison-Kimmel et al., 2014); known as the too-big-to-fail problem in the field (see, also, Papastergis et al., 2015).

1.5 Alternatives to ΛCDM

1.5.1 Alternative dark matter models

Cold dark matter particles have two key properties. They are (i) collision-less and (ii) massive, or equivalently have low primordial thermal energies. Both of these assumptions can be modified as discussed below.

1.5.1.1 Warm dark matter

As previously mentioned in Sec. 1.1.2, warm dark matter (WDM) particles have relatively higher thermal velocities (or lower mass) compared to CDM. WDM particle candidates which are not “too warm”, i.e. masses greater than ~ 1 KeV, are consistent with the observed matter power spectrum, probed by the Lyman-α forest (Boyarsky et al., 2009). Sterile neutrinos as WDM candidates have recently gained attention due to the observations of X-ray signals of 3.55 KeV at the centre of clusters (Bulbul et al., 2014; Boyarsky et al., 2014), the Galaxy (Boyarsky et al., 2014; Jeltema & Profumo, 2015), M31 (Boyarsky et al., 2014), and dwarf galaxies (Ruchayskiy et al., 2016). This signal can be associated to the annihilation of sterile neutrinos.

Cosmological numerical simulations have shown that the WDM models produce dark matter cores in the centre of haloes. Sterile neutrinos produce parsec-scale cores, with the addition of reducing the density of dark matter on scales of kilo-parsecs, compared to CDM. WDM has been proposed as a solution to the core-cusp or too-big-to-fail problems (Lovell et al., 2017; Wang & White, 2007).

1.5.1.2 Self-interacting dark matter

Self-interacting dark matter (SIDM) candidates have been proposed as alternative to the collision-less CDM. The SIDM models behave similarly to CDM on galaxy scales and larger, but the internal structure of haloes and their galaxies changes in these models. Spergel & Steinhardt (2000) first showed that SIDM haloes have dark matter cores. Models with constant and velocity-dependant cross sections for SIDM particles have been explored more in recent years (Vogelsberger et al., 2012, 2014; Rocha et al., 2013). All these studies show that dark matter cores develop in the centre of haloes, and therefore, offer a possible solution to the core-cups problem. Additionally Creasey et al. (2017) argue that SIDM can explain the diverse shapes of the rotation curves observed amongst galaxies (Oman et al., 2015). The reduction of density in the central regions of SIDM haloes have been claimed to be able to solve the too-big-to-fail problem (Rocha et al., 2013).

1.5.2 Alternative gravitational law

The mass discrepancy reported for clusters and galaxies, and the following proposal for the existence of non-baryonic dark matter, rely on the critical assumption that gravity behaves Newtonian [7]. The MOdified Newtonian Dynamics (MOND) was proposed by Milgrom (1983) to explain the observed mass discrepancy in galaxies. According to this hypothesis, MOND increasingly deviates from the Newtonian dynamics at smaller accelerations, $a << a_0$ where $a_0 \sim 3700\,\mathrm{m\,s^{-2}}$. Sanders & McGaugh (2002) show that MOND can explain the rotation curves of many galaxies (see McGaugh et al., 2016, for a recent work). Additionally, the bright satellites of the MW and M31 have been claimed to be consistent with MOND (e.g. McGaugh & Milgrom, 2013).

Navarro et al. (2016) show that the rotation curves of galaxies with very large dark matter cores can not be easily reconciled with MOND. MOND also is facing challenges when considering the evidence of dark matter in cosmological observations. In particular, the observations of the CMB power spectrum yield the energy density of total matter and baryonic matter (Planck Collaboration et al., 2016). The difference between the two, can not be explained in MOND.

[7] The general relativity effects are negligible at the accelerations probed by the motions of galaxies in a clusters, or the motions of stars in a galaxies. The exception is for the very central regions of galaxies close to the supermassive black holes, which is not relevant to the discussion here.

1.6 Thesis Outline

In order to gain a better understanding of the ΛCDM predictions for the LG and its dwarf galaxy members, I have been involved in the APOSTLE[8] project, a suite of ΛCDM hydrodynamical simulations of LG analogs using a state-of-the-art galaxy formation model developed for the large cosmological simulation of the EAGLE project(Schaye et al., 2015; Crain et al., 2015). The LG analogs were selected from a cosmological box and re-simulated using the zoom-in technique for achieving high resolutions for studying dwarf galaxies

In chapter 2, we study the kinematics of the LG in order to put constraints on the mass of the MW and M31. These kinematics and mass constraints were used to select the LG candidates for the APOSTLE project. The selection procedure, and an overview on the outcome of the simulations related to satellite dwarf galaxies is given in this chapter. This chapter in this format has been published as an article in the Monthly Notices of the Royal Astronomical Society (MNRAS) as Fattahi et al. (2016a). All the analysis in the article, and all the graphs and tables were done by myself.

Chapter 3 presents the study of the mass of classical dwarf spheroidal satellites of the Milky Way and compare the results with the simulated satellites in the APOSTLE suite. We address the TBTF problem and how it is resolved in APOSTLE. This chapter is available on the astro-ph as Fattahi et al. (2016b).

Chapter 4 extends the analysis of chapter 3 and goes beyond by studying the mass of all dwarf galaxies in the LG: MW and M31 satellites and newly discovered ultra faint dwarfs, as well as isolated dwarfs in the LG. We explore mass loss due to tidal stripping as the main reason behind the low mass of satellite galaxies. We track satellites back in time and find the properties of their progenitors. We finally study predictions of the MOdified Newtonian Dynamics (MOND) models for dwarfs galaxies.

Chapter 5 presents a brief conclusion and future prospects.

[8]A Project of Simulating The Local Environment

Chapter 2

The APOSTLE project: Local Group kinematic mass constraints and simulation candidate selection

2.1 Abstract

We use a large sample of isolated dark matter halo pairs drawn from cosmological N-body simulations to identify candidate systems whose kinematics match that of the Local Group of Galaxies (LG). We find, in agreement with the "timing argument" and earlier work, that the separation and approach velocity of the Milky Way (MW) and Andromeda (M31) galaxies favour a total mass for the pair of $\sim 5 \times 10^{12}\,\mathrm{M}_\odot$. A mass this large, however, is difficult to reconcile with the small relative tangential velocity of the pair, as well as with the small deceleration from the Hubble flow observed for the most distant LG members. Halo pairs that match these three criteria have average masses a factor of ~ 2 times smaller than suggested by the timing argument, but with large dispersion. Guided by these results, we have selected 12 halo pairs with total mass in the range 1.6-3.6 $\times\, 10^{12}\,\mathrm{M}_\odot$ for the APOSTLE project (A Project Of Simulating The Local Environment), a suite of hydrodynamical resimulations at various numerical resolution levels (reaching up to $\sim 10^4\,\mathrm{M}_\odot$ per gas particle) that use the subgrid physics developed for the EAGLE project. These simulations reproduce, by construction, the main kinematics of the MW-M31 pair, and produce satellite populations whose overall number, luminosities, and kinematics are in good agreement with observations of the MW and M31 companions. The APOSTLE candidate systems

thus provide an excellent testbed to confront directly many of the predictions of the ΛCDM cosmology with observations of our local Universe.

2.2 Introduction

The Local Group of galaxies (LG), which denotes the association of the Milky Way (MW) and Andromeda (M31), their satellites, and galaxies in the surrounding volume out to a distance of $\sim$ 3 Mpc, provides a unique environment for studies of the formation and evolution of galaxies. Their close vicinity implies that LG galaxies are readily resolved into individual stars, enabling detailed exploration of the star formation, enrichment history, structure, dark matter content, and kinematics of systems spanning a wide range of masses and morphologies, from the two giant spirals that dominate the Local Group gravitationally, to the faintest galaxies known.

This level of detail comes at a price, however. The Local Group volume is too small to be cosmologically representative, and the properties of its galaxy members may very well have been biased by the peculiar evolution that led to its particular present-day configuration, in which the MW and M31, a pair of luminous spirals $\sim$ 800 kpc apart, are approaching each other with a radial velocity of $\sim 120\,\mathrm{km\ s^{-1}}$. This galaxy pair is surrounded by nearly one hundred galaxies brighter than $M_V \sim -8$, about half of which cluster tightly around our Galaxy and M31 (see, e.g., McConnachie, 2012, for a recent review).

The Local Group is also a relatively isolated environment whose internal dynamics are dictated largely by the MW-M31 pair. Indeed, outside the satellite systems of MW and M31, there are no galaxies brighter than $M_B = -18$ (the luminosity of the Large Magellanic Cloud, hereafter LMC for short) within 3 Mpc from the MW. The nearest galaxies comparable in brightness to the MW or M31 are just beyond 3.5 Mpc away (NGC 5128 is at 3.6 Mpc; M81 and NGC 253 are located 3.7 Mpc from the MW).

Understanding the biases that this particular environment may induce on the evolution of LG members is best accomplished through detailed numerical simulations that take these constraints directly into account. This has been recognized in a number of recent studies, which have followed small volumes tailored to resemble, in broad terms, the Local Group (see, e.g., Gottloeber et al., 2010; Garrison-Kimmel et al., 2014). This typically means selecting $\sim$ 3 Mpc-radius regions where the mass budget is dominated by a pair of virialized halos separated by the observed MW-M31 distance and whose masses are chosen to match various additional constraints (see, e.g., Forero-Romero et al., 2013).

The mass constraints may include estimates of the individual virial[1] masses of both MW and M31, typically based on the kinematics of tracers such as satellite galaxies, halo stars, or tidal debris (see, e.g., Battaglia et al., 2005; Sales et al., 2007; Smith et al., 2007; Xue et al., 2008; Watkins et al., 2010; Deason et al., 2012; Boylan-Kolchin et al., 2013; Piffl et al., 2014; Barber et al., 2014, for some recent studies). However, these estimates are usually accurate only for the mass enclosed within the region that contains each of the tracers, so that virial mass estimates are subject to non-negligible, and potentially uncertain, extrapolation.

Alternatively, the MW and M31 stellar masses may be combined with "abundance matching" techniques to derive virial masses (see, e.g., Guo et al., 2010; Behroozi et al., 2013; Kravtsov et al., 2014, and references therein). In this procedure, galaxies of given stellar mass are assigned the virial mass of dark matter halos of matching number density, computed in a given cosmological model. Shortcomings of this method include its reliance on the relative ranking of halo and galaxy mass in a particular cosmology, as well as the assumption that the MW and M31 are average tracers of the halo mass-galaxy mass relation.

A further alternative is to use the kinematics of LG members to estimate virial masses. One example is the "numerical action" method developed by Peebles et al. (2001) to reconstruct the peculiar velocities of nearby galaxies which, when applied to the LG, predicts a fairly large circular velocity for the MW (Peebles et al., 2011). A simpler, but nonetheless useful, example is provided by the "timing argument" (Kahn & Woltjer, 1959), where the MW-M31 system is approximated as a pair of isolated point masses that expand radially away after the Big Bang but decelerate under their own gravity until they turn around and start approaching. Assuming that the age of the Universe is known, that the orbit is strictly radial, and that the pair is on first approach, this argument leads to a robust and unbiased estimate of the total mass of the system (Li & White, 2008). Difficulties with this approach include the fact that the tangential velocity of the pair is neglected (see, e.g., González et al., 2014), together with uncertainties relating the total mass of the point-mass pair to the virial masses of the individual systems.

[1]We define the virial mass, M_{200}, as that enclosed by a sphere of mean density 200 times the critical density of the Universe, $\rho_{\rm crit} = 3H^2/8\pi G$. Virial quantities are defined at that radius, and are identified by a "200" subscript.

Finally, one may use the kinematics of the outer LG members to estimate the total mass of the MW-M31 pair, since the higher the mass, the more strongly LG members should have been decelerated from the Hubble flow. This procedure is appealing because of its simplicity but suffers from the uncertain effects of nearby massive structures, as well as from difficulties in accounting for the directional dependence of the deceleration and, possibly, for the gravitational torque/pull of even more distant large-scale structure (see, e.g., Peñarrubia et al., 2014; Sorce et al., 2014, for some recent work on the topic).

A review of the literature cited above shows that these methods produce a range of estimates (spanning a factor of 2 to 3) of the individual masses of the MW and M31 and/or the total mass of the Local Group (see Wang et al., 2015, for a recent compilation). This severely conditions the selection of candidate Local Group environments that may be targeted for resimulation, and is a basic source of uncertainty in the predictive ability of such simulations. Indeed, varying the mass of the MW halo by a factor of 3, for example, would likely lead to variations of the same magnitude in the predicted number of satellites of such systems (Boylan-Kolchin et al., 2011a; Wang et al., 2012b; Cautun et al., 2014), limiting the insight that may be gained from direct quantitative comparison between simulations and observations of the Local Group.

With these caveats in mind, this paper describes the selection procedure, from a simulation of a large cosmological volume, of 12 viable Local Group environment candidates for resimulation. These 12 candidate systems form the basis of the EAGLE-APOSTLE project, a suite of high-resolution cosmological hydrodynamical resimulations of the LG environment in the ΛCDM cosmogony. The goal of this paper is to motivate the particular choices made for this selection whilst critically reviewing the constraints on the total mass of the Local Group placed by the kinematics of LG members. Preliminary results from the project (which we shall hereafter refer to as APOSTLE, a shorthand for "A Project Of Simulating The Local Environment"), which uses the same code developed for the EAGLE simulations (Schaye et al., 2015; Crain et al., 2015), have already been reported in Sawala et al. (2015, 2016b) and Oman et al. (2015).

Table 2.1 The parameters of the cosmological simulations used in this paper.

Simulation	Cosmology	Ω_m	Ω_Λ	Ω_b	h	σ_8	n_s	Cube side (Mpc)	Particle number	$m_{\rm p,DM}$ ($\rm M_\odot$)
MS-I	WMAP-1	0.25	0.75	0.045	0.73	0.9	1	685	2160^3	1.2×10^9
MS-II	WMAP-1	0.25	0.75	0.045	0.73	0.9	1	137	2160^3	9.4×10^6
EAGLE (L100N1504)	Planck	0.307	0.693	0.04825	0.6777	0.8288	0.9611	100	1504^3	9.7×10^6
DOVE	WMAP-7	0.272	0.728	0.0455	0.704	0.81	0.967	100	1620^3	8.8×10^6

We begin by using the Millennium Simulations (Springel et al., 2005; Boylan-Kolchin et al., 2009) to select relatively isolated halo pairs separated by roughly the distance between the MW and M31 and derive the distribution of total masses of pairs that reproduce, respectively, the relative radial velocity of the MW-M31 pair, or its tangential velocity, or the Hubble flow deceleration of distant LG members.

Given the disparate preferred masses implied by each of these criteria when applied individually, we decided to select pairs within a narrow range of total mass that match loosely the LG kinematics rather than pairs that match strictly the kinematic criteria but that span the (very wide) allowed range of masses. This choice allows us to explore the "cosmic variance" of our results given our choice of LG mass, whilst guiding how such results might be scaled to other possible choices. We end by assessing the viability of our candidate selection by comparing their satellite systems with those of the MW and M31 galaxies.

The plan for this paper is as follows. We begin by assessing in Sec. 2.3 the constraints on the LG mass placed by the kinematics of the MW-M31 pair and other LG members. We describe next, in Sec. 2.4, the choice of APOSTLE candidates and the numerical resimulation procedure. Sec. 2.5 analyzes the properties of the satellite systems of the main galaxies of the LG resimulations and compares them with observed LG properties. We end with a brief summary of our main conclusions in Sec. 4.7.

2.3 The mass of the Local Group

2.3.1 Observational data

We use below the positions, Galactocentric distances, line-of-sight-velocities and V-band magnitudes (converted to stellar masses assuming a mass-to-light ratio of unity in solar units) of Local Group members as given in the compilation of McConnachie (2012). We also use the relative tangential velocity of the M31-MW pair derived from M31's proper motion by van der Marel et al. (2012). When needed, we assume an LSR velocity of $220\,\mathrm{km\ s^{-1}}$ at a distance of 8.5 kpc from the Galactic center and that the Sun's peculiar motion relative to the LSR is $U_\odot = 11.1$, $V_\odot = 12.24$ and $W_\odot = 7.25\ \mathrm{km\ s^{-1}}$ (Schönrich et al., 2010), to refer velocities and coordinates to a Galactocentric reference frame.

According to these data, the MW-M31 pair is 787 ± 25 kpc apart, and is approach-

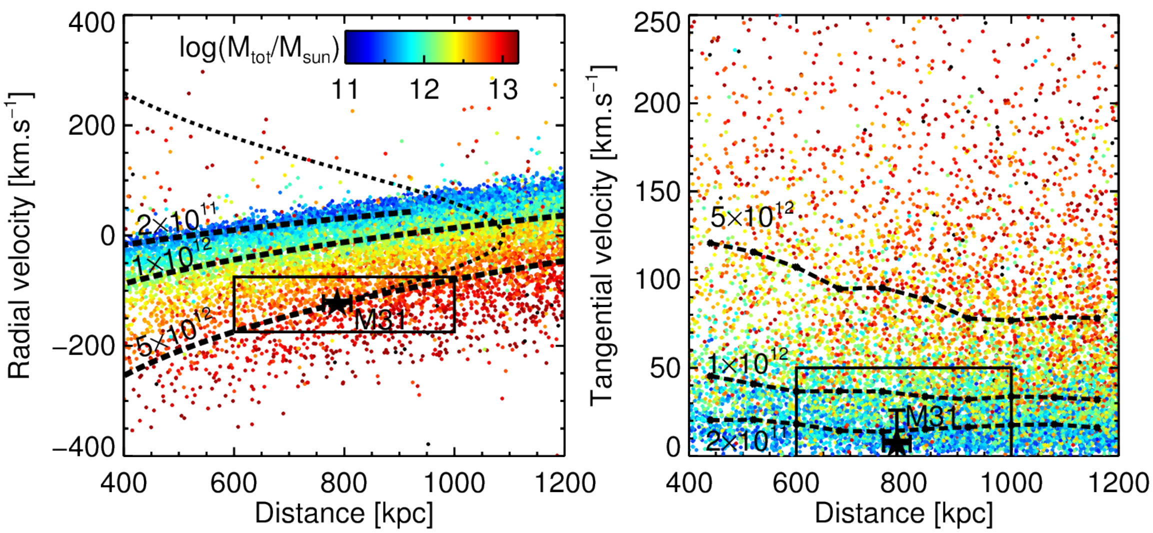

Figure 2.1 *Left*: The relative radial velocity vs distance of all halo pairs selected at highest isolation ("HiIso") from the Millennium Simulation. Colours denote the total mass of the pairs (i.e., the sum of the two virial masses), as indicated by the colour bar. The starred symbol indicates the position of the MW-M31 pair in this plane. The dotted line illustrates the evolution of a point-mass pair of total mass $\sim 5 \times 10^{12}\, M_{\odot}$ in this plane (in physical coordinates) which, according to the timing argument, ends at M31's position. Dashed lines indicate the loci, at $z = 0$, of pairs of given total mass (as labelled) but different initial energies, according to the timing argument. The box surrounding the M31 point indicates the range of distances and velocities used to select pairs for further analysis. *Right:* Same as left panel, but for the relative tangential velocity. Dashed curves in this case indicate the mean distance-velocity relation for pairs of given total mass, as labelled.

ing with a relative radial velocity of $123 \pm 4\,\mathrm{km\ s^{-1}}$. In comparison, its tangential velocity is quite low: only $7\,\mathrm{km\ s^{-1}}$ with 1σ confidence region $\leq 22\,\mathrm{km\ s^{-1}}$. We shall assume hereafter that these values are comparable to the relative velocity of the centers of mass of each member of the pairs selected from cosmological simulations. In other words, we shall ignore the possibility that the observed relative motion of the MW-M31 pair may be affected by the gravitational pull of their massive satellites; i.e., the Magellanic Clouds (in the case of the MW) and/or M33 (in the case of M31). This choice is borne out of simplicity; correcting for the possible displacement caused by these massive satellites requires detailed assumptions about their orbits and their masses, which are fairly poorly constrained (see, e.g., Gómez et al., 2015).

We shall also consider the recession velocity of distant LG members, measured in the Galactocentric frame. This is also done for simplicity, since velocities in that frame are more straightforward to compare with velocities measured in simulations. Other work (see, e.g., Garrison-Kimmel et al., 2014) has used velocities expressed in the Local Group-centric frame defined by Karachentsev & Makarov (1996). This transformation aims to take into account the apex of the Galactic motion relative to the nearby galaxies in order to minimize the dispersion in the local Hubble flow. This correction, however, is sensitive to the volume chosen to compute the apex, and difficult to replicate in simulations.

2.3.2 Halo pairs from cosmological simulations

We use the Millennium Simulations, MS-I (Springel et al., 2005) and MS-II (Boylan-Kolchin et al., 2009), to search for halo pairs with kinematic properties similar to the MW and M31. The MS-I run evolved 2160^3 dark matter particles, each of $1.2\times10^9\,\mathrm{M_\odot}$, in a box 685 Mpc on a side adopting ΛCDM cosmological parameters consistent with the WMAP-1 measurements. The MS-II run evolved a smaller volume (137 Mpc on a side) using the same cosmology and number of particles as MS-I. Each MS-II particle has a mass of $9.4\times10^6\,\mathrm{M_\odot}$. We list in Table 2.1 the main cosmological and numerical parameters of the cosmological simulations used in our analysis.

At $z = 0$, dark matter halos in both simulations were identified using a friends-of-friends (FoF, Davis et al., 1985) algorithm run with a linking length equal to 0.2 times the mean interparticle separation. Each FoF halo was then searched iteratively for self-bound substructures (subhalos) using the SUBFIND algorithm (Springel et al., 2001a). Our search for halo pairs include all pairs of separate FoF halos, as well as

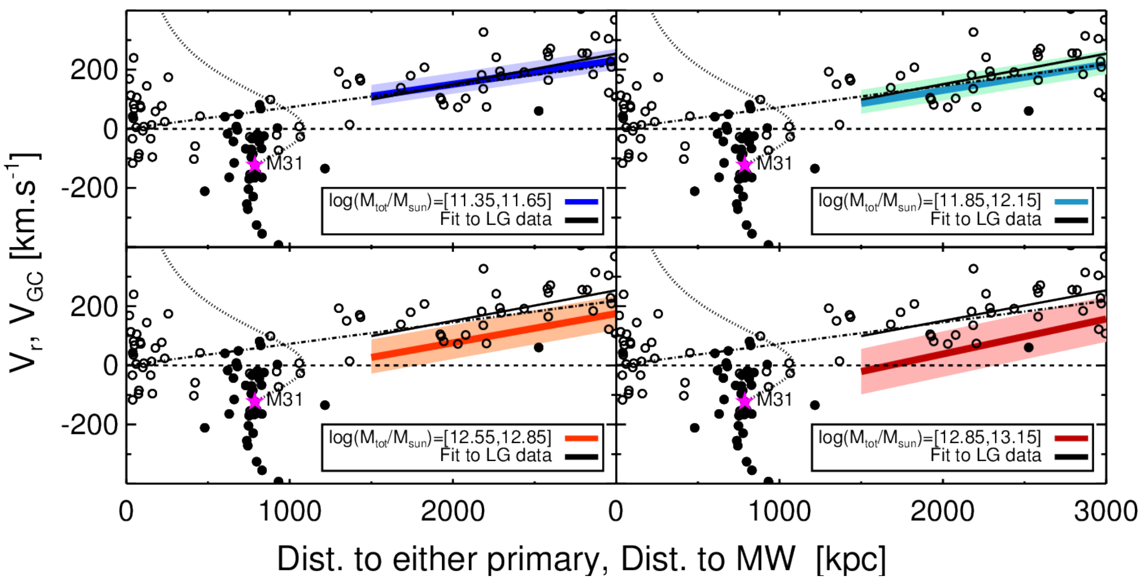

Figure 2.2 Radial velocity vs. distance for all Local Group members out to a distance of 3 Mpc from the Galactic center. Symbols repeat in each panel, and correspond to Local Group galaxies in the Galactocentric reference frame, taken from the compilations of McConnachie (2012) and Tully et al. (2009). Coloured bands are different in each panel and corrrespond to simulations. Solid symbols are used to show LG members that lie, in projection, within 30 degrees from the direction to M31. The dotted line in each panel is the timing argument curve for M31, as in Fig. 2.1. Each panel corresponds to pairs of different mass, as given in the legends. The coloured lines and shaded regions correspond, in each panel, to the result of binning MedIso MS-II halo pairs separated by 600-1000 kpc and least-square fitting the recession velocities of the outer members (between 1.5 and 3 Mpc from either primary). The solid coloured line shows the median slope and zero-point of the individual fits. The shaded regions show the interquartile range in zero-point velocity. Note that the recession speeds of outer members decrease with increasing LG mass. The dot-dashed line shows the unperturbed Hubble flow, for reference.

single FoF halos with a pair of massive subhalos satisfying the kinematic and mass conditions we list below. The latter is an important part of our search algorithm, since many LG candidates are close enough to be subsumed into a single FoF halo at $z = 0$.

The list of MS-I and MS-II halos retained for analysis include all pairs separated by 400 kpc to 1.2 Mpc whose members have virial masses exceeding $10^{11}\,\mathrm{M}_\odot$ each but whose combined mass does not exceed $10^{13}\,\mathrm{M}_\odot$. These pairs are further required to satisfy a fiducial isolation criterion, namely that no other halo more massive than the less massive member of the pair be found within 2.5 Mpc from the center of the pair (we refer to this as "medium isolation" or "MedIso", for short). We have also experimented with tighter/looser isolation criteria, enforcing the above criterion within 1 Mpc ("loosely isolated" pairs; or "LoIso") or 5 Mpc ("highly isolated" pairs; "HiIso"). Since the nearest galaxy with mass comparable to the Milky Way is located at $\sim$ 3.5 Mpc, the fiducial isolation approximates best the situation of the Local Group; the other two choices allow us to assess the sensitivity of our results to this particular choice.

2.3.3 Radial velocity constraint and the timing argument

The left panel of Fig. 2.1 shows the radial velocity vs separation of all pairs in our MS-I samples, selected using our maximum isolation criterion. Each point in this panel is coloured by the total mass of the pairs, defined as the sum of the virial masses of each member.

The clear correlation seen between radial velocity and mass, at given separation, is the main prediction of the "timing argument" discussed in Sec. 4.2. Timing argument predictions are shown by the dashed lines, which indicate the expected relation for pairs with total mass as stated in the legend. This panel shows clearly that low-mass pairs as distant as the MW-M31 pair are still, on average, expanding away from each other (positive radial velocity), in agreement with the timing argument prediction (top dashed curve). Indeed, for a total mass as low as $2 \times 10^{11}\,\mathrm{M}_\odot$, the binding energy reaches zero at $r = 914$ kpc, $V_r = 43\,\mathrm{km\ s}^{-1}$, where the dashed line ends.

It is also clear that predominantly massive pairs have approach speeds as large as the MW-M31 pair ($\sim -120\,\mathrm{km\ s}^{-1}$). We illustrate this with the dotted line, which shows the evolution in the r-V_r plane of a point-mass pair of total mass $5\times10^{12}\,\mathrm{M}_\odot$, selected to match the MW-M31 pair at the present time. The pair reached "turnaround" (i.e., null radial velocity) about 5 Gyr ago and has since been approaching from a distance of 1.1 Mpc (in physical units) to reach the point labelled "M31" by z=0, in the left-panel of Fig. 2.1.

An interesting corollary of this observation is that the present turnaround radius of the Local Group is expected to be well beyond 1.1 Mpc. Assuming, for guidance, that the turnaround radius grows roughly like $t^{8/9}$ (Bertschinger, 1985), this would imply a turnaround radius today of roughly ~ 1.7 Mpc, so that all LG members just inside that radius should be on first approach. We shall return to this point when we discuss the kinematics of outer LG members in Sec. 2.3.5 below.

2.3.4 Tangential velocity constraints

The right-hand panel of Fig. 2.1 shows a similar exercise to that described in Sec. 2.3.3, but using the relative tangential velocity of the pairs. This is compared with that of the MW-M31 pair, which is measured to be only $\sim 7\,\mathrm{km\ s^{-1}}$ by Sohn et al. (2012) and is shown by the starred symbol labelled "M31".

This panel shows that, just like the radial velocity, the tangential velocity also scales, at a given separation, with the total mass of the pair. In general, higher mass pairs have higher speeds, as gleaned from the colours of the points and by the three dashed lines, which indicate the average velocities of pairs with total mass as labelled.

The average relative tangential velocity of a $5 \times 10^{12}\,\mathrm{M_\odot}$ pair separated by ~ 800 kpc is about $\sim 100\,\mathrm{km\ s^{-1}}$, and very few of such pairs (only $\sim 6\%$) have velocities as low as that of the MW-M31 pair. The orbit of a typical pair of such mass is thus quite different from the strictly radial orbit envisioned in timing argument estimates. Indeed, the low tangential velocity of the MW-M31 pair clearly favours a much lower mass for the pair than derived from the timing argument (see González et al., 2014, for a similar finding).

The kinematics of the MW-M31 pair is thus peculiar compared with that of halo pairs selected from cosmological simulations: its radial velocity is best matched with relatively large masses, whereas its tangential velocity suggests a much lower mass. We shall return to this issue in Sec. 2.3.6, after considering next the kinematics of the outer LG members.

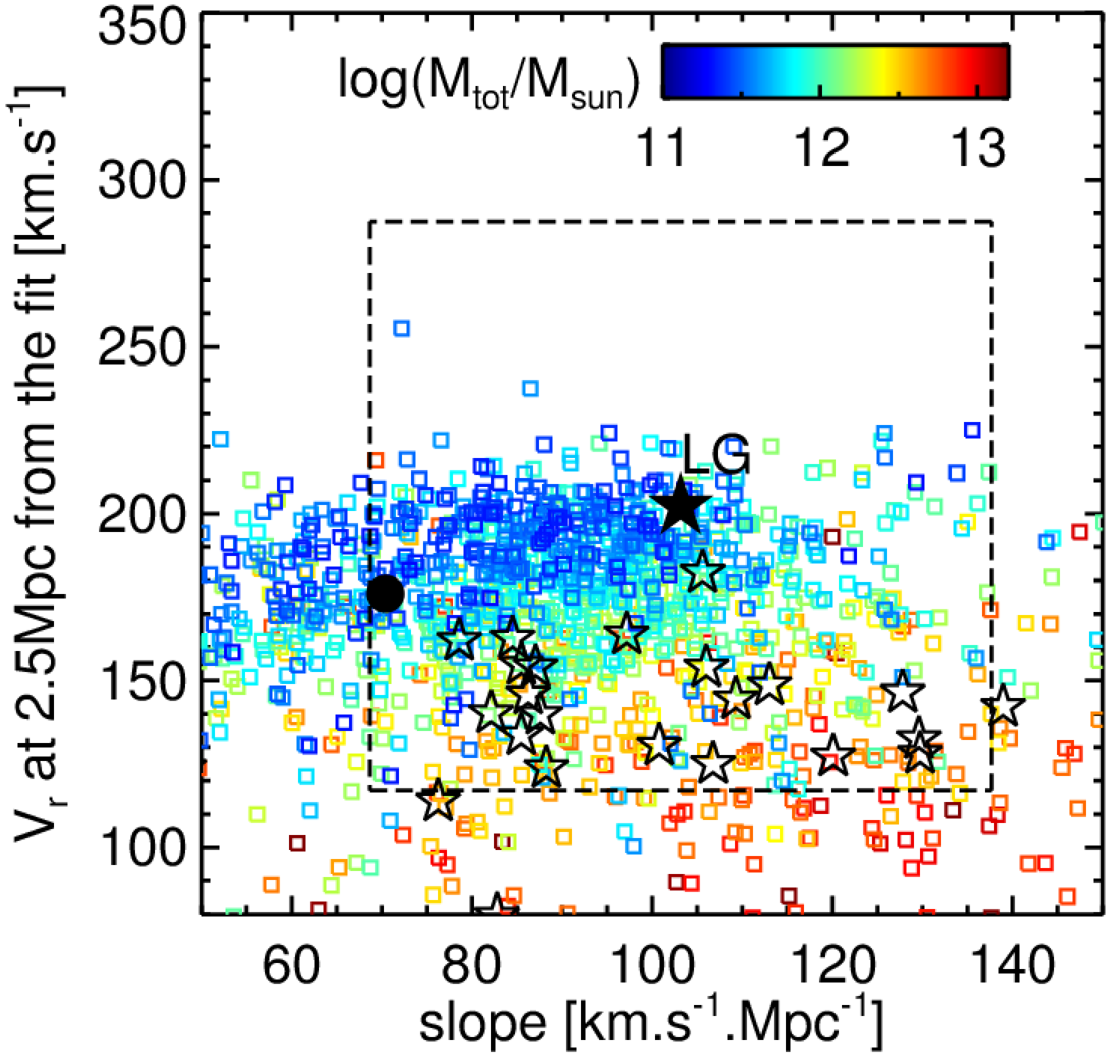

Figure 2.3 Parameters of the least-squares fits to the recession speeds of outer LG members as a function of distance. The solid starred symbol labelled "LG" indicates the result of fitting the distance vs Galactocentric radial velocity of all LG galaxies between 1.5 and 3 Mpc from the MW. The Hubble flow is shown by the solid circle. Each coloured point corresponds to a halo pair selected from the MS-II simulation assuming medium isolation, and uses all halos in the 1.5-3 Mpc range resolved in MS-II with more than 100 particles (i.e., masses greater than $1 \times 10^9\,\mathrm{M}_\odot$). Velocities and distances are measured from either primary, and coloured according to the total mass of the pair. Note that recession velocities decrease steadily as the total mass of the pair increases. The square surrounding the "LG" point indicates the error in the slope and zero-point, computed directly from the fit to the 33 LG members with distances between 1.5 and 3 Mpc. Open starred symbols correspond to the 12 pairs selected for the APOSTLE project (see Sec. 2.4.2).

2.3.5 Hubble flow deceleration

The kinematics of the more distant LG members is also sensitive to the total mass of the MW-M31 pair. In particular, we expect that the larger the mass, the more the recession velocities of those members would be decelerated from the Hubble flow. We explore this in Fig. 2.2, where the symbols in each panel show the Galactocentric radial velocity of all galaxies in the McConnachie (2012) catalogue and in the Extragalactic Distance Database of Tully et al. (2009) found within 3 Mpc of the MW. These data illustrate two interesting points. One is that all galaxies beyond ~ 1.3 Mpc from the MW are receding; and the second is that the mean velocity of all receding galaxies is only slightly below the Hubble flow, $V_r = H_0 r$, indicated by the dot-dashed line for $H_0 = 70.4$ km s^{-1} Mpc^{-1}.

The first result is intriguing, given our argument in Sec. 2.3.3 that the turnaround radius of the LG should be around ~ 1.7 Mpc at the present time. The second point is also interesting, since it suggests that the local Hubble flow around the MW (beyond ~ 1.3 Mpc) has been relatively undisturbed. The first point suggests that the M31 motion is somewhat peculiar relative to that of the rest of the LG members; the second that the total mass of the MW-M31 pair cannot be too large, for otherwise the recession velocities would have been decelerated more significantly.

We examine this in more detail in the four panels of Fig. 2.2, where the coloured lines show the mean recession speed as a function of distance for halos and subhalos surrounding candidate MS-II[2] pairs of different mass, binned as listed in the legend. Recession speeds are measured from each of the primaries for systems in the distance range 1.5-3 Mpc and are least-square fitted independently to derive a slope and velocity zero-point for each pair. The coloured lines in Fig. 2.2 are drawn using the median slope and zero-point for all pairs in each mass bin. The shaded areas indicate the interquartile range in the zero-point velocity. This figure shows clearly that the more massive the pair, the lower, on average, the recession velocities of surrounding systems.

This is also clear from Fig. 2.3, where we plot the individual values of the slopes and zero-point velocities (measured at $r = 2.5$ Mpc), compared with the values obtained from a least-squares fit to the Local Group data. The zero-point of the fit is most sensitive to the total mass of the pair; as a result, the relatively large recession

[2]We use here only MS-II pairs; the numerical resolution of the MS-I simulation is too coarse to identify enough halos and subhalos around the selected pairs to accurately measure the velocities of outer LG members.

velocity of the outer LG members clearly favours a low total mass for the MW-M31 pair.

2.3.6 Mass distributions

The histograms in Fig. 2.4 summarize the results of the previous three subsections. Each of the top three panels shows the distribution of the total masses of pairs with separations in the range $(600, 1000)$ kpc selected to satisfy the following constraints: (i) relative radial velocity in the range $(-175, -75)$ km s^{-1} (dark blue histograms; see selection box in the left panel of Fig. 2.1); (ii) tangential velocity in the range (0,50) km s^{-1} (light-blue histogram; see box in the right panel of Fig. 2.1); and (iii) Hubble velocity fits in the observed range (lightest blue histograms; see box in Fig. 2.3). The histograms in red correspond to the few systems that satisfy all three criteria at once. (The scale of the red histograms has been increased in order to make them visible; see legends.) In these three panels the isolation criteria for selecting pairs tightens from top to bottom, and, as a consequence, the total number of selected pairs decreases. As discussed before, the radial velocity constraint favours high-mass pairs, whereas the tangential velocity constraint favours low-mass ones. The Hubble velocity constraint gives results intermediate between the other two.

Fig. 2.4 shows that the main effect of relaxing the isolation criteria is to enable relatively low-mass pairs to pass the kinematic selection. The total mass of "HiIso" pairs matching the radial velocity constraint, for example, clusters tightly about the timing argument prediction ($\sim 5 \times 10^{12}\, M_{\odot}$; see dark blue histogram in the "HiIso" panel). However, a long tail of pairs with much lower masses appears in the other panels, indicating that neighbouring structures can have a non-negligible effect on the kinematics of a pair. In particular, "infall" onto a massive structure may accelerate low-mass pairs to much higher relative velocities than they would be able to reach in isolation.

The magnitude of the effect is expected to scale with the mass and distance to the most massive neighbouring system, and it seems legitimate to question whether an object like the Virgo cluster might have a discernible effect on the kinematics of the MW-M31 pair. We have checked this explicitly **by identifying the subsample of pairs in Fig. 2.4 that have a halo of mass $\gtrsim 5 \times 10^{13}\, M_{\odot}$ in the distance range[3] 15-20 Mpc. We find no statistically significant difference between**

[3]These numbers are chosen to match the Virgo cluster, a $\sim 4 \times 10^{14}\, M_{\odot}$ system situated 17 Mpc

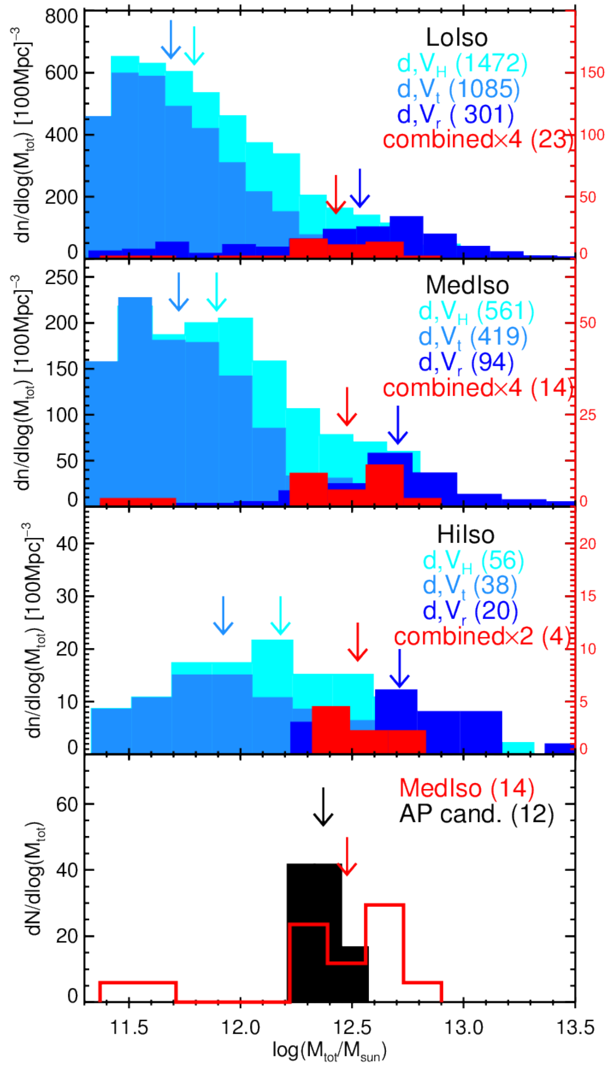

Figure 2.4 Total mass distributions of all pairs in the Millennium-II Simulation (MS-II) with separation and relative radial velocity similar to the MW-M31 pair, selected assuming different isolation criteria. The dark blue histogram shows pairs that satisfy the distance-radial velocity criterion shown by the box in the left panel of Fig. 2.1. The lighter blue histogram shows those pairs satisfying the constraint shown by the box in the distance-tangential velocity panel of Fig. 2.1. The lightest blue histogram identifies pairs satisfying the "Hubble flow" criterion shown by the box in Fig. 2.3. The red histogram corresponds to the intersection of all three criteria; their scale has been increased to make them more easily visible. The axis on the right shows the scale of the red histogram. From top to bottom, the first three panels show results for different levels of isolation, as labelled. The numbers in brackets indicate the number of pairs in each histogram. Arrows indicate the median of each distribution. The bottom panel shows in red the results for medium isolation (empty histogram), and compares them with the mass distribution of the 12 candidate pairs selected from the DOVE simulation for the APOSTLE simulation project (in solid black).

the pair mass distribution of this subsample and that of the MedIso and LoIso samples shown in Fig. 2.4. (This subsample is too small to draw a statistically sound conclusion for the HiIso case.) This suggests that only nearby massive systems can skew the pair mass distribution, and that a cluster as distant as Virgo is unlikely to play a substantial role in the kinematics of the M31-MW pair.

A further feature highlighted by Fig. 2.4 is that very few pairs satisfy all three constraints simultaneously. For the case of medium isolation (second panel from the top in Fig. 2.4) only 14 pairs satisfy the three criteria simultaneously in the (137 Mpc)^3 volume of the MS-II simulation. The bottom panel of Fig. 2.4 shows the mass distribution of pairs that satisfy all three criteria in the case of "medium isolation", the closest to our observed LG configuration (empty red histogram). The mass distribution of pairs that satisfy the three criteria simultaneously peaks at $\sim 2 \times 10^{12}\,\mathrm{M}_\odot$, a value significantly lower than the mass suggested by the timing argument. The distribution is quite broad, with an rms of 0.4 dex and a full range of values that stretches more than a decade; from $2.3 \times 10^{11}\,\mathrm{M}_\odot$ to $6.1 \times 10^{12}\,\mathrm{M}_\odot$ in the case of medium isolation.

This finding is one of the main reasons guiding our choice of mass for the halo pairs that we select for resimulation in the APOSTLE project; their distribution is shown by the solid black histogram in the bottom panel of Fig. 2.4. We describe the selection procedure of these 12 pairs in detail next.

2.4 The APOSTLE simulations

The APOSTLE project consists of a suite of high-resolution cosmological hydrodynamical simulations of 12 Local Group-like environments selected from large cosmological volumes of a ΛCDM universe. Each of these volumes has been simulated at three different resolutions with the same code as was used for the EAGLE simulation project (Schaye et al., 2015; Crain et al., 2015).

Results from a subset of these simulations have already been presented in Sawala et al. (2015, 2016b) and Oman et al. (2015). Here we describe the selection procedure for the resimulation volumes together with the physical processes included in the simulations. We assess the viability of these candidates by analyzing, in Sec. 2.5,

---

from the MW (McLaughlin, 1999; Tonry et al., 2001).

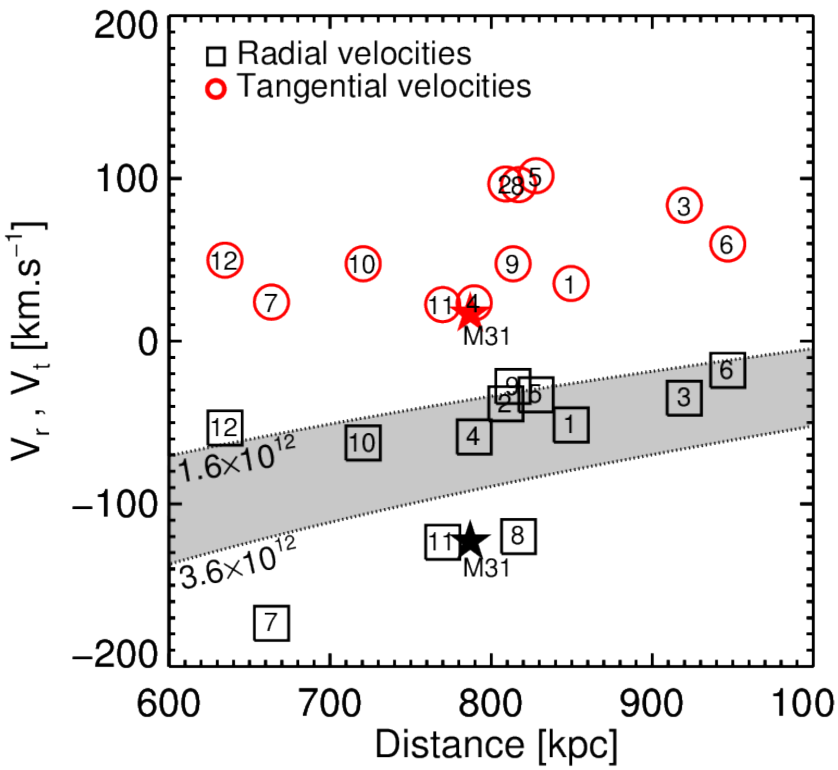

Figure 2.5 Relative radial (squares) and tangential (circles) velocities vs separation for all 12 candidates selected for resimulation in the APOSTLE project. The corresponding values for the MW-M31 pair are shown by the starred symbols. The shaded area indicate the region where we would expect the radial velocities of all 12 candidates to lie if the predictions of the timing argument held.

their satellite populations and comparing them with observations of the satellites of the MW and M31 galaxies.

2.4.1 The code

The APOSTLE simulations were run using a highly modified version of the N-body/SPH code, P-Gadget3 (Springel, 2005). The code includes sub-grid prescriptions for star formation, feedback from evolving stars and supernovae, metal enrichment, cosmic reionization, and the formation and energy output from supermassive black holes/active galactic nuclei (AGN). The details of the code and the subgrid physics model are described in detail in Schaye et al. (2015) and Crain et al. (2015) . When used to evolve a cosmologically significant volume, this code gives a galaxy stellar mass function in good agreement with observations in the range of galaxy stellar masses between $\sim 10^8$ and $\sim 10^{11}$ $M_\odot$(Schaye et al., 2015). The APOSTLE runs use the same parameter choices as the "reference" model in Schaye et al. (2015). As discussed below, we find good numerical convergence in the galaxy properties we investigate, without further calibration.

Table 2.2 TThe parameters of the APOSTLE resimulations. The first two columns list labels identifying each run. The following columns list the virial masses of each of the primaries at $z = 0$; their relative separation, radial velocity, and tangential velocity in the DOVE simulation, as well as the initial baryonic mass per particle in the hydrodynamical runs. The dark matter particle mass is $m_{\mathrm{DM}} = (1/f_{\mathrm{bar}} - 1)\, m_{\mathrm{gas}}$, where f_{bar} is the universal baryon fraction. (Dark matter-only runs have a particle mass equal to the sum of $m_{\mathrm{gas}} + m_{\mathrm{DM}}$.) The last column lists the value of the Plummer-equivalent gravitational softening, which is comoving at early times, but fixed at the listed value after $z = 3$.

Name	Run (resolution)	$M_{200}^{[1]}$ $[10^{12}(\mathrm{M}_\odot)]$	$M_{200}^{[2]}$ $[10^{12}(\mathrm{M}_\odot)]$	separation [kpc]	V_{r} [km s^{-1}]	V_{t} [km s^{-1}]	m_{gas} $[10^4(\mathrm{M}_\odot)]$	$\epsilon_{\max}$ [pc]
AP-1	L1/L2/L3	1.66	1.10	850	−51	35	0.99/12.0/147	134/307/711
AP-2	L2/L3	0.85	0.83	809	−39	97	12.5/147	307/711
AP-3	L2/L3	1.52	1.22	920	−35	84	12.5/147	307/711
AP-4	L1/L2/L3	1.38	1.35	790	−59	24	0.49/12.2/147	134/307/711
AP-5	L2/L3	0.93	0.87	828	−33	101	12.5/147	307/711
AP-6	L2/L3	2.36	1.21	950	−18	60	12.7/137	307/711
AP-7	L2/L3	1.88	1.09	664	−174	24	11.3/134	307/711
AP-8	L2/L3	1.72	0.65	817	−120	96	11.0/137	307/711
AP-9	L2/L3	0.96	0.68	814	−28	48	10.9/138	307/711
AP-10	L2/L3	1.46	0.87	721	−63	48	11.0/146	307/711
AP-11	L2/L3	0.99	0.80	770	−124	22	11.1/153	307/711
AP-12	L2/L3	1.11	0.58	635	−53	50	10.9/138	307/711

2.4.2 Candidate selection

The pairs selected for resimulation in the APOSTLE project were drawn from the DOVE[4] cosmological N-body simulation described by Jenkins (2013). DOVE evolved a periodic box 100 Mpc on a side assuming cosmological parameters consistent with the WMAP-7 estimates and summarized in Table 2.1. DOVE has 134 times better mass resolution than MS-I, with a particle mass of $8.8 \times 10^6\,\mathrm{M}_\odot$ (comparable to MS-II). Halo pairs were identified in DOVE using the procedure described in Sec. 2.3.2.

Guided by the discussion in Sec. 2.3, we chose 12 different pairs from the MedIso sample that satisfied, at $z = 0$, the following conditions:

- separation between 600 and 1000 kpc,
- relative radial velocity, V_r, in the range $(-250, 0)\,\mathrm{km\ s^{-1}}$,
- relative tangential velocity, V_t, less than $100\,\mathrm{km\ s^{-1}}$,
- recession velocities of outer LG members in the range defined by the box in Fig. 2.3
- total pair mass (i.e., the sum of the virial masses of the two primary halos) in the range $\log(M_\mathrm{tot}/\,\mathrm{M}_\odot) = [12.2, 12.6]$.

The relative velocities and separations of the 12 pairs are shown in Fig. 2.5, where each pair is labelled with a number from 1 to 12 for future reference. The main properties of these pairs are listed in Table 2.2 and the histogram of their total masses is shown (in black) in the bottom panel of Fig. 2.4. The parameters of fits to the recession velocities of the outer members are shown by the open starred symbols in Fig. 2.3.

Note that the 12 pairs chosen span a relatively small range of masses compared to what is allowed according to the kinematic constraints described in the previous section. The lowest mass of the pairs is $1.6 \times 10^{12}\,\mathrm{M}_\odot$ and the most massive pair is $3.6 \times 10^{12}\,\mathrm{M}_\odot$, with an average mass of $2.3 \times 10^{12}\,\mathrm{M}_\odot$ and an rms of only 30%. The small mass range of the pairs was chosen in order to explore the cosmic variance at fixed mass. Given the large range of allowed masses it would have been impossible to cover the whole range with high resolution resimulations.

[4]DOVE simulation is also known as COLOR.

It is interesting to compare the masses of the pairs with those estimated from the timing argument applied to each pair. This is shown by the shaded region of Fig. 2.5, which brackets the region in distance-radial velocity plane that should be occupied by the 12 candidates we selected, given their total masses. The timing argument does reasonably well in 8 out of the 12 cases, but four pairs fall outside the predicted region. Three pairs, in particular, have approach velocities as high or higher than observed for the MW-M31 pair (pairs 7, 8, and 11), demonstrating that our mass choice does not preclude relatively high approach velocities in some cases.

2.4.3 Resimulation runs

Volumes around the 12 selected pairs were carefully configured in the initial conditions of the DOVE simulation so that the inner 2-3 Mpc spherical regions centred on the mid-point of the pairs contain no "boundary" particles at $z = 0$ (for details of this "zoom-in" technique, see Power et al., 2003; Jenkins, 2013). For each candidate pair, initial conditions were constructed at three levels of resolution using second-order Lagrangian perturbation theory (Jenkins, 2010). (Further details are provided in the Appendix A.) Resolution levels are labelled L1, L2, and L3 (high, medium, and low resolution), where L3 is equivalent to DOVE, L2 is a factor of ~ 10 improvement in mass resolution over L3, and L1 is another factor of ~ 10 improvement over L2. The method used to make the zoom initial conditions has been described in Jenkins (2013). Particles masses, softening lengths, and other numerical parameters for each resolution level are summarized in Table 2.2.

Each run was performed twice, with one run neglecting the baryonic component (i.e., assigning all the matter to the dark matter component, hereafter referred to as dark-matter-only or "DMO" runs) and the other using the EAGLE code described in Sec. 2.4.1. Note that the cosmology assumed for the APOSTLE runs is the same as that of DOVE (see Table 2.1), which differs slightly from that of EAGLE. These differences, however, are very small, and are expected to have a negligible effect on our results. At the time of writing, only two volumes had been completed at the highest (L1) resolution; AP-1 and AP-4.

2.5 Local Group satellites

In this section we explore the properties of the satellite population that surrounds each of the two primary galaxies of the APOSTLE resimulations to assess whether our choice of total mass and subgrid physics gives results consistent with the broad properties of the satellite systems of the MW and M31. We examine consistency with properties that may be considered problematic, given that our choice for the total mass is significantly lower than indicated by the timing argument. In particular, we focus on (i) whether the total number of satellites brighter than $M_V = -8$ and $M_V = -9.5$ (or, equivalently, stellar mass[5], $M_{\rm gal}$, greater than 1.4×10^5 or $5.6 \times 10^5\,{\rm M}_\odot$, respectively), is comparable to the observed numbers around the MW and M31; (ii) whether satellites as massive/bright as the Large Magellanic Cloud or M33 are present; (iii) whether the velocity dispersion of the satellites is consistent with observations; and, finally, (iv) whether the observed satellites within 300 kpc of either primary (i.e., the MW or M31), are gravitationally bound given our choice of total mass for the LG candidates.

2.5.1 Satellite masses/luminosities

2.5.1.1 Number of bright satellites

The total number of satellites above a certain mass is expected to be a sensitive function of the virial masses of the primary halos (see, e.g., Boylan-Kolchin et al., 2011a; Wang et al., 2012b), so we begin by considering the number of satellites whose stellar masses exceed $1.4 \times 10^5\,{\rm M}_\odot$ or, equivalently[6], that are brighter than $M_V = -8$, as a function of the virial mass ,M_{200}, of each host. This brightness limit corresponds roughly to the faintest of the "classical" dwarf spheroidal companions of the MW, such as Draco or Ursa Minor. We choose this limit because there is widespread consensus that surveys of the surroundings of the MW and M31 are complete down to that limit (see, e.g., Whiting et al., 2007; McConnachie et al., 2009; McConnachie, 2012).

[5]Stellar masses are measured within a radius, $r_{\rm gal}$, equal to 15% of the virial radius, r_{200}, of the surrounding halo. For satellites we estimate $r_{\rm gal}$ from its peak circular velocity, $V_{\rm max}$, and the relation between $V_{\rm max}$ and r_{200} for isolated galaxies.

[6]We assume a constant mass-to-light ratio of 1 in solar units for converting stellar masses to V-band luminosities. This is done only for simplicity, since our primary aim is to assess consistency rather than to provide quantitative predictions. Later work will use spectrophotometric models and internal extinction as laid out in Trayford et al. (2015).

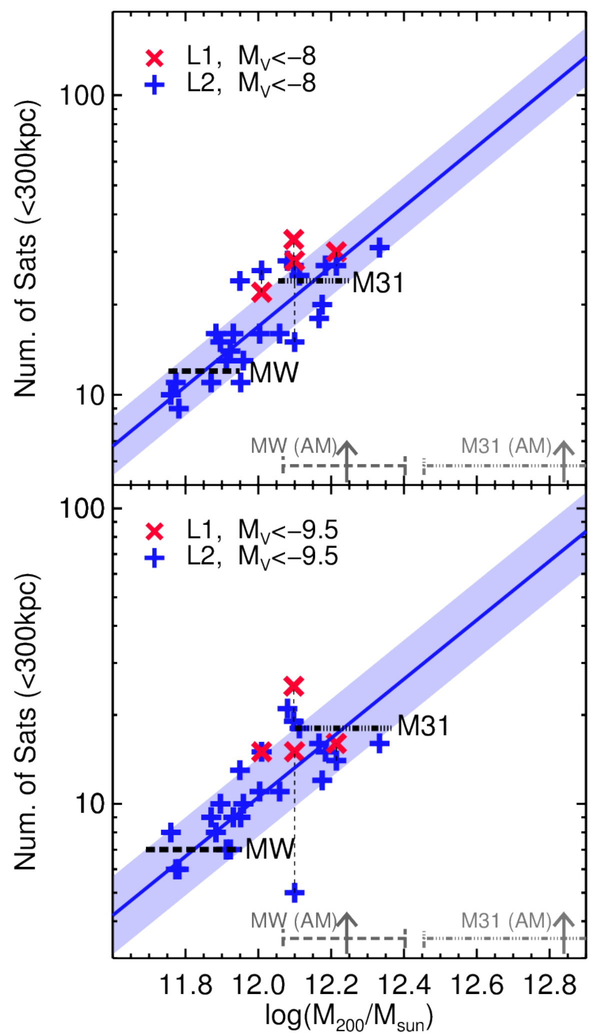

Figure 2.6 *Top*: Number of satellites with stellar mass greater than $1.4 \times 10^5\,\mathrm{M}_\odot$ (or brighter than $M_V = -8$) found within 300 kpc of each of the primary galaxies in our APOSTLE runs plotted versus the primary's virial mass. We show results for medium resolution (L2, blue plus symbols) and high resolution (L1, red crosses). The thin dashed lines connect the L1 halos to their counterparts in L2. The solid, coloured lines indicate the best fit to L2 data with unit slope; the shaded areas indicate the rms range about this fit. Small horizontal lines indicate the observed numbers for the MW and M31. Arrows indicate virial masses estimated for the MW and M31 from abundance matching of Guo et al. (2010). The "error bar" around each arrow spans different predictions by Behroozi et al. (2013) and Kravtsov et al. (2014). *Bottom*: Same as the top panel but for satellites with stellar mass greater than $5.6 \times 10^5\,\mathrm{M}_\odot$ (or brighter than $M_V = -9.5$).

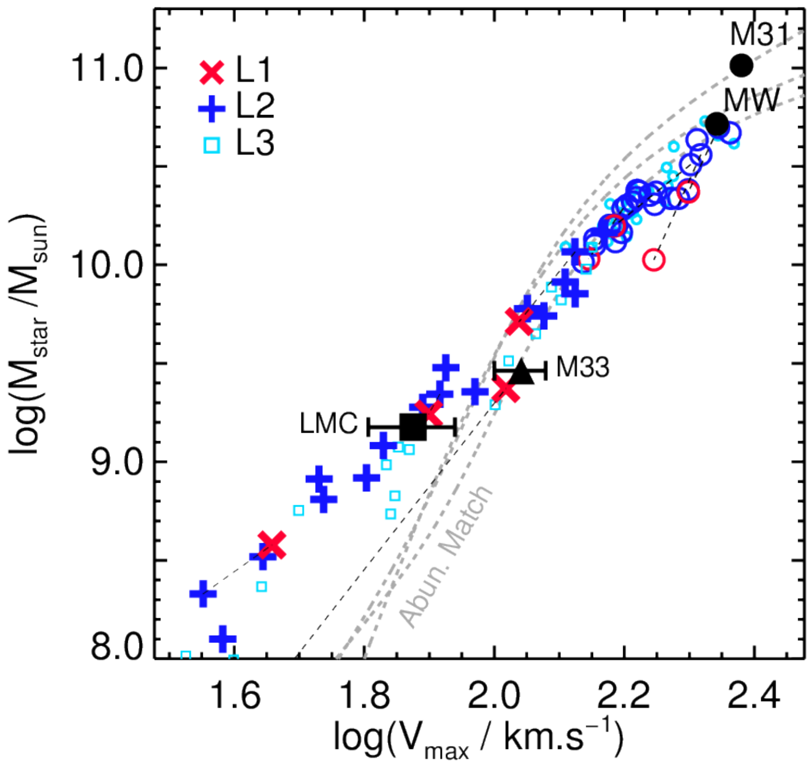

Figure 2.7 Stellar mass of the primary galaxies (circles) and their brightest satellites (crosses) for our 12 APOSTLE simulations, as a function of their maximum circular velocity. The large black solid symbols denote observational estimates for the two brightest members of the Local Group and their brightest satellites: MW, M31, LMC, and M33, respectively. Grey curves indicate "abundance matching" predictions from Guo et al. (2010); Behroozi et al. (2013); Kravtsov et al. (2014). Note that satellites as bright and massive as the LMC and M33 are not uncommon in our simulations. Note also that our primaries tend to be undermassive relative to observations and to predictions from abundance matching. The reverse applies at lower circular velocities. Black dashed lines connect matching systems at different resolution levels. See text for further discussion.

We compare in the top panel of Fig. 2.6 the number of simulated satellites within 300 kpc of each primary galaxy to the numbers observed around the MW and M31 (shown as horizontal line segments). Satellite numbers correlate strongly with virial mass, as expected, and it is encouraging that the observed number of satellites of the MW and M31 (shown by short horizontal line segments in Fig. 2.6) are well within the range spanned by our simulations. Since a lower-mass limit of $M_{\rm gal} = 1.4 \times 10^5\,\mathrm{M}_\odot$ corresponds to just a few particles at L2 resolution, we repeat the exercise in the bottom panel of Fig. 2.6, but for a higher mass limit; i.e., $M_{\rm gal} > 5.6 \times 10^5\,\mathrm{M}_\odot$ ($M_V < -9.5$). The results in either panel are reassuringly similar.

The impact of numerical resolution may be seen by comparing the results for the medium resolution (L2; blue "+" symbols) with those obtained for the L1 (high-resolution) runs in Fig. 2.6 (red crosses). On average, the number of satellites increases by only $\sim 10\%$ when increasing the mass resolution by a factor of 10, indicating rather good convergence. One of the halos in L1, however, hosts almost twice as many satellites as its counterpart in L2. The reason is that a relatively large group of satellites has just crossed inside the 300 kpc boundary of the halo in L1, but is still outside 300 kpc in L2. (We do not consider the low-resolution L3 runs in this plot because at that resolution the mass per particle is $1.5 \times 10^6\,\mathrm{M}_\odot$ and satellites fainter than $M_V \sim -13$ are not resolved, see Table 2.2.)

We also note that, had we chosen larger masses for our LG primaries, consistent with the timing argument and abundance matching, our simulations would have likely formed a much larger number of bright satellites than observed. For example, for a virial mass of $\sim 2 \times 10^{12}\,\mathrm{M}_\odot$ (the value estimated for the MW by abundance-matching analyses; see the upward arrow in Fig. 2.6) our simulations give, on average, 25 satellites brighter than $M_V = -8$ and 15 satellites brighter than $M_V = -9.5$. These are well in excess of the 12 and 8 satellites, respectively, found in the halo of the MW. The same conclusion applies to M31, where abundance matching suggests a halo mass of order $7 \times 10^{12}\,\mathrm{M}_\odot$. It is clear from Fig. 2.6 that our simulations would have produced a number of satellites well in excess of that observed around M31 for a halo as massive as that.

The correlation between host virial mass and satellite number is, of course, sensitive to our choice of galaxy formation model, and it would be possible, in principle, to reduce the number of bright satellites by reducing the overall galaxy formation efficiency in low-mass halos. It is interesting that the same galaxy formation model able to reproduce the galaxy stellar mass function in large cosmological volumes (Schaye et al., 2015) can reproduce, without further tuning, the number of satellites in the APOSTLE resimulations.

2.5.1.2 Most massive satellites

Another concern when adopting a relatively low virial mass for the LG primaries (compared to timing-argument and abundance-matching estimates), is that satellites as bright and massive as M33 in the case of M31, or the LMC in the case of the MW, may fail to form. We explore this in Fig. 2.7, where we plot the stellar mass of the primaries (open circles) and that of their most massive satellite found within 300 kpc (crosses, "plus", and square symbols for L1, L2, and L3, respectively) as a function of their peak circular velocity. We also plot, for reference, the rotation velocity and stellar masses of the MW and M31, as well as those of their brightest satellites, the LMC and M33, respectively. For the LMC, the error bar indicates the velocity range spanned by two different estimates, $64\,\mathrm{km\ s^{-1}}$ from van der Marel et al. (2002), and $87\,\mathrm{km\ s^{-1}}$ from Olsen et al. (2011). For M33, we use a rotation speed of $110\,\mathrm{km\ s^{-1}}$, with an error bar that indicates the range of velocities observed between 5 and 15 kpc by Corbelli et al. (2014): we use this range as an estimate of the uncertainty because the gaseous disk of M33 has a very strong warp in the outer regions which hinders a proper determination of its asymptotic circular speed.

Fig. 2.7 makes clear that there is no shortage of massive satellites in the APOSTLE simulations: 6 out of 24 primaries in the L2 runs have a massive subhalo with $V_{\rm max}$ exceeding $100\,\mathrm{km\ s^{-1}}$ (comparable to M33), and 12 out of 24 have $V_{\rm max} > 60\,\mathrm{km\ s^{-1}}$ (comparable to the LMC). This result is robust to numerical resolution; the numbers above change only to 7 and 11, respectively, when considering the lower-resolution L3 runs (see open squares in Fig. 2.7).

With hindsight, this result is not entirely surprising. According to Wang et al. (2012b), the *average* number of satellites scales as $10.2\,(\nu/0.15)^{-3.11}$, where $\nu = V_{\rm max}/V_{200}$ is the ratio between the maximum circular velocity of a subhalo and the virial velocity of the primary halo. A halo of virial mass $10^{12}\,\mathrm{M}_\odot$ has $V_{200} = 145\,\mathrm{km\ s^{-1}}$, so we expect, on average, that 1 in 11 of such halos should host a satellite as massive as M33 and 1 in 2.3 one like the LMC[7]. Our results seem quite consistent with this expectation.

A second point to note from Fig. 2.7 is that the stellar mass of the primary galaxies

[7]These numbers assume a maximum circular velocity of $100\,\mathrm{km\ s^{-1}}$ for M33 and $60\,\mathrm{km\ s^{-1}}$ for the LMC.

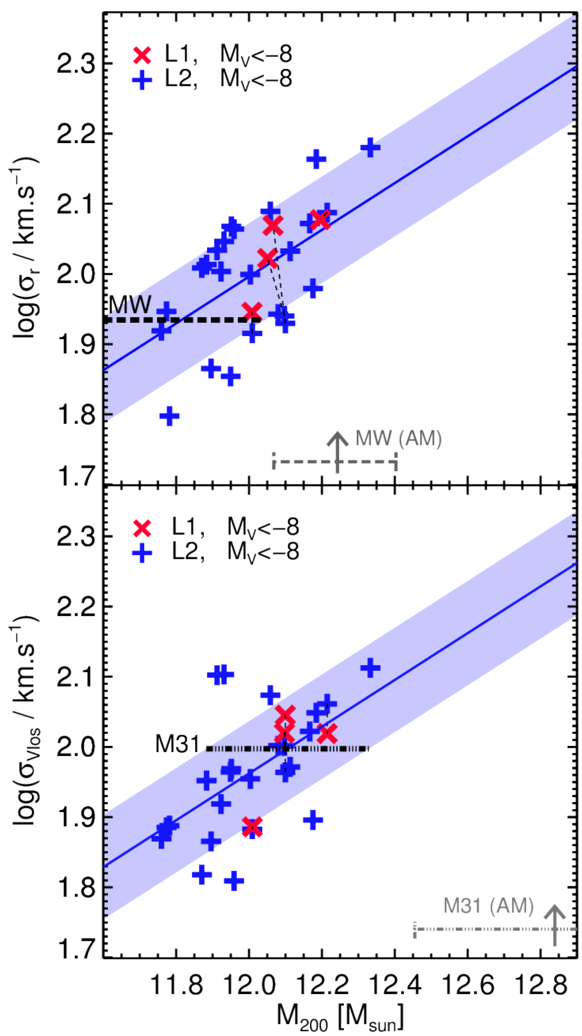

Figure 2.8 *Top*: Radial velocity dispersion of luminous satellites within 300 kpc of each primary in the APOSTLE runs, as a function of the host's virial mass. The red crosses and blue plus signs correspond to the resolution levels, L1 and L2, respectively. The thin dashed lines connect halos of different resolutions. The solid coloured line indicates the best power-law fit $\sigma \propto M^{1/3}$; the shaded areas indicate the rms around the fit. Note the strong correlation between velocity dispersion and host mass; the relatively low radial velocity dispersion of the MW satellites is best accommodated with a fairly low virial mass, lower than expected from abundance matching (see upward pointing arrow, the same as in Fig. 2.6). *Bottom:* Same as top, but for the line-of-sight velocity dispersion of one satellite system as seen from the other primary. Compared with the observed line-of-sight velocity dispersion of M31 satellites, shown by the horizontal line, this measure favours a lower virial mass than inferred from abundance-matching analyses, indicated by the arrow.

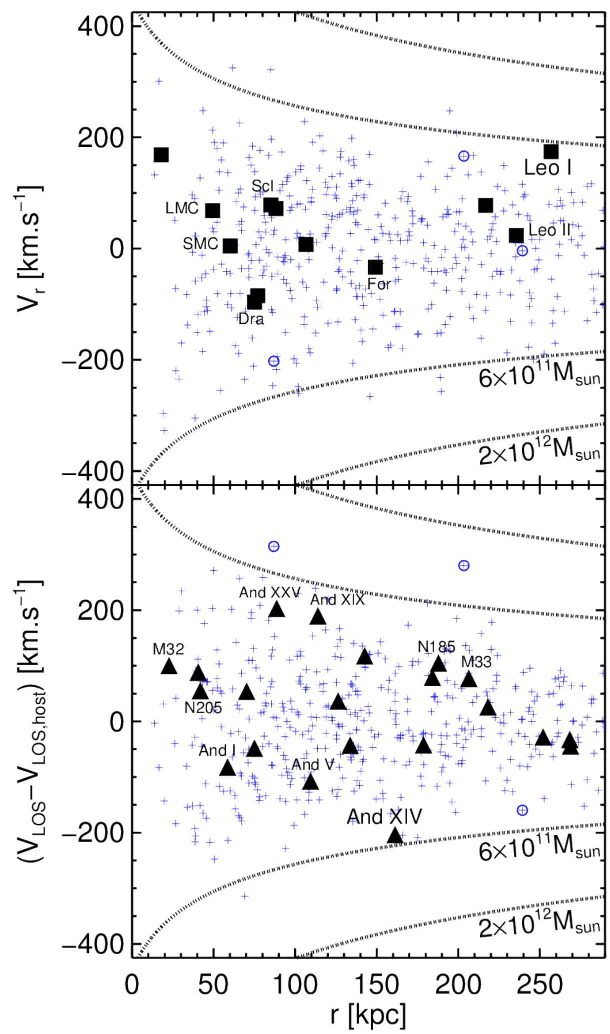

Figure 2.9 *Top*: Radial velocity vs distance for all satellites in the medium-resolution (L2) APOSTLE runs ("plus" symbols), compared with the observed radial velocities of the MW luminous satellites (filled squares). The positions of observed satellites in this phase-space correspond to regions that are well populated in the simulations. Very few satellites are "unbound" (marked by circles), as judged by escape velocity curves computed assuming a Navarro-Frenk-White profile of given virial mass (see dotted lines). *Bottom:* Same as top but for line-of-sight velocities of satellites as seen from the other primary. This may be directly compared with data for M31 satellites (filled triangles).

are below recent estimates for either the MW ($5.2 \times 10^{10}\,\mathrm{M}_{\odot}$, according to Bovy & Rix, 2013) or M31 ($1.03 \times 10^{11}\,\mathrm{M}_{\odot}$, according to Hammer et al., 2007). Indeed, none of our 24 primaries have masses exceeding $5 \times 10^{10}\,\mathrm{M}_{\odot}$, a consequence of the low virial masses of our selected LG pairs coupled with the relatively low galaxy formation efficiency of the EAGLE "Ref" model in $\sim 10^{12}\,\mathrm{M}_{\odot}$ halos. This may be seen in Fig. 2.7, where the open circles lie systematically below the grey lines, which show abundance matching predictions taken from three recent papers.

This issue has been discussed by Schaye et al. (2015), and is reflected in their fig. 4, which shows that the EAGLE "Ref" model we use here underpredicts the number of galaxies with stellar masses a few times $10^{10}\,\mathrm{M}_{\odot}$. That same figure shows that the opposite is true for smaller galaxies: the "Ref" model actually overpredicts slightly but systematically the number of galaxies with stellar masses a few times $10^{8}\,\mathrm{M}_{\odot}$.

Galaxy formation efficiency in our runs thus seems slightly too low in MW-sized halos, and slightly too high in systems of much lower mass. This slight mismatch in the galaxy mass-halo mass relation manifests itself more clearly on LG scales, making it difficult to match simultaneously the stellar masses of the MW and M31 as well as that of their luminous satellites. Indeed, increasing the halo masses of our LG candidates would lead to a better match to the stellar masses of the primaries, but at the expense of overpredicting the number of bright satellites (see, e.g., Fig. 2.6), unless the star formation and feedback parameters are recalibrated.

The stellar masses of LG galaxies are therefore a sensitive probe of the galaxy formation efficiency on cosmological scales, and provide an important constraint on the ability of cosmological codes to reproduce the observed galaxy population.

2.5.2 Satellite kinematics

We can also use the kinematics of MW and M31 satellites to gauge the consistency of our results with the simulated satellite population. We begin by considering, in the top panel of Fig. 2.8, the radial velocity dispersion, σ_r, of all satellites more massive than $1.4 \times 10^{5}\,\mathrm{M}_{\odot}$ (brighter than $M_V = -8$) within 300 kpc from either primary. We expect the satellite velocity dispersion to scale as $\sigma_r \propto V_{200} \propto M_{200}^{1/3}$, so the solid line indicates the best fit with that slope to the data for our 24 systems. (Symbols are as in Fig. 2.6; blue + symbols indicate L2 resolution, red crosses correspond to L1 resolution.) This scaling describes the correlation shown in Fig. 2.8 fairly well, and its best fit suggests that a $10^{12}\,\mathrm{M}_{\odot}$ system should host a satellite system with a radial velocity dispersion of $98 \pm 17\,\mathrm{km\ s^{-1}}$. (The shaded area in Fig. 2.8 indicates the rms scatter about the $M^{1/3}$ best fit.) The observed dispersion of the MW satellites ($86\,\mathrm{km\ s^{-1}}$; shown by the dashed horizontal line) thus suggests a mass in the range $3.9 \times 10^{11}\,\mathrm{M_\odot}$ to $1.1 \times 10^{12}\,\mathrm{M_\odot}$. The scatter, however, is large and these data alone can hardly be used to rule out larger virial masses.

The bottom panel of Fig. 2.8 shows a similar analysis, but applied to the satellites of M31. Since M31-centric radial velocities are not directly available from observations[8], we repeat the analysis for our 24 satellite systems using *projected* velocities, measured along the line of sight from the other primary of each pair. (The analysis uses only satellites within 300 kpc from the galaxy's center.) The relation between the projected velocity dispersion, σ_{Vlos}, and virial mass is again reasonably well described by the expected $M_{200}^{1/3}$ scaling. In this case, the observed projected dispersion of $99\,\mathrm{km\ s^{-1}}$ for the M31 satellites suggests a mass in the range $7.6 \times 10^{11}\,\mathrm{M_\odot}$ to $2.1 \times 10^{12}\,\mathrm{M_\odot}$ although the scatter is again large.

The main conclusion to draw from Fig. 2.8 is that the observed velocity dispersions of both the MW and M31 satellites are well within the ranges found in our simulations. The relatively low mass of our pairs thus does not seem to pose any problems reproducing the kinematics of the LG satellite population. On the contrary, as was the case for satellite numbers, the satellite kinematics would be difficult to reconcile with much larger virial masses. For example, if the MW had a virial mass of $1.8 \times 10^{12}\,\mathrm{M_\odot}$, as suggested by abundance-matching (Guo et al., 2010), then its satellite systems would, on average, have a velocity dispersion of order $120\,\mathrm{km\ s^{-1}}$, which would exceed the $86\,\mathrm{km\ s^{-1}}$ observed for the MW companions.

Finally, we check whether any of the MW or M31 satellites would be unbound given the mass of the primaries chosen for our sample. We explore this in Fig. 2.9, where we plot the observed velocity (radial in the case of the MW; line-of-sight in the case of M31) of satellites as a function of their distance to the primary's center (solid symbols).

The dotted lines delineate the escape velocity as a function of distance for halos with virial massses of 6×10^{11} and $2 \times 10^{12}\,\mathrm{M_\odot}$, corresponding to roughly the minimum and maximum virial masses of all primaries in our sample. The escape velocities assume a Navarro-Frenk-White profile (Navarro et al., 1996b, 1997), with a concentration $c = 10$. "Escapers" (i.e., satellites with $3D$ velocities exceeding the

[8]The M31-centric radial velocities can in principle be inferred from the data, but only by making further assumptions; see. e.g., Karachentsev & Kashibadze (2006)

escape speed for its primary) are shown by circled symbols. These are rare; only 3 of the 439 $M_V < -8$ satellites examined are moving with velocities exceeding the nominal NFW escape velocity of their halo (see also Boylan-Kolchin et al., 2013).

It is clear from this figure that, for our choice of masses, none of the MW or M31 satellites would be unbound given their radial velocity. Indeed, even Leo I and And XIV (the least bound satellites of the MW and M31, respectively) are both within the bound region, and, furthermore, in a region of phase space shared with many satellites in our APOSTLE sample. The kinematics of the satellite populations of MW and M31 thus seems consistent with that of our simulated satellite populations.

2.6 Summary and conclusions

We have analyzed the constraints placed on the mass of the Local Group by the kinematics of the MW-M31 pair and of other LG members. We used these constraints to guide the selection, from a large cosmological simulation, of 12 candidate environments for the EAGLE-APOSTLE project, a suite of hydrodynamical resimulations run at various numerical resolution levels (reaching $\sim 10^4\,\mathrm{M}_\odot$ per gas particle at the highest level) and aimed at studying the formation of galaxies in the local Universe.

APOSTLE uses the same code and star formation/feedback subgrid modules developed for the EAGLE project, which yield, in cosmologically-representative volumes, a galaxy stellar mass function and average galaxy sizes in good agreement with observations. This ensures that any success of our simulations in reproducing Local Group-scale observations does not come at the expense of subgrid module choices that might fail to reproduce the galaxy population at large. We also compare the simulated satellite populations of the two main galaxies in the APOSTLE resimulations with the observed satellite systems of M31 and MW to assess consistency with observation.

Our main conclusions may be summarized as follows:

- The kinematics of the MW-M31 pair and of other LG members are consistent with a wide range of virial masses for the MW and M31. Compared with halo pairs selected from the Millennium Simulations, the relatively fast approach velocity of MW and M31 favours a fairly large total mass, of order $5 \times 10^{12}\,\mathrm{M}_\odot$. On the other hand, the small tangential velocity and the small deceleration from the Hubble flow of outer LG members argue for a significantly smaller mass, of order $6 \times 10^{11}\,\mathrm{M}_\odot$. Systems that satisfy the three criteria are rare—only 14 are found in a $(137\,\mathrm{Mpc})^3$ volume—and span a wide range of masses, from 2.3×10^{11} to $6.1 \times 10^{12}\,\mathrm{M}_\odot$, with a median mass $\sim 2 \times 10^{12}\,\mathrm{M}_\odot$.

- Given the wide range of total masses allowed, the 12 candidate pairs selected for resimulation in the APOSTLE project were chosen to loosely match the LG kinematic criteria and to span a relatively narrow range of masses (from 1.6×10^{12} to $3.6\times10^{12}\,\mathrm{M}_\odot$, with a median mass of $2.3\times10^{12}\,\mathrm{M}_\odot$). This enables us to explore the cosmic variance of our results at fixed mass, and, potentially, to scale them to other mass choices, if needed.

- Large satellites such as LMC and M33 are fairly common around our simulated galaxies, although their total virial mass is well below that estimated from the timing argument.

- The overall abundance of simulated satellites brighter than $M_V = -8$ is a strong function of the virial mass assumed for the LG primary galaxies in our simulations. The relatively few (12) such satellites around the MW suggests a fairly low mass ($\sim 6 \times 10^{11}\,\mathrm{M}_\odot$); the same argument suggests a mass for M31 about twice as large ($\sim 1.2 \times 10^{12}\,\mathrm{M}_\odot$).

- The velocity dispersions of simulated satellites are consistent with those of the MW and M31. This diagnostic also suggests that virial masses much larger than those adopted for the APOSTLE project would be difficult to reconcile with the relatively low radial velocity dispersion observed for the MW satellite population, as well as with the projected velocity dispersion of the M31 satellite population.

- The primary galaxies in the simulations are less massive than current estimates for the MW and M31. The most likely reason for this is an inaccuracy in the subgrid modelling of star formation and feedback and its dependence on halo mass.

Our overall conclusion is that, despite some shortcomings, the APOSTLE simulation suite should prove a wonderful tool to study the formation of the galaxies that populate our cosmic backyard.

2.7 Appendix A: Parameters of the Initial Conditions

The initial conditions for the DOVE and APOSTLE simulations were generated from the PANPHASIA white-noise field (Jenkins, 2013) using second-order Lagrangian perturbation theory (Jenkins, 2010). The coordinates of the centers and the radii of the high resolution Lagrangian regions in the initial conditions, as well as the positions of the MW and M31 analogs at $z = 0$, for the twelve APOSTLE volumes are given in Table 2.3.

Table 2.3 The positions of main halos at $z = 0$ and parameters of the high resolution Lagrangian regions of the APOSTLE volumes in the initial conditions. The first column labels each volume. The next columns list the (X,Y,Z) coordinates of each of the primaries at $z = 0$. The final four columns give the comoving coordinate centre and radius of a sphere that contains the high resolution Lagrangian region in the initial conditions, for each of the zoom initial conditions. The phase descriptor for the APOSTLE runs is, in PANPHASIA format, [Panph1,L16,(31250,23438,39063),S12, CH1292987594,DOVE].

Name	X_1 [Mpc]	Y_1 [Mpc]	Z_1 [Mpc]	X_2 [Mpc]	Y_2 [Mpc]	Z_2 [Mpc]	X_l [Mpc]	Y_l [Mpc]	Z_l [Mpc]	R_l [Mpc]
AP-1	19.326	40.284	46.508	18.917	39.725	47.001	26.5	39.1	39.0	7.9
AP-2	28.798	65.944	17.153	28.366	65.981	16.470	28.1	60.2	18.4	14.3
AP-3	51.604	28.999	11.953	51.091	28.243	12.061	46.0	31.7	11.6	16.8
AP-4	63.668	19.537	72.411	63.158	20.137	72.467	57.1	20.6	74.9	8.4
AP-5	42.716	87.781	93.252	42.872	88.478	93.671	40.8	85.4	91.8	13.8
AP-6	35.968	9.980	43.782	36.171	9.223	43.251	32.9	13.1	45.2	9.9
AP-7	91.590	43.942	14.826	91.822	43.323	14.885	99.3	39.7	15.9	12.9
AP-8	4.619	22.762	85.535	4.604	23.508	85.203	4.9	20.4	89.9	9.9
AP-9	57.044	88.490	74.765	57.496	87.889	74.456	55.2	93.4	76.5	7.9
AP-10	61.949	24.232	98.305	61.867	24.925	98.124	62.5	24.5	93.5	11.7
AP-11	12.564	48.080	35.249	12.484	47.793	35.959	18.3	43.1	29.9	8.2
AP-12	97.553	89.587	72.093	97.351	90.100	72.407	98.5	91.9	81.9	7.9

Chapter 3

The cold dark matter content of Galactic dwarf spheroidals

3.1 Abstract

We examine the dark matter content of satellite galaxies in ΛCDM cosmological hydrodynamical simulations of the Local Group from the APOSTLE project. We find excellent agreement between simulation results and estimates for the 9 brightest Galactic dwarf spheroidals (dSphs) derived from their stellar velocity dispersions and half-light radii. Tidal stripping plays an important role by gradually removing dark matter from the outside in, affecting in particular fainter satellites and systems of larger-than-average size for their luminosity. Our models suggest that tides have significantly reduced the dark matter content of Can Ven I, Sextans, Carina, and Fornax, a prediction that may be tested by comparing them with field galaxies of matching luminosity *and* size. Uncertainties in observational estimates of the dark matter content of individual dwarfs have been underestimated in the past, at times substantially. We use our improved estimates to revisit the 'too-big-to-fail' problem highlighted in earlier N-body work. We reinforce and extend our previous conclusion that the APOSTLE simulations show no sign of this problem. The resolution does *not* require 'cores' in the dark mass profiles, but, rather, relies on revising assumptions and uncertainties in the interpretation of observational data and accounting for 'baryon effects' in the theoretical modelling.

3.2 Introduction

The steep slope of the dark matter halo mass function at the low-mass end is a defining characteristic of the ΛCDM cosmological paradigm. It is much steeper than the faint-end slope of the galaxy stellar mass function, implying that low-mass CDM haloes are significantly more abundant than faint dwarf galaxies (Moore et al., 1999a; Klypin et al., 1999). This discrepancy is usually reconciled by assuming that dwarfs form preferentially in relatively massive haloes, because cosmic reionization and the energetic feedback from stellar evolution are effective at removing baryons from the shallow gravitational potential of low-mass systems and at curtailing their star forming activity (Bullock et al., 2000; Benson et al., 2002; Somerville, 2002).

Such scenario makes clear predictions for the stellar mass – halo mass relation at the faint end. A simple – but powerful and widely used – parameterization of this prediction is obtained from abundance matching (AM) modeling, where galaxies and CDM haloes are ranked by mass and matched to each other respecting their relative ranked order (see, e.g., Frenk et al., 1988; Vale & Ostriker, 2004; Guo et al., 2011; Moster et al., 2013; Behroozi et al., 2013). Halo masses may thus be derived from stellar masses, yielding clear predictions amenable to observational testing.

Most such tests rely on using kinematic tracers such as rotation speeds or velocity dispersions to estimate the total gravitational mass enclosed within the luminous radius of a galaxy. Its dark matter content, computed after subtracting the contribution of the baryons, may then be used to estimate the total virial[1] mass of the system. Such estimates rely heavily on the similarity of the mass profiles of CDM haloes (Navarro et al., 1996b, 1997, referred to hereafter as NFW), and involve a fairly large extrapolation, since virial radii are typically much larger than galaxy radii.

These tests have revealed some tension between the predictions of AM models and observations. Boylan-Kolchin et al. (2011b), for example, estimated masses for the most luminous Galactic satellites that were lower than those of the most massive substructure haloes in N-body simulations of Milky Way-sized haloes from the Aquarius Project (Springel et al., 2008). Ferrero et al. (2012) reported a related finding when analyzing the dark matter content of faint dwarf irregular galaxies in the field: many of them implied total virial masses well below those predicted by AM models. Subsequent work has highlighted similar results both in the analysis of M31

[1]We define virial quantities as those corresponding to the radius where the spherical mean density equals 200 times the critical density for closure, $3H^2/8\pi G$. Virial quantities are identified by a “200” subscript.

satellites (Tollerud et al., 2014; Collins et al., 2014), as well as in other samples of field galaxies (Garrison-Kimmel et al., 2014; Papastergis et al., 2015).

These discrepancies may in principle be reconciled with ΛCDM in a number of ways. One possibility is to reconsider virial mass estimates based on the dark mass enclosed by the galaxy, a procedure that is highly sensitive to assumptions about the halo mass profile. A popular revision assumes that the assembly of the galaxy may lead to a reshuffling of the mass profile, pushing dark matter out of the inner regions and creating a constant-density 'core' in an otherwise cuspy NFW halo (e.g., Navarro et al., 1996a; Mashchenko et al., 2006; Governato et al., 2012).

These cores allow dwarf galaxies to inhabit massive haloes despite their relatively low inner dark matter content. This option has received some support from hydrodynamical simulations (see, e.g., Pontzen & Governato, 2014, for a review) although the results are sensitive to how star formation and feedback are implemented. Indeed, no consensus has yet been reached over the magnitude of the effect, its dependence on mass, or even whether such cores exist at all (see, e.g., Parry et al., 2012; Garrison-Kimmel et al., 2013; Di Cintio et al., 2014; Schaller et al., 2015b; Oman et al., 2015; Oñorbe et al., 2015, and references therein).

A second possibility is that Galactic satellites have been affected by tidal stripping, which would preferentially remove dark matter (e.g., Peñarrubia et al., 2008) and, therefore, act to reduce their dark mass content, much as the baryon-induced 'cores' discussed in the preceding paragraph. This proposal would not help to solve the issue raised by field dwarf irregulars (Ferrero et al., 2012) nor the low dark matter content of Galactic satellites (tides are, of course, already included in N-body halo simulations), unless baryon-induced cores help to enhance the effects of tides, as proposed by Zolotov et al. (2012) and Brooks & Zolotov (2014).

A third option is to revise the abundance matching prescription so as to allow dwarf galaxies to inhabit haloes of lower mass. This would be the case if some galaxies simply fail to form (or are too faint to feature in current surveys) in haloes below some mass: once these "dark" systems are taken into account, the AM stellar mass – halo mass relation would shift to systematically lower virial masses for given stellar mass, as pointed out by Sawala et al. (2013).

The existence of 'dark' subhaloes does not, on its own, solve the problem pointed out by Boylan-Kolchin et al. (2011b), which is usually referred to as the 'too-big-to-fail' problem (hereafter TBTF, see also Boylan-Kolchin et al., 2012). Indeed, associating dwarfs with lower halo masses would not explain why many of the most massive substructures in the Aquarius haloes seem inconsistent with the kinematic constraints of the known Galactic satellites.

One explanation might be that fewer massive subhaloes are present in the Milky Way (MW) than in Aquarius haloes. Since the number of substructures scales with the virial mass of the main halo, a lower Milky Way mass would reduce the number of massive substructures, thus alleviating the problem (Wang et al., 2012b; Vera-Ciro et al., 2013; Cautun et al., 2014). Another possibility is that dark-matter-only (DMO) simulations like Aquarius overestimate the subhalo mass function. Low mass haloes are expected to lose most of their baryons to cosmic reionization and feedback, a loss that stunts their growth and reduces their final mass. The effect is limited in terms of mass (baryons, after all, make up only 17 per cent of the total mass of a halo) but it can have disproportionate consequences on the number of massive substructures given the steepness of the subhalo mass function (Guo et al., 2015; Sawala et al., 2016a).

We explore these issues here using ΛCDM cosmological hydrodynamical simulations of the Local Group from the APOSTLE[2] project (Fattahi et al., 2016a; Sawala et al., 2016a). These simulations use the same code as the EAGLE project, whose numerical parameters have been calibrated to reproduce the galaxy stellar mass function and the distribution of galaxy sizes (Schaye et al., 2015; Crain et al., 2015). Our analysis complements that of Sawala et al. (2016a), who showed that APOSTLE reproduces the Galactic satellite luminosity/stellar mass function, as well as the total number of galaxies brighter than $10^5\,\mathrm{M}_\odot$ within the Local Group.

We extend here the TBTF discussion of that paper by reviewing the accuracy of observational constraints (Sec. 4.3), which are based primarily on measurements of line-of-sight velocity dispersions and the stellar half-mass radii ($r_{1/2}$) of 'classical' (i.e., $M_V < -8$) Galactic dwarf spheroidals (dSphs), and by focusing our analysis on the actual mass enclosed within $r_{1/2}$ rather than on extrapolated quantitites such as the maximum circular velocity of their surrounding haloes. We also highlight the effect of Galactic tides, and identify the satellites where such effects might be more easily detectable observationally.

This paper is organized as follows. We begin by reviewing in Sec. 4.3 the observational constraints on the mass of Galactic dSphs. We then describe briefly our simulations and discuss our main results in Sec. 4.5, and conclude with a summary of our main conclusions in Sec. 4.7.

[2]A Project Of Simulating The Local Environment

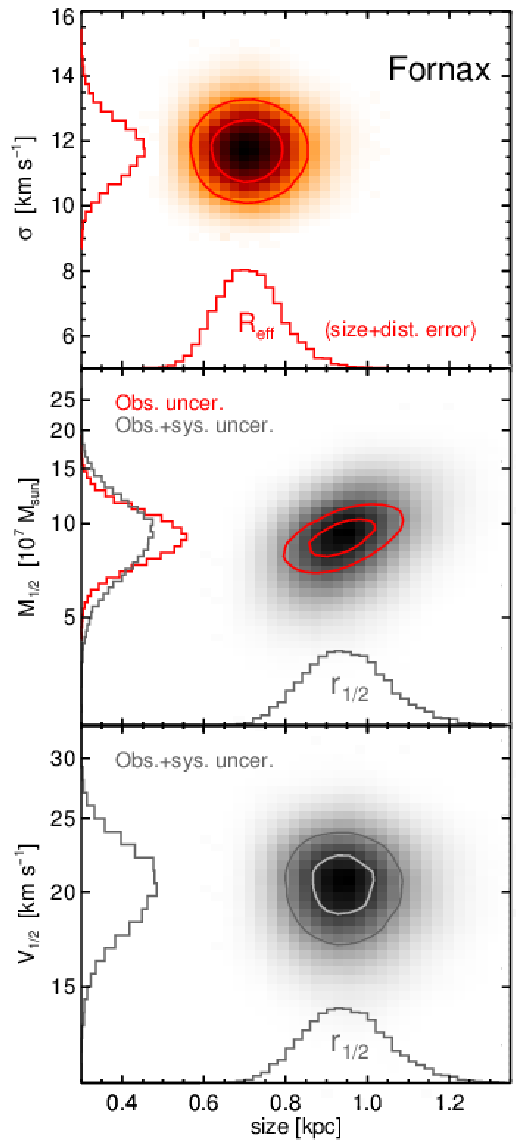

Figure 3.1 *Top*: Stellar velocity dispersion and effective radius (R_{eff}) of the Fornax dSph. The R_{eff} distribution is obtained by convolving uncertainties in distance and in the observed angular half-light radius, using uncertainties from the literature and assuming Gaussian error distributions. *Middle*: Dynamical mass within the deprojected 3D half-light radius ($r_{1/2}$) of Fornax, calculated using eq. 4.1 (Wolf et al., 2010). The red histogram shows the result of propagating the observational uncertainties, whereas the grey histogram adds a 23 per cent base modeling uncertainty, as suggested by Campbell et al. (2016). *Bottom*: Circular velocity at $r_{1/2}$ ($V_{1/2}$), including both observational and systematic uncertainties, calculated from the final $M_{1/2}$ distribution (middle panel). Unlike $M_{1/2}$, $V_{1/2}$ is independent of $r_{1/2}$. Contours in all panels enclose 50 per cent and 80 per cent of the distributions.

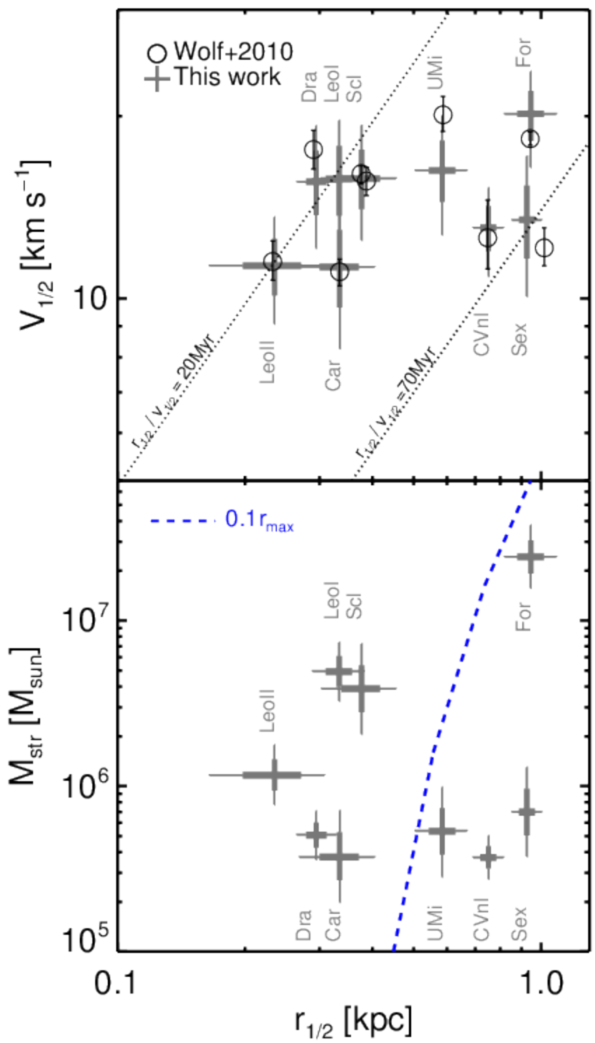

Figure 3.2 *Top:* Circular velocity at the half-light radius of Milky Way classical dSphs. Open circles show the results of Wolf et al. (2010) with 1σ error. The bar-and-whisker symbols show the results of this work, including observational and systematic uncertainties (see, e.g., the bottom panel of Fig. 3.1 for the case of the Fornax dSph). The thick and thin portions illustrate interquartile and 10–90$^{\rm th}$ percentile intervals, respectively. Our results suggest that $V_{1/2}$ uncertainties have been underestimated in previous work. Slanted lines show objects with constant crossing time, as labelled. *Bottom:* Stellar mass derived for the 9 Galactic dSphs, shown as a function of their half-light radius. The blue dashed line indicates the characteristic halo mass – radius dependence of APOSTLE centrals, computed from the fit shown in Fig. 3.3. The line divides the sample in two groups of compact objects resilient to tides and more extended systems where tidal effects may be more apparent.

3.3 The mass of Milky-Way dwarf spheroidals

Dwarf spheroidals (dSph) are dispersion-supported stellar systems, with little or no gaseous content. Their stellar velocity dispersion may be combined with the half-mass radius, $r_{1/2}$, to estimate the total mass enclosed within $r_{1/2}$. This estimate depends only weakly on the velocity anisotropy, provided that the system is in equilibrium, close to spherically symmetric, and that its velocity dispersion is relatively flat (Walker et al., 2009a; Wolf et al., 2010). In that case, the latter authors show that the total mass enclosed within the (deprojected) half-mass radius is well approximated by

$$M_{1/2} = 3\, G^{-1}\, \sigma_{\rm los}^2\, r_{1/2}, \tag{3.1}$$

where $\sigma_{\rm los}$ is the luminosity-weighted line-of-sight velocity dispersion of the stars and $r_{1/2}$ has been estimated from the (projected) effective radius, $R_{\rm eff}$, using $r_{1/2} = (4/3)R_{\rm eff}$.

The velocity dispersion profiles of the Milky Way classical dSph satellites are indeed nearly flat (Walker et al., 2007, 2009a), and eq. 4.1 has been used to estimate $M_{1/2}$ or, equivalently, the circular velocity at $r_{1/2}$, $V_{1/2} = \sqrt{GM_{1/2}/r_{1/2}}$, for many of them. The two parameters needed for eq. 4.1 are inferred from (i) individual stellar velocities; (ii) the angular projected half-light radius; and (iii) the distance modulus, each of which is subject to observational uncertainty. A lower limit on the uncertainty in $M_{1/2}$ may thus be derived by propagating the uncertainties in each of those three quantities. We shall adopt the most up-to-date values from the McConnachie (2012) Local Group compilation[3] as the main source of observational data. Table 3.1 lists our adopted values for the 9 dSphs within 300 kpc from the Milky Way. (We have excluded the Sagittarius dwarf from our analysis because it is in the process of being tidally disrupted.)

We show in Fig. 3.1 the error budget (assumed Gaussian unless otherwise specified) for the case of the Fornax dSph, one of the best studied Galactic dSphs. The top panel illustrates the errors in $\sigma_{\rm los}$ and $R_{\rm eff}$, including errors in the distance and the angular half size. The red histogram in the middle panel of Fig. 3.1 shows the result of applying eq. 4.1, after transforming $R_{\rm eff}$ into 3D $r_{1/2}$, assuming no additional error.

The error propagation results in a 20 per cent uncertainty in $M_{1/2}$, with some covariance with that in $r_{1/2}$. Note that this uncertainty is substantially larger than the $\sim$ 7 per cent uncertainty quoted for Fornax by Wolf et al. (2010). Further-

[3] http://www.astro.uvic.ca/~alan/Nearby_Dwarf_Database.html

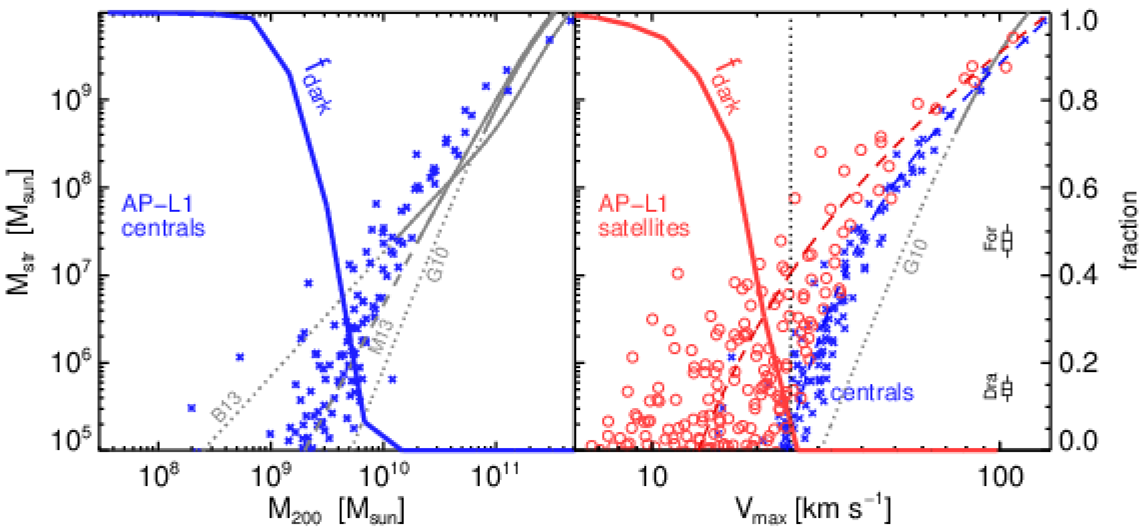

Figure 3.3 *Left*: Stellar mass – halo mass relation for 'central' galaxies in the highest resolution APOSTLE runs (L1). The abundance matching relations of Guo et al. (2010), Moster et al. (2013) and Behroozi et al. (2013) are shown for reference, labelled as G10, M13, and B13, respectively. The dotted portion of these curves indicates extrapolation of their formulae to low masses. The fraction of 'dark' systems in APOSTLE (i.e., no star particles) as a function of virial mass is indicated by the curve labelled '$f_{\rm dark}$', with the scale shown on the right axis. *Right:* Stellar mass versus maximum circular velocity ($V_{\rm max}$) of centrals and satellite galaxies (at $z = 0$ for both) in APOSTLE, shown as blue crosses and red circles, respectively. The offset between field and satellite galaxies is due to loss of mass, mostly dark matter, caused by tidal stripping. The fraction of 'dark' subhaloes is shown by the solid red curve. There are no dark subhaloes with $V_{\rm max} > 25\,{\rm km\ s^{-1}}$. Blue and red dashed lines are fits to the central and satellite stellar mass – $V_{\rm max}$ relations, respectively, of the form $M_{\rm str}/\,{\rm M_\odot} = M_0\,\nu^\alpha \exp(-\nu^\gamma)$, where ν is the velocity in units of $50\,{\rm km\ s^{-1}}$. Best fits have (M_0, α, γ) equal to $(3.0 \times 10^8, 3.36, -2.4)$ and $(8.0 \times 10^8, 2.70, -1.3)$ for centrals and satellites, respectively. For illustration, we indicate the stellar mass of Fornax and Draco with box-and-whisker symbols, at an arbitrary value of $V_{\rm max}$.

more, the uncertainty shown by the red histogram in Fig. 3.1 assumes that applying eq. 4.1 introduces no additional error. This assumption has been recently examined by Campbell et al. (2016), who conclude that such modeling has a base systematic uncertainty of ~ 23 per cent, even when half-mass radii and velocity dispersions are known with exquisite accuracy. We therefore add this in quadrature to obtain the grey histogram in the middle panel of Fig. 3.1. Finally, using the circular velocity, $V_{1/2}$, instead of $M_{1/2}$ removes the covariance between mass and radius (see bottom panel of the same figure), so we shall hereafter adopt $V_{1/2}$ for our analysis.

We have followed this procedure to compute $r_{1/2}$ and $V_{1/2}$ for all 9 classical MW dSphs, and quote their values and uncertainties in Table 3.1. Note that in a number of cases these uncertainties are well in excess of those assumed in recent work. This may also be seen in the top panel of Fig. 3.2, where the grey crosses indicate our results and compare them with the values quoted by Wolf et al. (2010), shown by the open circles. Some of the differences may be ascribed to revisions to the observational data from more recent studies and some to the increase in the error due to the base systematic uncertainty discussed above. We additionally note that the uncertainties quoted in Wolf et al. (2010) are the result of spherical Jeans analysis and maximum likelihood fits to the line-of-sight velocity dispersion profiles, rather than the propagation of errors using Eq. 4.1. The authors demonstrate that the two approaches yield similar uncertainties. Even though the uncertainties resulting from a full Jeans analysis are more accurate, the systematic uncertainty of 23 per cent we take into account is dominant over uncertainties reported in Wolf et al. (2010).

We have also estimated stellar masses for all Galactic dSphs in order to facilitate comparison with simulated data. We do this by using the V-band magnitude and distance modulus from the compilation of McConnachie (2012), and stellar mass-to-light ratios from Woo et al. (2008). Errors in V-band magnitude and distance modulus are taken from McConnachie (2012). Woo et al. (2008) do not provide uncertainties in the mass-to-light ratios, so we assume a constant 10 per cent uncertainty for all systems. We list all observable quantities and derived stellar masses in Table 3.1 and show, for future reference, the relation between stellar mass and half-mass radius in the bottom panel of Fig. 3.2.

3.4 Results

3.4.1 The Local Group APOSTLE simulations

We shall use results from the APOSTLE project, a suite of cosmological hydrodynamical simulations of 12 independent volumes chosen to resemble the Local Group of Galaxies (LG), with a relatively isolated dominant pair of luminous galaxies analogous to M31 and the Milky Way. A full description of the volume selection procedure and of the simulations is presented in Fattahi et al. (2016a) and Sawala et al. (2016a). We briefly summarize here the main parameters of the simulations relevant to our analysis.

LG candidate volumes for resimulation were selected from a dark-matter-only (DMO) simulation of a $(100\,\mathrm{Mpc})^3$ cosmological box with 1620^3 particles (known as DOVE, Jenkins, 2013). DOVE adopts cosmological parameters consistent with 7-year *Wilkinson Microwave Anisotropy Probe* (WMAP-7, Komatsu et al., 2011) measurements, as follows: $\Omega_m = 0.272$, $\Omega_\Lambda = 0.728$, $h = 0.704$, $\sigma_8 = 0.81$, $n_s = 0.967$.

Each APOSTLE volume includes a relatively-isolated pair of haloes with kinematics consistent with the MW–M31 pair; in particular: (i) the pair members are separated by 600 to 1000 kpc; (ii) they are approaching each other with velocities in the range $(-250, 0)$ km s^{-1}; and (iii) their relative tangential velocities do not exceed 100 km s^{-1}. The virial mass of the pair members are in the range $(5 \times 10^{11}, 2.5 \times 10^{12})\,\mathrm{M}_\odot$, and the combined virial masses are in the range $(1.6 \times 10^{12}, 4 \times 10^{12})\,\mathrm{M}_\odot$. An isolation criterion is also adopted to ensure that no halo more massive than the smaller of the pair is found within 2.5 Mpc from the pair barycentre.

APOSTLE volumes were resimulated using the code developed for the EAGLE simulation project (Schaye et al., 2015; Crain et al., 2015). The code is a highly modified version of the Tree-PM/SPH code, P-Gadget3 (Springel, 2005; Schaller et al., 2015a), with subgrid implementations for star formation, radiative cooling, metal enrichment, uniform UV and X-ray background (cosmic reionization), feedback from evolving stars, as well as the formation and growth of supermassive black holes and related feedback. APOSTLE runs use the parameters of the 'Ref' model described in Schaye et al. (2015). The EAGLE galaxy formation model has been calibrated to reproduce the galaxy stellar mass function and sizes in the mass range 10^8–$10^{11}\,\mathrm{M}_\odot$ at $z = 0.1$. This leads to relatively 'flat' rotation curves for luminous galaxies that agree well with observations (Schaller et al., 2015b).

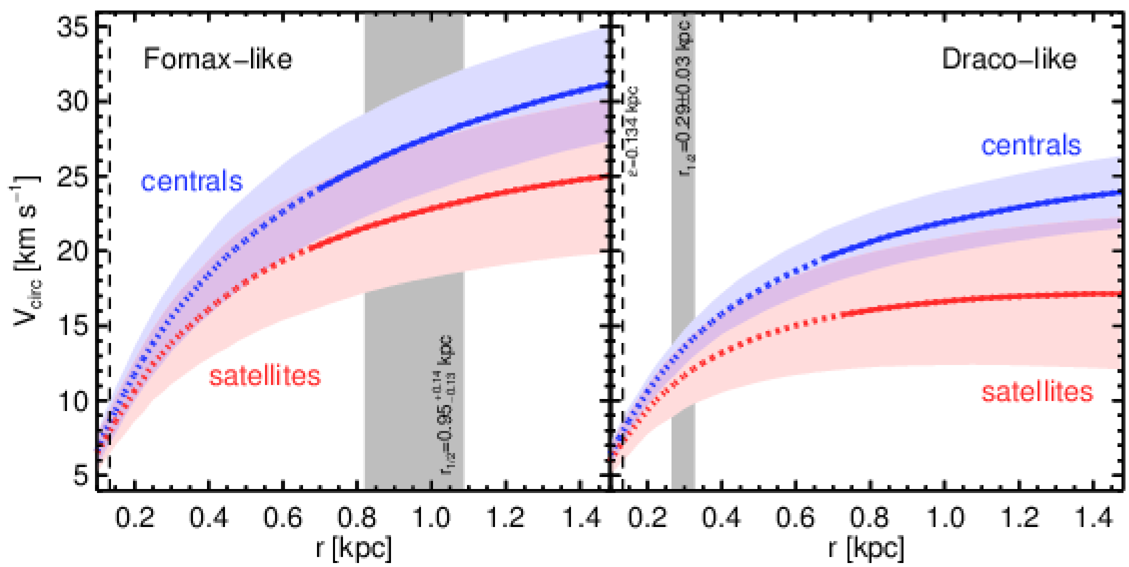

Figure 3.4 Circular velocity profiles of Fornax- and Draco-like satellites (red) and centrals (blue), as labelled. The solid lines indicate the average profiles, which turn to dotted inside the Power et al. (2003) convergence radius. Shaded regions indicate $\pm 1\sigma$ deviations. The grey vertical bars bracket the 10^{th} and 90^{th} percentiles of the half-light radii of Fornax and Draco, respectively. Note that, although both sets of satellites have been heavily stripped, the dark matter content within $r_{1/2}$ has been more significantly affected in the case of Fornax, given its relatively large size.

The APOSTLE project aims to simulate each volume at three different resolution levels (L1 to L3). At the time of writing, all 12 APOSTLE volumes (AP-1 to AP-12) have been resimulated at L3 and L2 resolution levels with gas particle mass of $\sim 10^6\,\mathrm{M}_\odot$ and $\sim 10^5\,\mathrm{M}_\odot$, respectively. Three volumes (AP-1, AP-4, AP-11, see Fattahi et al., 2016a) have also been completed at the highest resolution level, L1, with gas particle mass of $\sim 10^4$, DM particle mass of $\sim 5 \times 10^4\,\mathrm{M}_\odot$, and maximum gravitational softening of 134 pc. In this paper, we shall use mainly results from the APOSTLE L1 runs, unless otherwise specified.

Dark matter haloes in APOSTLE are identified using a friends-of-friends (FoF, Davis et al., 1985) algorithm with linking length equal to 0.2 times the mean inter-particle separation. The FOF algorithm is run on the dark matter particles; gas and star particles acquire the FoF membership of their nearest DM particle. Self-bound substructures inside each FoF halo are then found recursively using the SUBFIND algorithm (Springel et al., 2001b; Dolag et al., 2009). We will hereafter refer to the main structure of each FoF halo as its 'central', and to the self-bound substructures as its 'satellites'. MW and M31 analogues in the simulations are referred to as primary galaxies.

3.4.2 Stellar mass – halo mass relation in APOSTLE

Abundance matching models provide the relation between the stellar mass and virial mass of galaxies by assuming that every dark matter halo hosts a galaxy and that there is a monotonic correspondence between stellar mass and halo mass. The relation is best specified in the regime where the galaxy stellar mass function is well determined ($M_{\rm str} > 10^7\,\mathrm{M}_\odot$), but is routinely extrapolated to lower masses, usually assuming a power-law behaviour (Guo et al., 2010; Behroozi et al., 2013; Moster et al., 2013, hereafter G10, B13, and M13, respectively).

We compare the APOSTLE stellar mass – halo mass relation with the predictions of three different AM models in the left panel of Fig. 3.3. Stellar masses, $M_{\rm str}$, are measured for simulated galaxies within the 'galactic radius', $r_{\rm gal}$, defined as 0.15 times the virial radius the halo. This radius contains most of the stars and cold, star-forming gas of the main ('central') galaxy of each FoF halo. When considering galaxies inhabiting subhaloes ('satellites'), whose virial radii are not well defined, we shall compute $r_{\rm gal}$ using their maximum circular velocity, $V_{\rm max}$, after calibrating the

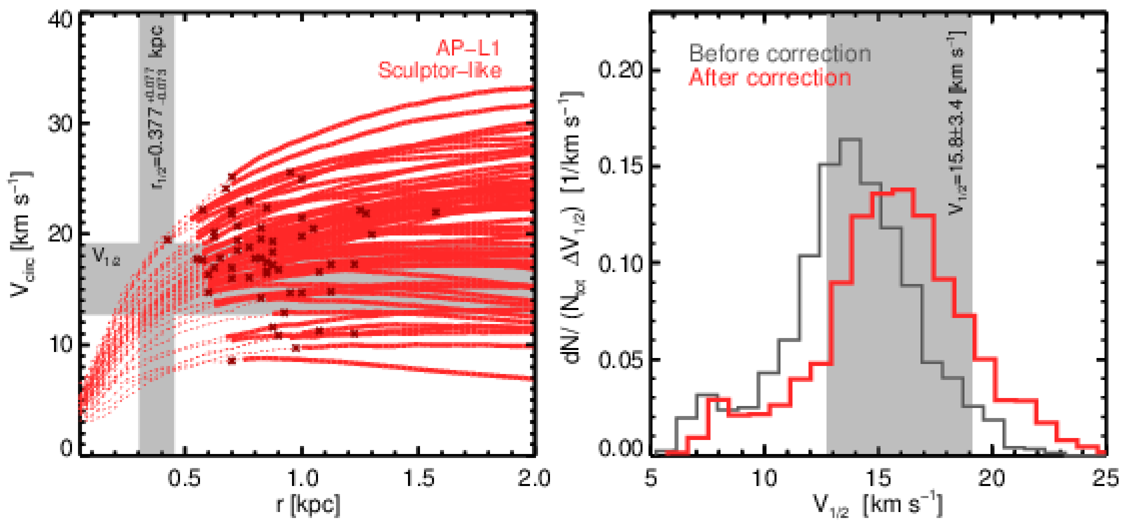

Figure 3.5 *Left*: Circular velocity curves of Sculptor-like satellites in APOSTLE, i.e., systems within 300 kpc from either of the main primaries with stellar mass matching that of Sculptor within 3σ of the central value given in Table 3.1. Curves turn from solid to dotted inside the Power et al. (2003) convergence radius (for $\kappa = 0.6$, see Appendix 3.6). The grey vertical band indicates the half-light radius of Sculptor and the corresponding 10–90$^{\rm th}$ precentile interval. Small crosses indicate the half-mass radii of Sculptor-like simulated satellites. *Right*: Distribution of circular velocities of Sculptor-like satellites, measured at the half-light radius of the Sculptor dSph (grey band on left). The red histogram shows the distribution after applying the resolution correction described in Appendix 3.6. The grey vertical band corresponds to $V_{1/2}$ of Scultpr (10–90$^{\rm th}$ precentile interval).

$V_{\rm max}$–$r_{\rm gal}$ relation[4] of the centrals.

The left panel of Fig. 3.3 shows that APOSTLE centrals do not form 'stochastically' in low mass haloes as envisioned in some models (e.g., Guo et al., 2015), but, rather, follow a tight stellar mass – halo mass relation that deviates systematically from the AM predictions/extrapolations of G10 and M13. APOSTLE galaxies of given stellar mass live in haloes systematically less massive than extrapolated by those models but more massive than the B13 extrapolation. This reflects the fact that the galaxy stellar mass function of faint galaxies is rather poorly known, and that AM 'predictions' must be considered with care in this mass regime.

The systematic offset between the G10 and M13 AM extrapolations and our numerical results has been discussed by Sawala et al. (2013, 2015), who trace the dis-

[4]Specifically, we used $r_{\rm gal}/{\rm kpc}= 0.169\,(V_{\rm max}/\,{\rm km\ s^{-1}})^{1.01}$

agreement at least in part to the increasing prevalence of 'dark'[5] haloes with decreasing virial mass. The effect of these dark systems is not subtle, as shown by the thick solid blue line in Fig. 3.3. This indicates the fraction of APOSTLE haloes that are dark (scale on right axis); only *half* of $10^{9.5}\,\mathrm{M}_\odot$ haloes harbor luminous galaxies in APOSTLE. The 'dark' fraction increases steeply with decreasing mass: 9 out of 10 haloes with $M_{200} = 10^9\,\mathrm{M}_\odot$ are dark, and fewer than 1 in 50 haloes with virial mass $\sim 10^{8.8}\,\mathrm{M}_\odot$ are luminous.

One might fear that the deviation from the AM prediction shown in Fig. 3.3 might lead to a surplus of faint galaxies in the Local Group. This is not the case; as discussed by Sawala et al. (2016a), APOSTLE volumes contain ~ 100 galaxies with $M_{\rm str} > 10^5\,\mathrm{M}_\odot$ within 2 Mpc from the LG barycentre, only slightly above the ~ 60 known such galaxies in the compilation of McConnachie (2012), which might still be incomplete due to the difficulty of finding dwarf galaxies in the Galactic 'zone of avoidance'. We shall hereafter adopt $10^5\,\mathrm{M}_\odot$ (which corresponds roughly to a magnitude limit of $M_V \sim -8$) as the minimum galaxy stellar mass we shall consider in our discussion. In APOSTLE L1 runs these systems inhabit haloes of $M_{200} \sim 2 \times 10^9\,\mathrm{M}_\odot$ (three quarters of which are 'dark'), and are resolved with a few tens of thousands of particles.

3.4.3 Tidal stripping effects

The right-hand panel of Fig. 3.3 is analogous to the left but using $V_{\rm max}$ (at $z = 0$) as a measure of mass (see also Sales et al., 2016). This allows the satellites in APOSTLE (open circles) to be included and compared with centrals (blue crosses). Satellites clearly deviate from centrals and push the offset from the G10 abundance matching prediction even further. This is mainly the result of tidal stripping, which affects disproportionately the dark matter content of a galaxy, reducing its $V_{\rm max}$ and increasing its scatter at a given stellar mass (see, e.g., Peñarrubia et al., 2008, and references therein).

Despite the large scatter, a few results seem robust. One is that *every* subhalo with $V_{\rm max} > 25\,\mathrm{km\ s^{-1}}$ is host to a satellite more massive than $10^5\,\mathrm{M}_\odot$. This implies that the number of massive subhaloes provides a firm lower limit to the total number of satellites at least as bright as the 'classical' dSphs, an issue to which we shall return

[5]These are systems with no stars in APOSTLE L1, or, more precisely, $M_{\rm str} < 10^4\,\mathrm{M}_\odot$, the mass of a single baryonic particle.

below.

A second point to note is that the effects of tidal stripping increase with decreasing stellar mass. Indeed, the $V_{\rm max}$ of Fornax-like[6] centrals is, on average, only 37 per cent higher than that of corresponding satellites; the difference, on the other hand, increases to 67 per cent in the case of Draco. This trend arises because dynamical friction erodes the orbits of massive satellites much faster than those of less luminous systems, leading to rapid merging or full disruption. As a result, surviving luminous satellites have, on average, been accreted more recently and have been less stripped than fainter systems (see, e.g., Barber et al., 2014).

This does not necessarily imply that the *stellar* components of fainter satellites have been more affected by stripping. Tides are more effective at removing (mostly dark) mass from the outskirts of a subhalo than from the inner regions, so their effects on the stellar component (for a given orbit) will be sensitive to the size of the satellite. This may be appreciated from Fig. 3.4, where we show the average circular velocity profiles of both Fornax- and Draco-like satellites and centrals. The outer regions are clearly more heavily stripped, implying that satellites that are physically large for their luminosity should show clearer signs of stripping than their more compact counterparts.

In other words, dSphs like Can Ven I or Sextans, for example, are much more likely to have been affected by tides than Draco or Leo II. Fig. 3.2 illustrates this in two different ways. In the top panel, the latter are seen to have much shorter crossing times than the former, making them more resilient to tides. Similarly, in the bottom panel, the former are shown to be physically larger than the latter both at fixed stellar mass and in terms of the characteristic radius of their host haloes (according to the stellar mass – halo mass relation for APOSTLE centrals shown in Fig. 3.3; see blue dashed line).

Thus, although our results suggest that satellites and field galaxies of similar $M_{\rm str}$ are expected to inhabit haloes of different $V_{\rm max}$, the difference might not translate directly into an observable deficit in their dark matter content[7]. This is because $V_{\rm max}$ is usually reached at radii much larger than the stellar half-mass radii where kinematic

[6]We match Galactic satellites with APOSTLE dwarfs by stellar mass. For example, we refer to systems as Fornax-like if their $M_{\rm str}$ match Fornax's within 3σ. Fornax-like *satellites* are those within 300 kpc of any of the APOSTLE primaries; Fornax-like *centrals* refer to field galaxies beyond that radius.

[7]Indeed, Kirby et al. (2014) argue that no large differences seem to exist between field and satellite galaxies in the LG.

data provide meaningful constraints. Given the large scatter in $V_{\max}$ at a given stellar mass shown by APOSTLE satellites, it is important to compare simulations and observations *at the same radii*. We explore this next.

3.4.4 The dark matter content of APOSTLE satellites

Our main conclusion from Fig. 3.3 is that APOSTLE satellites of given stellar mass are significantly less massive than expected from abundance matching and, because of stripping, span a relatively wide range of maximum circular velocities. Are these results consistent with the observational constraints discussed in Sec. 4.3? In other words, are the predicted values of $r_{1/2}$ and $V_{1/2}$ consistent with those of Galactic satellites of matching stellar mass?

The main issue to consider when addressing this question is that the half-light radii, $r_{1/2}$, of the faintest dSphs are smaller than the smallest well-resolved radius in APOSTLE. This impacts the analysis in two ways: one is that the faintest simulated dwarfs have radii larger than observed[8]; another is that the total mass enclosed by simulated dwarfs within radii as small as the observed half-light radii might be systematically affected by the limited resolution.

We illustrate this in the left panel of Fig. 3.5 for the case of the Sculptor dSph. The vertical shaded band shows the half-light radius of that galaxy, $r_{1/2} = 377^{+77}_{-73}$ pc (10–90$^{\rm th}$ percentile interval), whereas the small crosses indicate the stellar half-mass radii of Sculptor-like APOSTLE satellites on their circular velocity profiles, $V_{\rm circ}(r)$. Clearly, for the comparison with Sculptor to be meaningful, we should estimate masses within the *observed* radius (grey band), rather than at the half-mass radius of each of the simulated systems.

However, the observed $r_{1/2}$ (although significantly larger than the gravitational softening, which is fixed at 134 pc at z=0 in AP-L1 runs) is smaller the minimum resolved radius according to the convergence criterion proposed by Power et al. (2003). This is shown by the circular velocity profiles in Fig. 3.5, where the line types change from solid to dotted at the convergence radius, $r_{\rm conv}$ (defined by setting $\kappa = 0.6$ in eq. 3.3). The total mass within $r_{1/2}$ and, consequently, $V_{1/2}$, are therefore probably underestimated in the simulations. Fortunately, the analysis of Power et al. (2003) also shows that mass profiles inside $r_{\rm conv}$ deviate from convergence in a predictable

[8]The subgrid equation of state imposed on star-forming gas particles by the EAGLE model results in a minimum effective radius of $\sim$ 400 pc for galaxies in AP-L1 runs (see, e.g., Crain et al., 2015; Campbell et al., 2016).

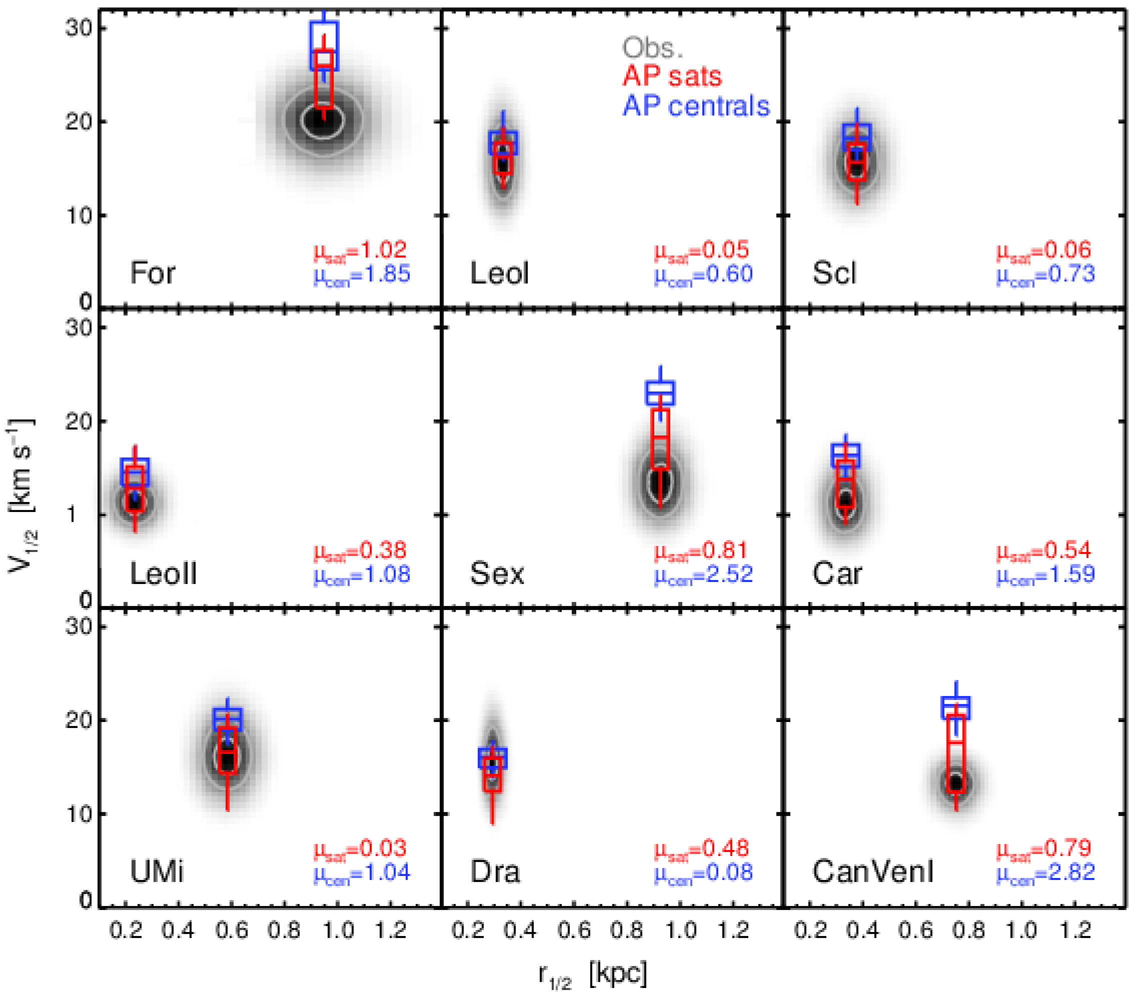

Figure 3.6 Circular velocity, $V_{1/2}$, of APOSTLE satellites matching the stellar mass of each of the 9 Galactic dSphs, and measured at the observed half-light radius of each system. Observational estimates and uncertainties are given by the grey cloud, whereas red bar-and-whisker symbols indicate the values for matching APOSTLE satellites. Contours indicate the regions containing 50 per cent and 80 per cent of the distributions. Bars and whiskers represent the interquartile and 10–90$^{\text{th}}$ percentile intervals of predicted $V_{1/2}$, plotted at the median value of $r_{1/2}$. Note the significant overlap between the satellite simulation results and the observational estimates; this may be quantified by the velocity difference between the mean observed and simulated values, divided by the combined rms of each distribution (μ), which is less than unity in all cases. The values of $V_{1/2}$ for APOSTLE centrals are larger, since centrals have not experienced tidal stripping.

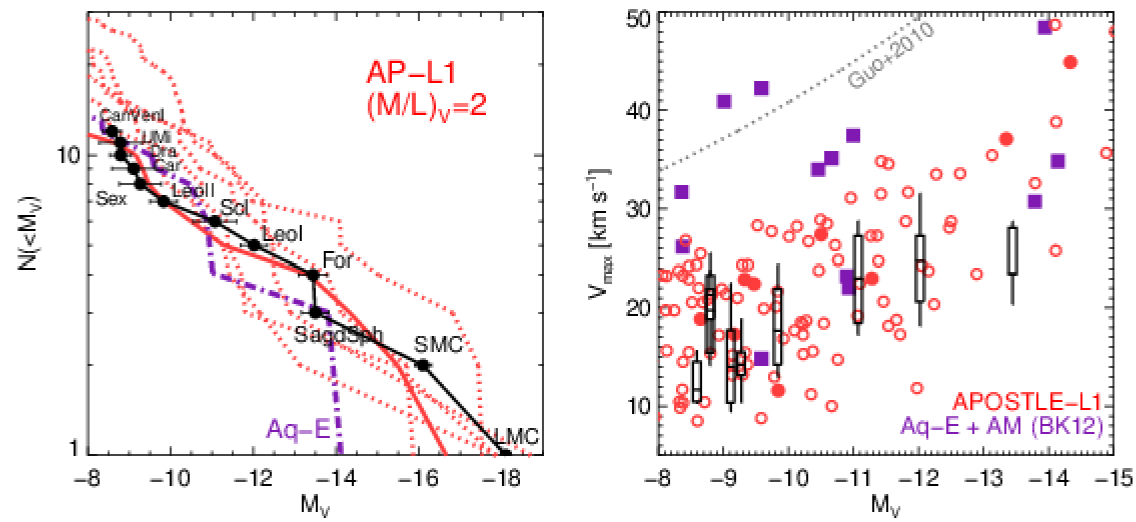

Figure 3.7 *Left*: Luminosity function of satellites of the six APOSTLE L1 primaries (dotted lines), compared with that of Galactic satellites (filled circles). We consider as satellites all systems within 300 kpc of the centre of each primary galaxy. We also show the luminosity function of the Aq-E halo (dot-dashed line) derived by Boylan-Kolchin et al. (2012) using an abundance matching model. The best fitting APOSTLE galaxy is highlighted with a solid line type. *Right*: $V_{\rm max}$–M_V relation for APOSTLE satellites (circles) compared with the abundance matching estimates for Aq-E subhaloes from Boylan-Kolchin et al. (2012). Box-and-whisker symbols indicate the $V_{\rm max}$ range of APOSTLE satellites that match the stellar mass and $V_{1/2}$ of each of the 9 Galactic dSphs (see Sec. 3.4.5 for details). APOSTLE satellites inhabit markedly lower mass haloes than expected from abundance matching, at a given luminosity. APOSTLE also differs from Aq-E in the number of massive substructures. On average, each APOSTLE primary has ~ 7.2 satellite more massive than $V_{\rm max} > 25\,{\rm km\ s^{-1}}$; this number is actually only 5 for the halo that best matches the MW satellite luminosity function (solid circles; two of them are brighter than $M_V = -15$). Aq-E has 21 satellites with $V_{\rm max}$ exceeding $25\,{\rm km\ s^{-1}}$, some of them fainter than $M_V = -8$.

fashion, so that a correction procedure is straightforward to devise and implement, at least for radii not too far inside $r_{\rm conv}$.

In Appendix 3.6, we describe the correction used to estimate the total mass enclosed within the Sculptor half-light radius for all Sculptor-like satellites in APOSTLE. The right-hand panel of Fig. 3.5 shows the APOSTLE $V_{1/2}$ estimates with and without correction. These estimates are obtained by randomly sampling the allowed range in $r_{1/2}$ as well as the $V_{\rm circ}(r_{1/2})$ distribution of Sculptor-like APOSTLE satellites. In brief, this procedure involves: (i) choosing a random value for $r_{1/2}$ consistent with propagating the Gaussian errors in distance modulus and angular size (see Sec. 4.3 and col. 7 of Table 3.1); (ii) measuring $V_{1/2} = V_{\rm circ}(r_{1/2})$ for a random satellite in AP-L1; and (iii) weighting[9] each APOSTLE satellite by how closely it matches Sculptor's stellar mass. (Although the procedure considers all satellites, in practice only Sculptor-like satellites contribute meaningfully, given the weighting procedure.)

The procedure is repeated $10,000$ times to derive the $V_{1/2}$ distribution shown in Fig. 3.5, which is then corrected for resolution as described in Appendix 3.6. In the case of Sculptor the correction to the measured $V_{1/2}$ values is relatively mild; the median $V_{1/2}$ shifts only slightly, from $13.9\,{\rm km\ s^{-1}}$ before correction to $15.7\,{\rm km\ s^{-1}}$. This is actually the case for the majority of systems; the largest correction is obtained for the Leo II dSph, where the median $V_{1/2}$ increases by 24 per cent, from $10.3\,{\rm km\ s^{-1}}$ to $12.8\,{\rm km\ s^{-1}}$. Satellites like Fornax, which have larger half-light radii well-resolved by APOSTLE, are corrected by less than 5 per cent.

We apply the same procedure outlined above to all 9 Galactic 'classical' dSph satellites (excluding Sagittarius) and compare our results with observational constraints in Fig. 3.6. The grey shaded regions and contours denote the observational estimates including uncertainties, while the red box-and-whisker symbols indicate the results for APOSTLE satellites. There is clearly substantial overlap between observational estimates of $V_{1/2}$ and the APOSTLE results for all 9 dSphs, with no exception.

The values of $\mu_{\rm sat}$ quoted in the legends of Fig. 3.6 indicate the absolute value of the difference between the mean observed and simulated values, in units of the combined rms: the difference is clearly not significant (less than unity) in any of the 9 cases. We conclude that the dark matter content of APOSTLE satellites is in good agreement with the observed values. We emphasize that this agreement is *not* the result of cored DM density profiles, as dwarf galaxies in APOSTLE show no evidence

[9]The weighting function is $\exp(-x^2/2\sigma^2)$, where $x = M_{\rm str}^{\rm AP} - M_{\rm str}^{\rm Scl}$, and σ is the uncertainty in Sculptor's stellar mass discussed in Sec. 4.3.

for cores (Oman et al., 2015; Sawala et al., 2016a).

We may assess the effect of tidal stripping on our conclusion by repeating the above procedure using APOSTLE centrals, rather than satellites, for the comparison. The results are shown by the blue box-and-whisker symbols in Fig. 3.6 (red and blue boxes are plotted with different widths, for clarity). The values of $V_{1/2}$ are systematically larger for centrals, since they have not experienced tidal stripping. The agreement is clearly poorer, in particular for satellites 'unusually large for their luminosities' (Sec. 3.4.3) like Can Ven I, Sextans, Carina, and Fornax.

Consistency between APOSTLE and Galactic satellites therefore requires that the dark matter content of at least some dSphs has been affected by tides from the Milky Way halo. We emphasize that *all* subhaloes have been affected by tides; their effects, however, are noticeable mainly in systems whose sizes are large enough for their kinematics to probe regions where the mass loss is significant. The strong dependence of the effect of tides on galaxy size must be taken carefully into account when comparing the dynamics of satellite and isolated field galaxies to search for signs of environmental effects (see, e.g., Kirby et al., 2014).

3.4.5 The too-big-to-fail problem revisited

The previous section demonstrates that there is no conflict between the dark matter content of APOSTLE satellites and that of Galactic dSphs. This does not *per se* solve the 'too-big-to-fail' problem laid out by Boylan-Kolchin et al. (2011b, 2012), which asserts that there is an excess of massive subhaloes without a luminous counterpart in Milky Way-sized haloes. Does this problem persist in APOSTLE?

We have examined this question earlier in Sawala et al. (2016a), but we review those arguments here in light of the revised uncertainties in the mass of the Galactic classical dwarf spheroidals discussed in Sec 4.3. Fig. 3.7 reproduces the argument given by Boylan-Kolchin et al. (2012). The solid squares in the right-hand panel of our Fig. 3.7 are taken directly from their Fig. 6 and show the maximum circular velocities of the 13 most luminous subhaloes in the Aq-E halo, selected because, according to an abundance matching model patterned after Guo et al. (2010), its number of satellites brighter than $M_V = -8$ matches that of the Milky Way. This is shown by the magenta dot-dashed line in the left-hand panel of Fig. 3.7. The offset between the Aq-E solid squares and the Guo et al. (2010) prediction (dotted line on right-hand panel) is mainly due to tidal stripping.

Our APOSTLE L1 simulations also reproduce well the MW satellite luminosity function (see dotted lines in left-hand panel), but they differ from the Boylan-Kolchin et al. (2012) analysis of Aq-E in two respects. One is that our subhaloes are, on average, significantly less massive, at a given M_V, than assumed for Aq-E. This is because the APOSTLE stellar mass – halo mass relation is offset from the extrapolation of abundance matching predictions (see Fig. 3.3). A question that arises is that whether this offset causes any discrepancy with other dwarf galaxies data. The only other available data are the rotation curves of gas-rich dwarf galaxies. By assuming that $V_{\rm max}$ is comparable to the outer most point of the rotation curve, Ferrero et al. (2012) show that these dwarf galaxies have lower mass than predicted by abundance-matching, at a fixes stellar mass; hence a discrepancy. The APOSTLE stellar mass–halo mass relation offsets from the abundance matching relation in the right direction to resolve the discrepancy (see also Oman et al., 2016).

The box-and-whisker symbols in the right-hand panel of Fig. 3.7 show the $V_{\rm max}$ values (Table 3.2) of APOSTLE satellites that best match the stellar mass *and* $V_{1/2}$ of each Galactic dSph. The procedure for estimating $V_{\rm max}$ is the same as that outlined in Sec. 3.4.4 for computing $V_{1/2}$ but, in addition, weights each simulated satellite by how closely it matches the observed $V_{1/2}$. These new $V_{\rm max}$ estimates complement and extend those reported by Sawala et al. (2016a).

The second difference concerns the number of massive substructures: Aq-E has 21 subhaloes with $V_{\rm max} > 25\,{\rm km~s^{-1}}$ within 300 kpc from the centre, 10 of which are more luminous than $M_V = -8$, according to the model of Boylan-Kolchin et al. (2012). On the other hand, APOSTLE L1 primaries have, on average, just 7.2 ± 2.5 subhaloes with $V_{\rm max} > 25\,{\rm km~s^{-1}}$ within the same volume. Indeed, the APOSTLE primary whose satellite population best matches the MW satellite luminosity function (solid red curve in the left-panel of Fig. 3.7) has only 5 subhaloes this massive, as indicated by the solid circles in the right-hand panel of the same figure. (Two of those host satellites brighter than $M_V = -15$.)

As discussed by Sawala et al. (2016a), the reason for the discrepancy is twofold. (i) Subhalo masses are systematically lower in cosmological hydrodynamical simulations because of the reduced growth brought about by the early loss of baryons caused by cosmic reionization and feedback. This reduces the $V_{\rm max}$ of all subhaloes by ~ 12 per cent. (ii) Chance plays a role too, as Aq-E seems particularly rich in massive substructures. The average number of subhaloes with $V_{\rm max} > 25\,{\rm km~s^{-1}}$ expected *within the virial radius* of a halo of virial mass $M_{200} = 1.2 \times 10^{12}\,{\rm M_\odot}$ is just 8.1 (Wang et al., 2012b), compared with 18 for Aq-E, a $> 3\sigma$ upward fluctuation. Note that the expected number would drop to just 5.4 after correcting for the ~ 12 per cent reduction in $V_{\rm max}$. Indeed, the subhalo velocity function is so steep that even a slight variation in $V_{\rm max}$ leads to a disproportionately large change in the number of massive substructures.

The discrepancy between APOSTLE and Aq-E noted above can therefore be ascribed to a chance upward fluctuation in the number of massive substructures in Aq-E coupled with the reduction of subhalo masses due to the loss of baryons in a hydrodynamical simulation.

3.4.6 TBTF and the mass of the Milky Way

The number of massive substructures is, of course, quite sensitive to the virial mass of the host halo. Following Wang et al. (2012b) and Cautun et al. (2014), we may use this to derive an upper limit to the mass of the Milky Way. In APOSTLE every subhalo with $V_{\rm max} > 25\,{\rm km\ s^{-1}}$ hosts a satellite brighter than $M_V = -8$ (or, equivalently, more massive than $M_{\rm str} \sim 10^5\,{\rm M_\odot}$; see the right-hand panel of Fig. 3.3). This means that any potential Milky Way host halo with more than ~ 12 subhaloes this massive will either suffer from a 'too-big-to-fail' problem or have an excess of luminous satellites.

We examine this in Fig. 3.8, which shows the number of massive subhaloes within r_{200} as a function of virial mass. The criterion above implies that, in the top panel, only systems below the dashed line labelled 'MW' are likely to reproduce well the MW satellite population. The grey band in the same panel shows the expected number ($\pm 1\sigma$) of massive substructures according to Wang et al. (2012b). Small (grey) open circles indicate the results from a 752^3-particle dark-matter-only simulation of a cube 25 Mpc on a side. Small (green) filled circles correspond to the same volume, but for a run including baryons and the full galaxy formation physics modules from the EAGLE project[10]. The offset between green and grey circles demonstrates the effect of the reduction of $V_{\rm max}$ caused by the inclusion of baryons in the simulation.

The six Aquarius haloes (Springel et al., 2008) are shown by starred symbols: these systems are slightly overabundant in massive substructures relative to both the EAGLE runs and the predictions of Wang et al. (2012b), which are based on large

[10] This simulation is labelled L0250752 in Schaye et al. (2015) and was run using the parameters of the 'Ref' model.

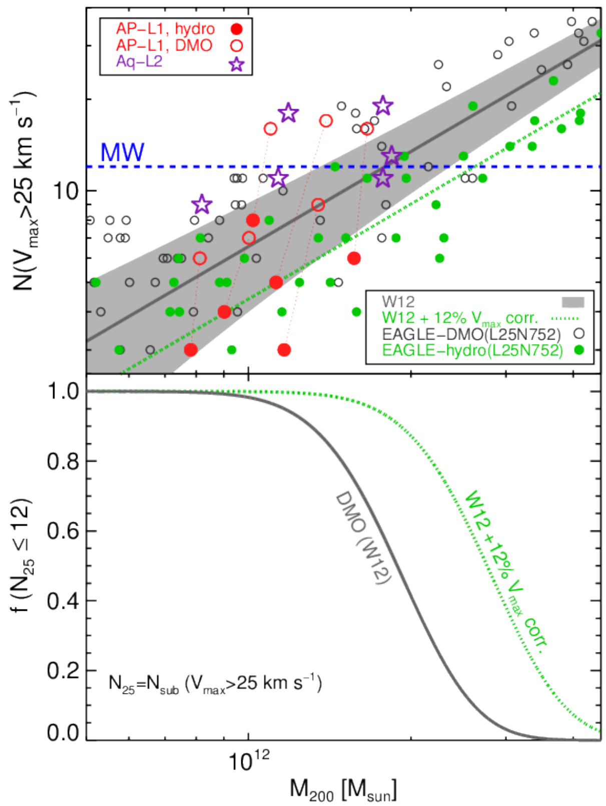

Figure 3.8 *Top*: Number of massive subhaloes ($V_{\rm max} > 25\,{\rm km\ s}^{-1}$) within r_{200}, shown as a function of virial mass, M_{200}, for APOSTLE-L1 (solid red circles) haloes and their DMO counterparts (open red circles), and Aquarius haloes (open stars). The results from EAGLE L0250752-Ref and its DMO counterpart are shown using small solid green circles and grey open circles, respectively. The prediction of Wang et al. (2012b, W12) with 1σ scatter is shown by the grey band. Including the 12 per cent reduction in $V_{\rm max}$ brings the W12 relation down to the green dotted line. The horizontal dashed line indicates the number of MW satellites brighter than $M_V = -8$. *Bottom*: The fraction of haloes with 12 or fewer massive subhaloes (i.e., $V_{\rm max} > 25\,{\rm km\ s}^{-1}$), as a function of the virial mass of the primary. The grey curve corresponds to the Wang et al. (2012b) estimate from dark-matter-only simulations. The green curve includes the 12 per cent reduction in $V_{\rm max}$ obtained in hydrodynamical simulations.

samples of haloes from the Millennium Simulations. Three Aquarius haloes have more than 12 massive substructures, and therefore would not be consistent with the MW satellite population according to our APOSTLE results.

Including baryons changes this, as shown by the six primaries in APOSTLE L1: these are shown in Fig. 3.8 with red circles; filled symbols for the hydrodynamical runs, and open symbols for the DMO versions. The DMO runs give results similar to Aquarius: half of APOSTLE DMO are above the 'MW' line. The number of massive substructures drops substantially once baryons are included (filled circles), so that all six primaries in the APOSTLE L1 hydrodynamical runs are actually consistent with the MW.

We may use these results to derive firm upper limits on the mass of the Milky Way. This is shown in the bottom panel of Fig. 3.8 where each curve traces the fraction of haloes of a given virial mass that have 12 (or fewer) massive substructures (i.e., the observed number of Galactic satellites brighter than $M_V = -8$). We show results for two cases; one where the numbers are derived from the formula of Wang et al. (2012b), assuming Poisson statistics (solid grey lines) and another where the zero-point of that relation has been shifted to account for the 12 per cent reduction in $V_{\rm max}$ discussed above (see green dotted line in the top panel of Fig. 3.8).

Clearly, the reduction in $V_{\rm max}$ induced by the loss of baryons in hydrodynamical simulations significantly relaxes the constraints based on dark-matter-only simulations. Indeed, according to this argument, fewer than 5 per cent of haloes more massive than $2.8 \times 10^{12}\,\mathrm{M}_\odot$ can host the Milky Way, assuming the DMO relation. The same criterion results in an increased mass limit of $4.2 \times 10^{12}\,\mathrm{M}_\odot$ adopting the $V_{\rm max}$ correction. This may also be compared with the earlier analysis of Wang et al. (2012b), which found an upper limit of $2 \times 10^{12}\,\mathrm{M}_\odot$, and of Cautun et al. (2014), which derived an even stricter limit, albeit using slightly different criteria.

3.5 Summary and Conclusions

We use the APOSTLE suite of ΛCDM cosmological hydrodynamical simulations of the Local Group to examine the masses of satellite galaxies brighter than $M_V = -8$ (i.e., $M_{\rm str} > 10^5\,\mathrm{M}_\odot$). Our analysis extends that of Sawala et al. (2016a), were we showed that our simulations reproduce the Galactic satellite luminosity function and show no sign of either the 'missing satellites' problem nor of the 'too-big-to-fail' problem highlighted in earlier work. Our main conclusions may be summarised as follows.

Previous studies have underestimated the uncertainty in the mass enclosed within the half-light radii of Galactic dSphs, derived from their line-of-sight velocity dispersion and half-light radii. Our analysis takes into account the error propagation due to uncertainties in the distance, effective radius, and velocity dispersion, and also include an estimate of the intrinsic dispersion of the modeling procedure, following the recent work of Campbell et al. (2016). The latter is important as it introduces a base systematic uncertainty that exceeds ~ 20 per cent.

Simulated galaxies in APOSTLE/EAGLE follow a stellar mass – halo mass relation that differs, for dwarf galaxies, from common extrapolations of abundance matching models, a difference that is even more pronounced for satellites due to tidal stripping, At fixed stellar mass, APOSTLE dwarfs inhabit halos significantly less massive than AM predicts. This difference, however, might not be readily apparent because tides strip halos from the outside in and some dSphs are too compact for tidal effects to be readily apparent.

We find that the dynamical mass of *all* Galactic dSphs is in excellent agreement with that of APOSTLE satellites that match their stellar mass. APOSTLE centrals (i.e., not satellites), on the other hand, overestimate the observed mass of four Galactic dSphs (Can Ven I, Sextans, Carina, and Fornax), suggesting that they have had their dark matter content significantly reduced by stripping. The other, more compact, dSphs are well fit by either APOSTLE satellites or centrals, so tides are not needed to explain their dark matter content.

After accounting for tidal mass losses, we find that all APOSTLE halos (satellites or centrals) with $V_{\rm max} > 25\,{\rm km\ s^{-1}}$ host dwarfs brighter than $M_V = -8$. Only systems with fewer than ~ 12 subhaloes with $V_{\rm max} > 25$ km/s are thus compatible with the population of luminous MW satellites. This suggests an upper limit to the mass of the Milky Way halo: we find that most halos with virial mass not exceeding $2 \times 10^{12}\,M_\odot$ should pass this test, unless they are unusually overabundant in massive substructures.

Our APOSTLE primaries satisfy these constraints, and show a dwarf galaxy population in agreement with observations of the Local Group, including their abundance as a function of mass, their dark matter content, and their global kinematics. Furthermore, APOSTLE uses the same galaxy formation model that was found by EAGLE to reproduce the galaxy stellar mass function in cosmologically significant volumes. We consider this a significant success for direct simulations of galaxy formation based on the ΛCDM paradigm.

We note that this success does not require any substantial modification to well-established properties of ΛCDM. In particular, none of our simulated dwarf galaxies have 'cores' in their dark mass profiles, but yet have no trouble reproducing the detailed properties of Galactic satellites. Baryon-induced cores are not mandatory to solve the 'too-big-to-fail' problem.

We end by noting that a number of recent studies have argued that TBTF-like problems also arise when considering the properties of M31 satellites (Tollerud et al., 2014; Collins et al., 2014), as well as those of field galaxies in the local Universe (Garrison-Kimmel et al., 2014; Papastergis et al., 2015). It remains to be seen whether the resolution we advocate here for Galactic satellites will solve those problems as well. We plan to report on those issues in future work.

3.6 Appendix A: Numerical Corrections

As discussed by Power et al. (2003), the enclosed mass profiles of N-body realizations of ΛCDM haloes converge outside a minimum radius, $r_{\rm conv}$, that depends on the number of particles enclosed and on the mean inner density of the halo at that radius. This is because simulated profiles converge only for radii where the two-body relaxation timescale is long compared with the age of the Universe. A criterion for convergence may thus be derived using the ratio of relaxation time to the circular velocity at the virial radius:

$$\kappa(r) = \frac{t_{\rm relax}(r)}{t_{\rm circ}(r_{200})} = \frac{N(r)}{8\,\ln\,N(r)}\frac{r/V_c}{r_{200}/V_{200}}, \tag{3.2}$$

which may also be written as,

$$\kappa(r) = \frac{\sqrt{200}}{8}\frac{N(r)}{\ln\,N(r)}\left(\frac{\bar{\rho}(r)}{\rho_{\rm crit}}\right)^{-1/2}. \tag{3.3}$$

where $N(r)$ is the enclosed number of particles and $\bar{\rho}(r)$ is the mean density inside the radius r. At radii where $\kappa \approx 1$ profiles converge to better than 10 per cent in terms of circular velocity. Stricter convergence demands larger values of κ and implies, consequently, larger values of $r_{\rm conv}$ (Navarro et al., 2010).

Fig. 3.9 illustrates this for the case of the dark-matter-only realizations of four different APOSTLE primary haloes, run at three different resolutions, each differing

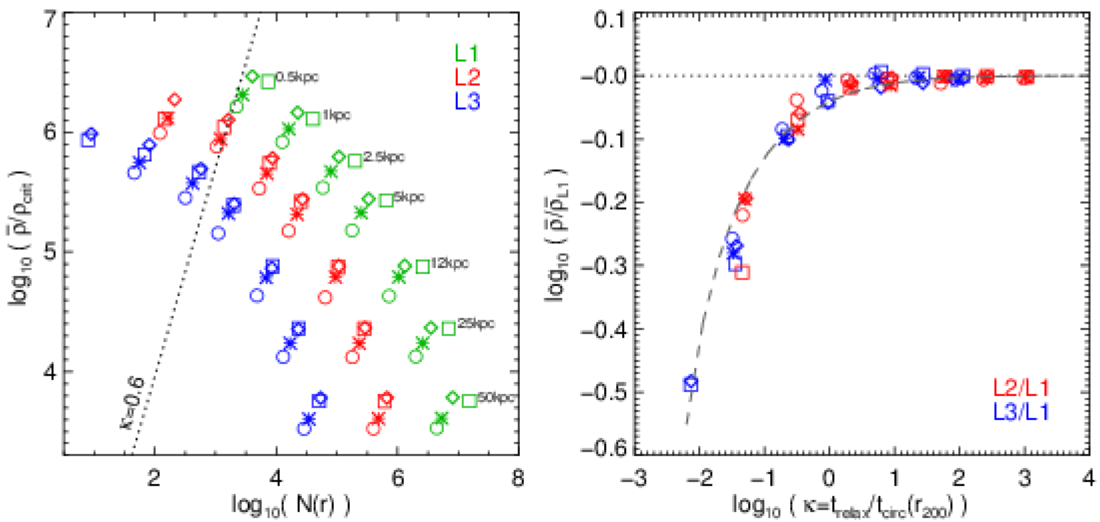

Figure 3.9 *Left*: Mean inner density as a function of enclosed number of particles at different radii, as labelled, for 4 primary haloes in dark-matter-only APOSTLE, simulated at three different resolution levels (L1 to L3). Different haloes are shown by different symbols, and colours indicate different resolution levels. Points to the right of the $\kappa = 0.6$ line (eq. 3.3) converge in circular velocity to better than 15 per cent (Power et al., 2003). Two L3 haloes have fewer than 5 particles at the smallest radius, and are not shown. *Right*: Mean inner density as a function of κ for L2 and L3 haloes, normalized to the values obtained for the highest-resolution run, L1. Symbols are the same as in the left panel. The dashed line has been used to correct densities at small radii.

by about a factor of ~ 10 in particle mass and ~ 2 in force resolution (L1 to L3, where L1 is best resolved).

The left panel of Fig. 3.9 shows the mean enclosed density at various radii. Different colours indicate the various resolution levels, whereas different symbols correspond to different haloes. At large radii all resolutions converge to the same result (i.e., like symbols line up horizontally). At small radii, however, the lower-resolution profiles gradually deviate from the highest-resolution (L1) run. The Power et al. (2003) criterion is shown by the inclined dotted line, for $\kappa = 0.6$. Note that points clearly converge, regardless of resolution, to the right of this line, but those on the left deviate noticeably from the results obtained for the highest-resolution case, L1.

The smooth trend in density contrast with enclosed particle number suggests a simple way to correct an under-resolved halo profile. Indeed, expressed in terms of κ, the 'deficit' in density observed in the inner regions always follows the same pattern. This is shown in the right-hand panel of Fig. 3.9, where we show, for all radii $\geq 0.5\,\mathrm{kpc}$ and all haloes, the density in units of the 'true' values obtained for L1. All haloes follow the same pattern, which we approximate with a fitting function, $\log(1 - \bar{\rho}/\bar{\rho}_{\rm conv}) = a(\log\kappa)^2 + b(\log\kappa) + c$ where (a,b,c)=(-0.04,-0.5,-1.05).

Since densities of L1 are 'converged' according to the left-hand panel of Fig. 3.9 ($\bar{\rho}_{\rm L1} = \bar{\rho}_{\rm conv}$), the aforementioned trend may be used to extrapolate the results of a simulation to radii smaller than the traditional value of $r_{\rm conv}$ dictated by assuming $\kappa = 0.6$.

We show in Fig. 3.10 the results of applying this correction to Sculptor-like central galaxies in APOSTLE-L1. Typical values of κ at $r_{1/2}$ for this galaxy are about 0.15, which results in a correction in enclosed density of roughly 20 per cent. The distribution shown in the right-hand panel of Fig. 3.10 is then used statistically to correct the raw $V_{1/2}$ estimates from our L1 satellites. The result of applying this to Sculptor-like satellites is shown in Fig.3.5. This same procedure is applied separately to each Galactic satellite in order to derive the predictions shown in Fig. 3.6.

3.7 Appendix B: Tables

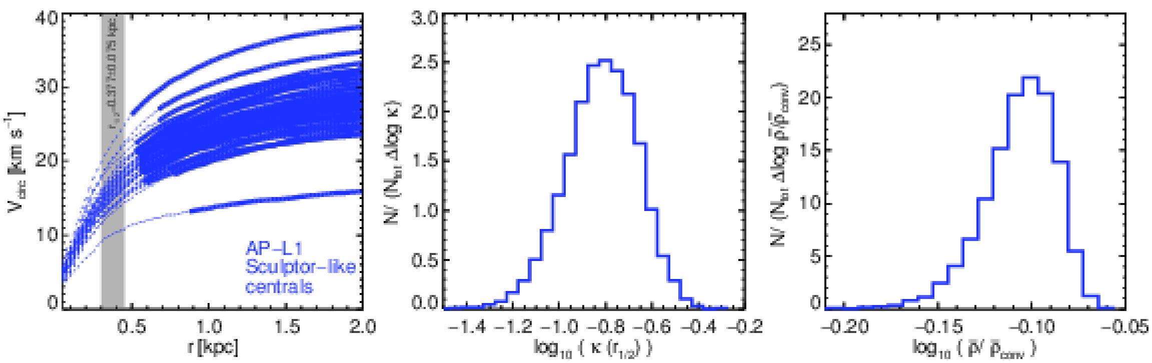

Figure 3.10 *Left*: Circular velocity curves of Sculptor-like APOSTLE centrals. The grey band corresponds to the 10–90$^{\rm th}$ percentile interval for the observed $r_{1/2}$ of Sculptor. *Middle*: Distribution of $\kappa(r) = t_{\rm relax}(r)/t_{\rm circ}(r_{200})$ for the rotation curves in the left panel, at radii consistent with the $r_{1/2}$ of Sculptor. *Right:* Distribution of the density correction factor derived from the κ distribution of the middle panel and the fit presented in the right panel of Fig. 3.9.

Table 3.1 The parameters of classical dSph satellites of MW.

name	$(m-M)_0$	$R_{\rm eff}$	$\sigma_{\rm los}$	m_V	$\frac{M_{\rm str}}{L_V}$	3D $r_{1/2}$	$M_{1/2}$	$V_{1/2}$	$M_{\rm str}$
		(arcmin)	(km s^{-1})			(pc)	(10^7 M$_\odot$)	(km s^{-1})	(10^6 M$_\odot$)
ref.	(a)			(a)	(b)				
For	20.84 ± 0.18	$16.6 \pm 1.2^{a,c}$	11.7 ± 0.9^f	7.4 ± 0.3	1.2	$950^{+70(140)}_{-70(130)}$	$8.9^{+1.9(3.8)}_{-1.7(3.0)}$	$20.1 \pm 1.9(3.6)$	$24^{+6(13)}_{-5(9)}$
Leo I	22.02 ± 0.13	$3.4 \pm 0.3^{a,c}$	9.2 ± 1.4^g	10.0 ± 0.3	0.9	$334^{+24(47)}_{-24(44)}$	$1.9^{+0.6(1.2)}_{-0.6(0.8)}$	$15.8 \pm 2.0(3.9)$	$5.0^{+1.1(2.4)}_{-1.0(1.7)}$
Scl	19.67 ± 0.14	$11.3 \pm 1.6^{a,c}$	9.2 ± 1.1^f	8.6 ± 0.5	1.7	$377^{+40(77)}_{-39(73)}$	$2.2^{+0.6(1.2)}_{-0.5(0.9)}$	$15.8 \pm 1.8(3.4)$	$3.9^{+1.5(3.4)}_{-1.1(1.8)}$
Leo II	21.84 ± 0.13	$2.6 \pm 0.6^{a,c}$	6.6 ± 0.7^h	12 ± 0.3	1.6	$235^{+38(73)}_{-38(71)}$	$0.68^{+0.21(0.4)}_{-0.17(0.3)}$	$11.3 \pm 1.2(2.3)$	$1.2^{+0.3(0.6)}_{-0.2(0.4)}$
Sex I	19.67 ± 0.10	$27.8 \pm 1.2^{a,c}$	7.9 ± 1.3^f	10.4 ± 0.5	1.6	$926^{+40(77)}_{-39(73)}$	$3.9^{+1.2(2.5)}_{-1.0(1.7)}$	$13.5 \pm 1.9(3.5)$	$0.7^{+0.3(0.6)}_{-0.2(0.3)}$
Car	20.11 ± 0.13	$8.2 \pm 1.2^{a,c}$	6.6 ± 1.2^f	11.0 ± 0.5	1.0	$334^{+36(69)}_{-35(66)}$	$1.0^{+0.3(0.7)}_{-0.3(0.5)}$	$11.3 \pm 1.7(3.1)$	$0.38^{+0.14(0.32)}_{-0.11(0.18)}$
UMi	19.40 ± 0.10	19.9 ± 1.9^d	9.5 ± 1.2^i	10.6 ± 0.5	1.9	$584^{+42(82)}_{-41(78)}$	$3.6^{+1.0(2.0)}_{-0.8(1.4)}$	$16.3 \pm 1.9(3.6)$	$0.54^{+0.21(0.46)}_{-0.15(0.25)}$
Dra	19.40 ± 0.17	$10.0^{+0.3,e}_{-0.2}$	9.1 ± 1.2^j	10.6 ± 0.2	1.8	$294^{+17(33)}_{-16(30)}$	$1.7^{+0.5(0.9)}_{-0.4(0.7)}$	$15.6 \pm 1.9(3.6)$	$0.51^{+0.09(0.20)}_{-0.09(0.15)}$
CVn I	21.69 ± 0.10	8.9 ± 0.4^e	7.6 ± 0.4^k	13.1 ± 0.2	1.6	$751^{+34(64)}_{-32(60)}$	$3.0^{+0.5(1.1)}_{-0.5(0.9)}$	$13.1 \pm 1.1(2.1)$	$0.37^{+0.06(0.13)}_{-0.05(0.10)}$

Notes: Uncertainties in the observed parameters are taken directly from the references. We assume in all cases that they correspond to standard deviations of a Gaussian error distribution. The uncertainties quoted for derived parameters, i.e. the last four columns, correspond to interquartile and 10–90$^{\rm th}$ percentile intervals, written outside and inside parentheses, respectively.

References: [a]McConnachie (2012); [b]Woo et al. (2008); [c]Irwin & Hatzidimitriou (1995); [d]Palma et al. (2003); [e]Martin et al. (2008); [f]Walker et al. (2009b); [g]Mateo et al. (2008); [h]Koch et al. (2007); [i]Walker et al. (2009a); [j]Walker et al. (2007); [k]Simon & Geha (2007).

Table 3.2 Parameters of APOSTLE satellites matching the stellar mass of Galactic classical dSph satellites.

	$M_{1/2}$ ($10^7\,\mathrm{M}_\odot$)	$V_{1/2}$ (km s^{-1})	$V_{\rm max}$ (km s^{-1})
Fornax-like (14)	$13^{+3(6)}_{-3(5)}$	$25.5^{+1.8(3.4)}_{-4.0(5.1)}$	$23.0^{+4.6(4.6)}_{-0(3.07)}$
Leo I-like (37)	$2.0^{+0.5(1.0)}_{-0.5(0.8)}$	$16.2^{+1.5(3.1)}_{-1.7(3.3)}$	$24.7^{+2.6(6.7)}_{-4.1(6.5)}$
Sculptor-like(56)	$2.1^{+0.8(1.6)}_{-0.6(1.2)}$	$15.7^{+2.0(4.0)}_{-1.9(4.4)}$	$23.0^{+4.2(5.5)}_{-4.6(5.7)}$
Leo II-like(50)	$0.9^{+0.5(1.0)}_{-0.4(0.6)}$	$12.8^{+2.3(4.4)}_{-2.4(4.6)}$	$17.7^{+4.0(6.6)}_{-3.5(4.5)}$
Sextans-like(89)	$7.1^{+2.7(4.2)}_{-2.3(4.6)}$	$18.2^{+3.0(4.4)}_{-3.4(7.4)}$	$14.2^{+1.2(4.1)}_{-1.1(3.8)}$
Carina-like(117)	$1.4^{+0.6(1.2)}_{-0.5(0.8)}$	$13.8^{+2.0(3.9)}_{-3.0(4.7)}$	$14.0^{+3.2(8.0)}_{-3.7(4.5)}$
Ursa Minor-like(95)	$3.7^{+1.2(2.4)}_{-1.1(2.3)}$	$16.6^{+2.6(4.1)}_{-4.2(5.7)}$	$19.8^{+2.2(4.0)}_{-4.3(5.6)}$
Draco-like(48)	$1.3^{+0.4(0.8)}_{-0.4(0.8)}$	$14.7^{+1.9(3.1)}_{-1.7(5.1)}$	$21.3^{+1.9(4.1)}_{-2.5(6.0)}$
Canes Venatici I-like(45)	$5.3^{+2.0(3.0)}_{-2.6(3.4)}$	$17.6^{+2.9(4.1)}_{-5.2(7.2)}$	$11.7^{+2.8(3.8)}_{-1.2(1.8)}$

Notes: Values of $M_{1/2}$ and $V_{1/2}$ have been corrected by the procedure outlined in Appendix 3.6. $V_{\rm max}$ values are obtained by matching the stellar mass *and* $V_{1/2}$ of APOSTLE satellites to those of MW satellites. See text for details. Numbers quoted in parentheses after the names are the number of simulated satellites matching the stellar mass of the corresponding MW dSph. Similar to Table 3.1, uncertainties represent interquartile and 10–90$^{\rm th}$ percentile intervals, written outside and inside parentheses, respectively.

Chapter 4

Tidal stripping of Local Group dwarf spheroidals within ΛCDM

4.1 Abstract

According to the APOSTLE cosmological hydrodynamical simulations within the ΛCDM framework, all *isolated* luminous dwarf galaxies are expected to live in haloes in a very narrow range of the maximum circular velocity around $25\,\mathrm{km\ s^{-1}}$, and therefore, follow a universal halo mass profile. The enclosed mass within the half-light radii of LG classical and ultra faint satellites, derived using their velocity dispersions, indicates that some of them contain, at times significantly, less dark matter than expected from the universal profile. Tidal stripping, as a plausible mechanism responsible for their low masses, is additionally supported by the large half light radii of these satellites.

By tracking the evolution of stellar mass, velocity dispersion and size of satellites back in time, we show that the same degree of stripping required to explain the mass deficit of satellites compared to the universal mass profile, will move the large satellites amongst the average size field galaxies. Our analysis shows that Cra II amongst Milky Way satellites, and And XIX, XXI, and XXV amongst M31 satellites have been extremely stripped. They have lost 99 per-cent of their *stellar mass*. We check that this high degree of stripping is not contradictory to the metallicity relations and dynamical mass-to-light ratios of these dwarfs.

Additionally, Dwarf spheroidals also show a much larger scatter on $g_{\mathrm{obs}}-g_{\mathrm{bar}}$ plane, as oppose to the tight relation expected from MOND. Tidal stripping introduces

scatter on the $g_{\rm obs} - g_{\rm bar}$, and brings the observed acceleration of dwarf galaxies lower than $a_{\rm min} \sim 10^{-11}\,{\rm m\,s^{-2}}$, the minimum expected for isolated dwarfs. Highly stripped satellites in APOSTLE move towards the MOND prediction in g-g plane; another support for high degree of stripping for satellites such as Cra II. Finally we show that the measured velocity dispersions of dwarf spheroidals, in particular the ultra faint ones, are inconsistent with MOND predictions based on their stellar masses and positions around their hosts.

4.2 Introduction

The standard model of cosmology, Lambda-Cold Dark Matter (ΛCDM), has a clear prediction for the shape of the dark halo mass function. The predicted halo mass function is rather steep compared to the shape of the galaxy mass function at the low mass end; resulting in a large discrepancy between the observed number of dwarf galaxies and the predicted number of low mass haloes, as the potential sites of galaxy formation. In an attempt to match the abundance of galaxies and haloes while keeping their mass ranking, the "abundance-matching" techniques will result in a sharp drop in the galaxy formation efficiency [1] towards low mass haloes, such that *all* dwarf galaxies are expected to form in haloes in a very narrow range of halo mass around virial[2] mass of $M_{200} \sim 10^{10}\,{\rm M_\odot}$ (corresponding to the maximum circular velocity of $V_{\rm max} \sim 30\,{\rm km\ s^{-1}}$). The current models of galaxy formation account for the low galaxy formation efficiency using the cosmic UV/X-ray background and stellar/supernovae feedback, which prevent gas from cooling and forming into stars in low mass haloes (Bullock et al., 2000; Benson et al., 2002).

Despite the predicted cut-off of $V_{\rm max} \sim 30\,{\rm km\ s^{-1}}$ for haloes which host galaxies, the velocity dispersion of dwarf spheroidals (dSphs) of the Local Group (LG) combined with their size, indicate velocities well below what is expected for a $V_{\rm max} = 30\,{\rm km\ s^{-1}}$ halo (Read et al., 2006). Given that almost all dSphs are satellites of either the MW or M31, with the exception of Cetus and Tucana, the influence of environment on the evolution of these gas-free galaxies is clear. Tidal stripping by the gravitational field of the host is considered the main mechanism for removing their mass and bringing down their velocity dispersion (Peñarrubia et al., 2008).

[1] galaxy formation efficiency is defined as galaxy mass normalized by halo mass

[2] virial quantities are defined at the radius where the mean enclosed density is 200 times the critical density for closure. The virial parameters are indicated with a 200 subscript

Tidal stripping alone, however, can not solve the "too-big-to-fail" problem (TBTF) introduced by Boylan-Kolchin et al. (2012), who showed that the MW brightest dSphs are not dense enough to be consistent with the most massive subhaloes around the Aquarius MW-sized haloes (Springel et al., 2008).

One proposed solution of the TBTF problem is lowering the virial mass of the MW (Wang et al., 2012a; Cautun et al., 2014), which is quite uncertain (see, e.g., Wang et al., 2015). Other common solutions of the problem rely on altering the central dark matter density profile of the satellites, and change it from the cuspy form expected in ΛCDM (Navarro et al., 1996b, 1997, NFW hereafter) to a centrally flat (cored) profile. This solution which connects the "core-cusp" and the TBTF problems, works by bringing down the circular velocity in the inner regions of haloes, into agreement with observations (Oñorbe et al., 2015; Zolotov et al., 2012). Additionally, the cored dark matter profiles make the satellites more susceptible to tidal effects by the host's DM halo or baryonic disk (Peñarrubia et al., 2010; Brooks & Zolotov, 2014; Errani et al., 2015).

Production of DM cores in ΛCDM hydrodynamical simulations are dependent on the details of the star formation and supernovae feedback implementations. Additionally, the cores are produced in relatively bright dwarf galaxies with stellar mass above $10^7\,M_\odot$ (Madau et al., 2014; Di Cintio et al., 2014; Pontzen & Governato, 2014); fainter systems do not produce sufficient baryonic feedback to alter the distribution of DM. Therefore, cored profiles can not explain the low velocity dispersion of (ultra) faint satellites. On the observational side, the existence and/or importance of cores are still debated (Oman et al., 2015); in particular, for dSphs whose circular velocities are not observable (Walker & Peñarrubia, 2011; Strigari et al., 2010, 2017; Campbell et al., 2016).

Using the APOSTLE hydrodynamical simulations of the LG, Sawala et al. (2016a) recently showed that the mass (within the half light radius) of MW classical dSphs are in perfect agreement with the ΛCDM simulated satellites, and there is no TBTF problem of MW satellites in APOSTLE, even though DM profiles are cuspy in the simulations (Schaller et al., 2015c; Oman et al., 2015). The solution relies on the reduction of halo mass in hydrodynamical simulations compared to their N-Body counterparts (Sawala et al., 2013). Moreover, the stellar mass-halo mass relation at the faint end in APOSTLE is different than the abundance-matching relations (Sawala et al., 2015), even though it still shows a sharp decline in the galaxy formation efficiency at the faint end. Essentially, the stellar mass-halo mass of APOSLTE galaxies combined with tidal stripping is enough to explain the mass of MW classical dSphs.

In this paper we are planning to extend the analysis, and the observational sample to M31 satellites and ultra faint galaxies, to test whether these galaxies are consistent with being born in similar haloes, in agreement with the APOSTLE prediction. Strigari et al. (2008) and Walker et al. (2009a), indeed, conclude that MW satellites are broadly consistent with living in a common halo. On the other hand, by measuring the velocity dispersion of a large sample of M31 satellites, Collins et al. (2014) show that M31 satellites do not share a common mass profile, as suggested by the two previous works (see also, Tollerud et al., 2014). In particular, a number of M31 satellites, e.g. And XIX, XXI or XXV, have unusually small velocity dispersions of around $3-4\,\mathrm{km\ s^{-1}}$. Collins et al. (2014) suggest tidal stripping as the source of their low velocity dispersions. It is, however, unclear whether stripping can explain other properties of these galaxies.

Since the previous studies, a large number of (ultra) faint dSphs have been discovered around the MW in the footprints of the Dark Energy Survey, VST-ATLAS survey, Pan-STARRS, and SDSS (Bechtol et al., 2015; Drlica-Wagner et al., 2015; Koposov et al., 2015; Kim et al., 2015; Kim & Jerjen, 2015; Martin et al., 2015; Belokurov et al., 2014; Laevens et al., 2014, 2015b,a), and stellar kinematic measurements have become available for many more ultra faint dwarfs. In addition to ultra faint dwarfs, a new peculiar MW satellite has been discovered: Crater II, with a luminosity similar to Draco, is amongst the lowest velocity dispersion satellites, but has one of the largest half-light radii (Torrealba et al., 2016; Caldwell et al., 2017). The properties of this galaxy can raise challenges for ΛCDM; and studies have shown that this galaxy is consistent with MOND predictions (McGaugh, 2016; Caldwell et al., 2017).

A common minimum mass scale for isolated dwarf galaxies will also manifest itself in the mass discrepancy-acceleration relation (MDAR), a relation between the total observed acceleration of galaxies and their baryonic surface density, observed for spiral galaxies (Milgrom, 1983; McGaugh et al., 2016). As discussed in Navarro et al. (2016), the minimum halo mass imposes a minimum observed acceleration of $10^{-11}\,\mathrm{m\,s^{-2}}$, which is quite different from the MOND prediction for the low surface brightness galaxies. Galaxies such as Crater II (Cra II), which probe accelerations much lower than $10^{-11}\,\mathrm{m\,s^{-2}}$ can only be explained through tidal stripping. Exploring these outliers such as Cra II, And XXI or XXV, therefore, will shed light on the viability of our understanding of galaxy formation and underlying cosmology.

Here, we address the tidal stripping of LG satellites and the scenario that they originated from a similar halo mass. We track satellites backward using the work of Peñarrubia et al. (2008), and predict how much they should have been stripped to be in agreement with APOSTLE predictions. We discuss the MDAR of dwarf galaxies in the light of tidal stripping. The paper is organized as follows. Sec. 4.3 describes the observational sample we use in this study, along with deriving their mass within their (deprojected) half light radii. APOSTLE hydrodynamical simulations are introduced in Sec. 4.4, followed by comparing the LG dwarf mass measurements with that of APOSTLE predictions in Sec. 4.5.1. We introduce our method of tracking satellites' properties and find their progenitors in Sec. 4.5.2.1. The rest of Sec. 4.5 explores the properties of the progenitors. We examin the MDAR relation of LG dwarfs in Sec. 4.6.1, and the MOND predictions for velocity dispersion of dwarfs in Sec. 4.6.2. We end by the discussion and conclusion in Sec. 4.7.

4.3 Observational data and the mass of dwarf spheroidals

The mass of dispersion supported stellar systems, such as dwarf spheroidals, can be estimated within their half-light radii, under the assumptions of equilibrium and sphericity (Walker et al., 2009a; Wolf et al., 2010). Wolf et al. (2010) have shown that the following equation can be used to estimate the enclosed mass within the 3D (deprojected) half-light radius ($r_{1/2}$) of such systems:

$$M_{1/2} = 3\, G^{-1}\, \sigma_{\rm los}^2\, r_{1/2}, \tag{4.1}$$

where $\sigma_{\rm los}$ is the luminosity-weighted line-of-sight velocity dispersion of the stars and $r_{1/2}$ has been derived from the effective radius, $R_{\rm eff}$, using $r_{1/2} = (4/3)R_{\rm eff}$.

In this work, we use the Wolf et al. mass estimator to calculate $M_{1/2}$ for all dwarf galaxies in the LG with available velocity dispersion and half-light radius measurements. We mainly work in the velocity space and use the circular velocity at $r_{1/2}$, instead of $M_{1/2}$:

$$V_{1/2} = \sqrt{GM_{1/2}/r_{1/2}} = \sqrt{3} \times \sigma_{\rm los} \tag{4.2}$$

We use the updated version of the compilation of McConnachie (2012) as the base of the observational data for dwarfs in and around the LG [3]. We update the data if more recent measurements are available. Distance modulus, angular half-light radius, and stellar velocity dispersion are used for estimating $V_{1/2}$ at $r_{1/2}$. We also derive the stellar mass of dwarfs, $M_{\rm str}$, from the distance modulii and v-band magnitudes, along with stellar mass-to-light ratios derived in Woo et al. (2008). For cases where stellar mass-to-light ratios were not derived in Woo et al. (2008), we adopt $M_{\rm str}/L_{\rm V} = 1.6$ and $M_{\rm str}/L_{\rm V} = 0.7$ for dSphs and Irregulars, respectively. observational measurements used in this work

Uncertainties in $M_{1/2}$ (or $V_{1/2}$), $M_{\rm str}$, and $r_{1/2}$ are derived by propagating the errors in relevant observed quantities using the Monte-Carlo methods. Since Woo et al. (2008) do not report the individual uncertainties on stellar mass-to-light ratios, we assume a constant 10 per-cent uncertainty for all dwarfs. After propagating the observational errors in deriving $M_{1/2}$, we add in quadrature an additional 20 per-cent uncertainty following the work of Campbell et al. (2016). They used the hydrodynamical simulation suite of APOSTLE to show that the Wolf et al. estimator can recover the $M_{1/2}$ of dispersion supported dwarfs with a 20 per-cent uncertainty. The details of this procedure is illustrated in the previou chapter.

In order to use a homogeneous mass estimate, or $V_{1/2}$, my main analysis in this paper involves systems with velocity dispersion and half-light radius measurements. We note that some LG field galaxies and dwarf ellipticals of M31 show signs of rotation in their stellar component, and a more careful treatment of stellar kinematics is needed to estimates their masses which is beyond the scope of our paper. Since the dispersion is dominated over the rotation of stars, we chose to neglect the rotation for the sake of simplicity. Moreover, the main focus of our study is on dwarf spheroidal satellites, which are all dispersion supported.

Galaxies with no velocity dispersion measurements appear in some plots where we show quantities independent of $V_{1/2}$.

The following definitions for different subgroups within the LG were adopted throughout this work:

- **Milky Way satellites**: All galaxies within 300 kpc of the centre of the MW. Classical satellites are referred to those brighter than $M_{\rm V} = -8$. Good quality measurements are available for all classical dSphs of the MW. We also include newly discovered ultra faint dwarfs where data is available.

[3]We use the October 2015 version from http://www.astro.uvic.ca/~alan/Nearby_Dwarf_Database.html

- **M31 satellites**: All galaxies within 300 kpc (in 3D) from the centre of the M31. The same as above, classical satellites refer to those brighter than $M_{\rm V} = -8$, whereas fainter satellites are referred to as ultra faints. Velocity dispersion measurements are available for many M31 satellites, from the works of Collins et al. (2013) and Tollerud et al. (2012). For satellites with double measurements of their velocity dispersions, we adopt the estimate based on the higher number of member stars. Structural parameters of M31 satellites within the PAndAS footprint (McConnachie et al., 2009) are updated to the new measurements by Martin et al. (2016).

- **LG field members**: Any dwarf galaxy who is located further then 300 kpc from either the MW or M31, but is within 1.5 Mpc of the barycentre of the LG[4]. This definition is motivated by the work of McConnachie (2012) and the zero-velocity surface of the LG; galaxies further than 1.5 Mpc are receding from the LG with the Hubble flow. Velocity dispersion measurements are available for most of these field dwarfs. Majority of them were obtained by Kirby et al. (2014).

- **Nearby galaxies**: Any galaxy in the compilation of McConnachie (2012) which is further than 1.5 Mpc from the barycentre of the LG. This dataset includes galaxies with accurate distance estimates based on high precision methods, such as TRGB. The furthest galaxies in the sample are located at the distance of ~ 3 Mpc from the centre of the MW. Velocity dispersion measurement are not available for this galaxies. We use the data for their stellar mass, half-light radius, and metallicity.

The matellicities used in our plots are taken from McConnachie (2012), updated for a few recent measurements regarding ultra faint dwarfs.

4.4 The Simulations

In this study, we use cosmological, hydrodynamical simulations of the APOSTLE project. The APOSTLE suite includes zoom-in simulations of 12 volumes resembling kinematics of the MW–M31 pair and the surrounding. We refer the interested reader to Sawala et al. (2016a) and Fattahi et al. (2016a) for a full description of the candidate

[4]barycentre is calculated assuming equal masses for MW and M31

selection and the simulations. In summary, 12 LG candidates ware selected from the DOVE dark-matter only simulation of a periodic box of $100^3\,\mathrm{Mpc}^3$ (Jenkins, 2013). Each simulation candidate contains a relatively isolated pair of halo with virial mass $M_{200} \sim 10^{12}\,\mathrm{M}_{\odot}$, separated by $d = 600 - 1000$ kpc, and approaching each other with $V_{\mathrm{r}} = 0 - 250\,\mathrm{km\ s}^{-1}$. The relative tangential velocity of the pair members were constrained to be less than $100\,\mathrm{km\ s}^{-1}$, and the Hubble flow of structures around each pair is consistent with the observations. Each zoom-in volume is clean of boundary contaminating particles out to 2-3 Mpc from the barycentre of MW-M31 analogs.

The candidates were simulated at three different levels of resolution, labelled L1 to L3, using the code developed for the EAGLE project (Schaye et al., 2015; Crain et al., 2015). The code is a highly modified version of the Tree-PM/smoothed particle hydrodynamics code, P-Gadget3 (Springel, 2005). The hydrodynamical forces are calculated using the pressure-entropy formalism of Hopkins (2013), and the subgrid physics model was calibrated to reproduce the stellar mass function of galaxies at $z = 0.1$ in the stellar mass range of $M_{\mathrm{str}} = 10^8 - 10^{12}\,\mathrm{M}_{\odot}$, and realistic galaxy sizes. The complex galaxy formation subgrid model includes metallicity dependant star formation and cooling, metal enrichment, stellar and supernova feedback, homogeneous X-ray/UV background radiation (re-ionization), supermassive black-hole, and AGN activity. The resulting rotation curves of simulated galaxies are in good agreement with observations (Schaller et al., 2015b). The details of the subgrid model can be found in Schaye et al. (2015), Crain et al. (2015), and Schaller et al. (2015a). APOSTLE project adopts the parameters of the 'ref' model in the language of the aforementioned papers.

Haloes and bound (sub)structures in the simulations are found using the FoF algorithm and SUBFIND, respectively. First, FoF is run on the DM particles, with linking length 0.2 times the mean inter-particle separation, for finding the haloes. Gas and star particles association to haloes are determined according to their nearest DM particle. In the second step, SUBFIND searches iteratively for bound (sub)structures of any given FoF halo using *all* particle types associated to it. We shall refer to MW and M31 analogs as primary haloes.

Throughout this paper we use the highest resolution simulations, L1, with gas particle mass of $\sim 10^4\,\mathrm{M}_{\odot}$, and force softening length of 134 pc. 4 simulation volumes are available at the resolution level L1, corresponding to AP-01, AP-04, AP-06, AP-11 in table 2 of Fattahi et al. (2016a).

The simulations adopt cosmological parameters consistent with 7-year *Wilkinson*

Microwave Anisotropy Probe (WMAP-7, Komatsu et al., 2011) measurements, as follows: $\Omega_m = 0.272$, $\Omega_\Lambda = 0.728$, $h = 0.704$, $\sigma_8 = 0.81$, $n_s = 0.967$.

4.5 Results

4.5.1 Dark matter content of LG dwarf galaxies

A natural outcome of the simulations is the relation between stellar mass and dark halo mass. In the top panel of Fig. 4.1, we show stellar mass versus the maximum of the circular velocity, $V_{\rm max}$, for field galaxies and satellites in APOSTLE [5], shown as red crosses and blue circles, respectively. Stellar masses for the field galaxies are measured within $r_{\rm gal} = 0.15\, r_{200}$. For the satellites, r_{200} is not well defined, and we use the relation between $r_{\rm gal}$ and $V_{\rm max}$ of centrals, $r_{\rm gal}/{\rm kpc}{=}\ 0.169\, (V_{\rm max}/\ {\rm km\ s^{-1}})^{1.01}$, to estimate their $r_{\rm gal}$.

The top panel of Fig. 4.1 shows that APOSTLE field galaxies form a tight and very steep relation in $M_{\rm str} - V_{\rm max}$ plane. The steep behaviour of the relation is not surprising, given that APOSTLE reproduces the stellar mass function of the LG very well (Sawala et al., 2016a), while the number of dark matter subhaloes around LG analogs is orders of magnitude larger. We, however, note that the agreement with observed stellar mass function could be achieved even if the $M_{\rm str} - V_{\rm max}$ relation was more stochastic, but this scenario comes with the expense of keeping some of the massive ($V_{\rm max} > 20\,{\rm km\ s^{-1}}$) (sub)halos empty of stars. The dotted line in this panel corresponds to the power-law extrapolation of Guo et al. (2010) abundance-matching relation.

The steepness of the $M_{\rm str} - V_{\rm max}$ relation implies that all field dwarf galaxies live in a norrow range of $V_{\rm max}$. Dashed curve is a fit to the median $M_{\rm str} - V_{\rm max}$ relation of the field galaxies, derived using galaxies with $M_{\rm str} > 10^5\,{\rm M_\odot}$ and extrapolated to lower masses. According to this relation, all field dwarf galaxies with stellar mass below 10^7 live in haloes with $V_{\rm max} \sim 20 - 35\,{\rm km\ s^{-1}}$. Reionization at the early Universe prevents star formation to occure in haloes less massive than $V_{\rm max} \sim 20\,{\rm km\ s^{-1}}$ (Sawala et al., 2015).

APOSTLE satellites, on the other hand, show a large scatter in $M_{\rm str} - V_{\rm max}$

[5]field galaxies refer to the central subhalo of any FoF halo, which is located further than 300 kpc from either of the primaries, but is not further than 2 Mpc from the midpoint between the two. Satellites alternatively refer to subhaloes located within 300 kpc of either of primaries.

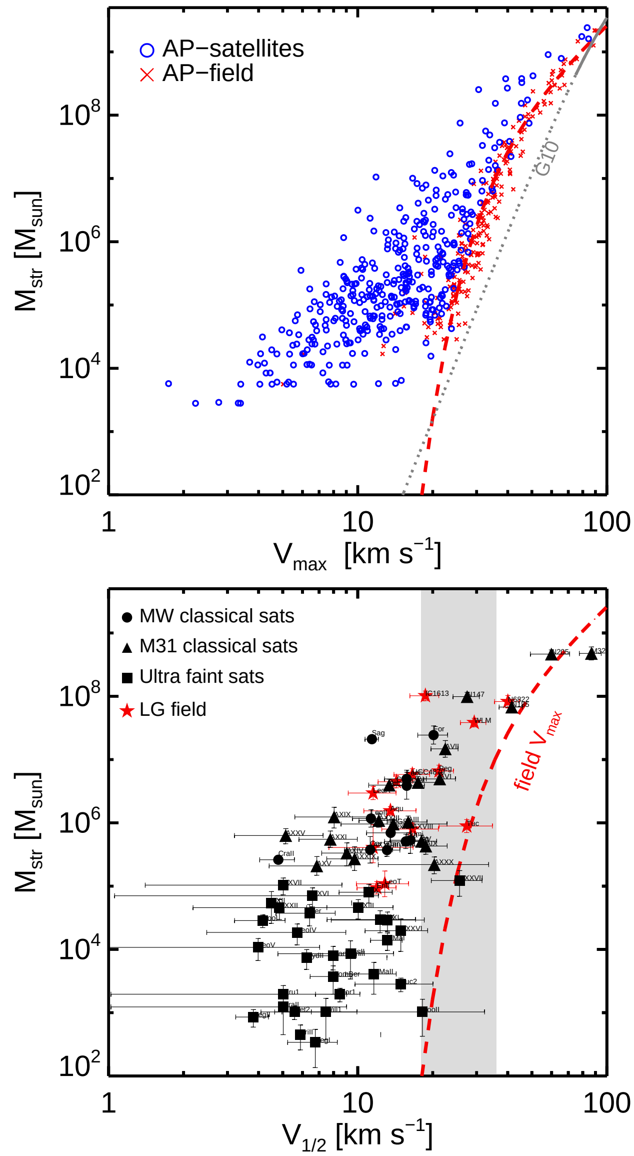

Figure 4.1 *Top:* Stellar mass versus the maximum circular velocity ($V_{\rm max}$) of field and satellite galaxies (at $z = 0$ for both) in APOSTLE, shown as red crosses and blue circles, respectively. The offset between field and satellite galaxies is due to mass loss, mostly dark matter, caused by tidal stripping. The red dashed line is the fit to the field galaxies' $M_{\rm str} - V_{\rm max}$ relations of the form $M_{\rm str}/\,{\rm M}_{\odot} = M_0\,\nu^{\alpha}\exp(-\nu^{\gamma})$, where ν is the velocity in units of 50 km s^{-1}, and (M_0, α, γ) equal to $(3.0\times10^8, 3.36, -2.4)$). The grey dotted line represent the power-law extrapolation of Guo et al. (2010) abundance-matching relation. *Bottom*: Stellar mass versus circular velocity at the half light radius ($V_{1/2}$), derived from the stellar velocity dispersions, of LG dwarfs. MW and M31 classical satellites, and ultra faint ones are shown as circle, triangle, and square symbols, respectively. The LG field dwarfs (i.e. $r_{\rm LG} > 1500$ kpc) are represented as red stellar symbols. The dashed red line is repeated from the top panel. The shaded area marks the $V_{\rm max}$ range of simulated field dwarfs with stellar mass in the range $10^7 - 10^2\,{\rm M}_{\odot}$.

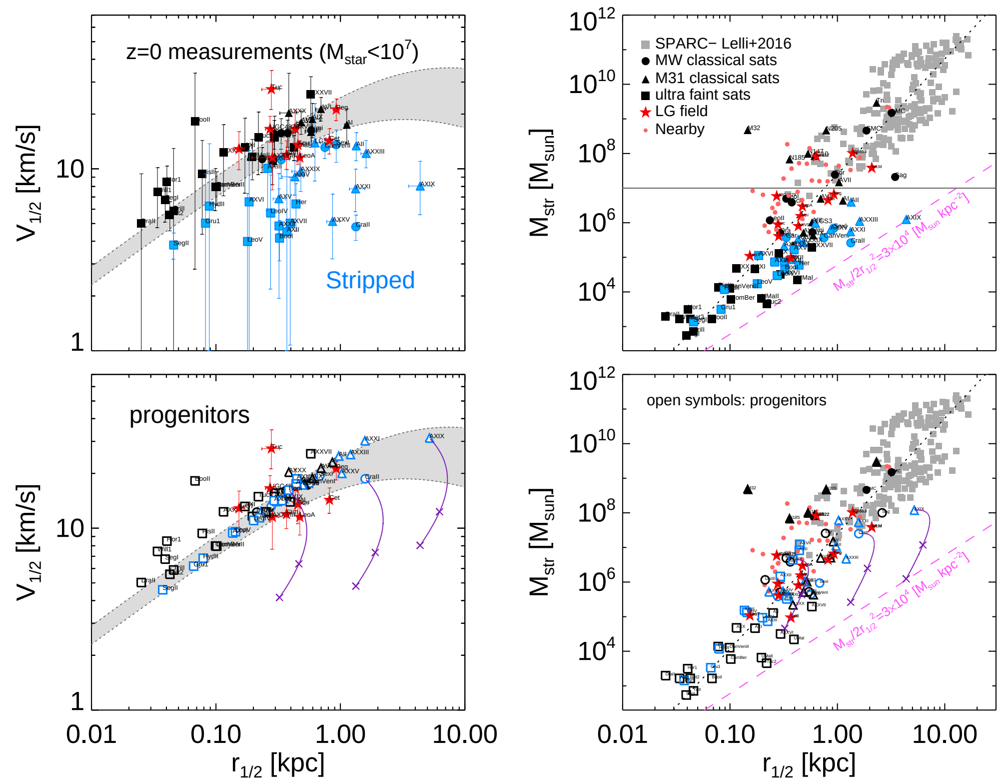

Figure 4.2 *Top-Left*: $V_{1/2}$ of the LG dwarfs with stellar mass below $M_{\rm str} = 10^7\,{\rm M}_\odot$, versus their $r_{1/2}$. The shaded area which is encompassed by two NFW rotation curves of $V_{\rm max} = 20, 36\,{\rm km\ s}^{-1}$, corresponds to the marked range in Fig. 4.1. Symbols types are the same as previous figure. Satellites lying below the shaded area are predicted to have lost their mass through stripping, and are marked with blue. LG Field dwarfs, except for the outlier Tucana, lie on the shaded area and are consistent with the APOSTLE predictions. *Top-Right*: $M_{\rm str} - r_{1/2}$ relation of observed galaxies from the sample of SPARC late type galaxies (Lelli et al., 2016), and dwarfs in and around the LG. Symbol types are similar to the previous figure, with the addition of small red circles and grey squares representing nearby dwarf galaxies and the SPARC sample, respectively. The stripped satellites, marked as blue, follow a trend below the isolated dwarfs such that their stellar mass is on average lower at a given radius. The dashed magenta line indicates a constant effective surface brightness limit. *Bottom-Left*: The same as top-left but for the progenitors (see Sec. 4.5.2.1). The purple curves are three examples of tidal stripping tracks (Peñarrubia et al., 2008), connecting the present day measurement at one end to the progenitor at the other end. The crosses on the curves mark decrease of stellar mass by 1 and 2 orders of magnitude. By construction, $V_{1/2}$ of progenitors lie close to the shaded area. *Bottom-Right*: The same as top-right, but for the the satellites we show their progenitors instead, as open symbols. $M_{\rm str} - r_{1/2}$ relation of field galaxies and progenitors are in very good agreement. Since we did not use any constraints on the $M_{\rm str} - r_{1/2}$ relation when finding the properties of the progenitors, the agreement between progenitors and field galaxies is an independent support for our predictions.

relation, and they are living in lower mass haloes compared to field dwarfs at a given stellar mass. This is the result of tidal stripping as the stellites orbit their hosts. Due to the larger extent of the DM halo, DM is more suceptible to stripping at first, compared to stars. Satellites, therefore, move horizontally to the left on the $M_{\rm str} - V_{\rm max}$ plane, before stripping becomes extreme and the satellites start to lose theirs stars. The further the satellite from the $M_{\rm str} - V_{\rm max}$ relation of fields, the more mass it has lost.

Bottom panel of Fig. 4.1, shows stellar mass of LG dwarfs vs their $V_{1/2}$ (where velocity dispersion is available). Black and red symbols correspond to the satellites and field LG members, repsectively. For comparison, the fit from the top panel is repeated here. Consistent with APOSTLE predictions, $V_{1/2}$ of the observed galaxies is always lower than the $V_{\rm max}$ of APOSTLE field dwarfs at a fixed stellar mass. [6] The only exception is M32, which is a compact elliptical galaxy and does not have any counterpart in APOSTLE.

$V_{1/2}$ of any given dwarf can be to the left of the $V_{\rm max}$ curve for two reasons. First, $r_{1/2}$ is small compared to the radius of $V_{\rm max}$, $r_{\rm max}$, and therefore $V_{1/2}$ probes rising part of the rotation curve. Second, tidal stripping has lowered $V_{1/2}$ by removing mass from the dwarf. We predict the former to be the case for isolated LG field dwarfs. For satellites, a combination of the two scenarios can play a role for their low $V_{1/2}$.

To investigate these two scenarios further, the top-left panel of Fig. 4.2 shows $V_{1/2}$ at $r_{1/2}$ of LG dwarfs with stellar mass below $10^7\,{\rm M}_\odot$. Red star symbols correspond to LG field dwarfs, while the rest represent MW and M31 satellites. According to APOSTLE predictions, all these galaxies should live in a narrow range of halo mass with $V_{\rm max} = 20 - 36\,{\rm km\ s^{-1}}$ (the shaded region in Fig. 4.1), *if* they are not stripped. The rotation curves of $V_{\rm max} = 20$ and $36\,{\rm km\ s^{-1}}$ haloes are shown in the top-left panel of Fig. 4.2 as dotted curves. If galaxies are not stripped, their $V_{1/2}$ and $r_{1/2}$ are expected to follow the grey shaded region. LG field galaxies are, indeed, consistent with this prediction and lie on the grey area, except for Tuc whose velocity dispersion surpasses this prediction, and can be problematic for our model.

One can note that there is no correlation between $V_{1/2}$ and $r_{1/2}$ for the satellites

[6] We do not show the $V_{1/2}$ or velocity dispersion of APOSTLE here for two reasons. One is related to resolution; the majority of the LG satellites have stellar masses below $10^6\,{\rm M}_\odot$. Simulated satellites in that regime are resolved with less than 100 star particles, and therfore their sizes and velocity dispersins are not reliable. Additionally, the eqution of state of star-forming gas in the subgrid physics model of APOSTLE/EAGLE prevents galaxies to be smaller than ~ 400 pc. Therefore, the size of faintest simulated galaxies are artifically larger. Therefore, their velocity dispersin or $V_{1/2}$ is not accurate (Crain et al., 2015; Campbell et al., 2016).

population; while a fraction of them follow the grey shaded area, a significant number of them lie below the shaded area. The latter population, marked as blue, must have lost its mass through tidal stripping according to our predictions. Extreme examples include Cra II and And XIX with large half-light radii and very small velocity dispersions. It is also worth noting that none of the satellites lie above the $V_{\rm max} = 30\,{\rm km\ s^{-1}}$ rotation curve if the uncertainties in $V_{1/2}$ is taken into account, in agreement with APOSTLE prediction.

Peñarrubia et al. (2008, P08 hereafter) have shown that tidal stripping of galaxies embedded in cuspy NFW haloes does not change their half light radius significantly (see also, Errani et al., 2015). In fact tidal stripping can remove 99 per-cent of stellar mass but changes the half-light radius by only a factor of 2. Therefore, we can test the stripping scenario as the origin of low $V_{1/2}$ satellites (blue symbols) by comparing their sizes to isolated and unstripped galaxies. The top-right panel of Fig. 4.2 shows stellar masses versus half-light radii of LG field and satellite members, nearby galaxies, and late type galaxies of the SPARC sample[7] from Lelli et al. (2016). Despite the general trend between half-light radii and stellar masses, there is a significant scatter in size at a fixed stellar mass, in particular around $M_{\rm str} = 10^5 - 10^7 M_{\rm str}$, as noted in previous studies (see, McConnachie, 2012, and references therein). We note that the satellites marked as stripped in $V_{1/2} - r_{1/2}$ plane (blue symbols) contribute notably to the scatter. More importantly, they follow a different trend compared to more isolated galaxies (i.e. LG field, nearby galaxies and SPARC sample) such that they have lower stellar masses on average at a given half-light radius. We note that previously mentioned extreme examples, Cra II and And XIX, are amongst the extreme outliers in $M_{\rm str} - r_{1/2}$ as well. This picture is in perfect agreement with stripping being the origin of the low $V_{1/2}$ satellites.

We also note from Fig. 4.2 that most of the ultra faint dwarfs with small size are not stripped. The primary reason is that they are embedded well within the potential well of their DM haloes, given their small size. In order to change the velocity dispersion and stellar mass of a satellite, DM must also be removed within the half-light radius (P08). Therefore, in order to tidally strip small galaxies, more bound DM particles must be stripped as well. This makes the small galaxies more resilient to tides. A secondary effect is related to the surface brightness limit of detection, since stripping brings down the surface brightness by decreasing the stellar

[7]Following Lelli et al. (2016) we assume stellar mass-to-light ratio of 0.5 in 3.6 μm band for the SPARC galaxies.

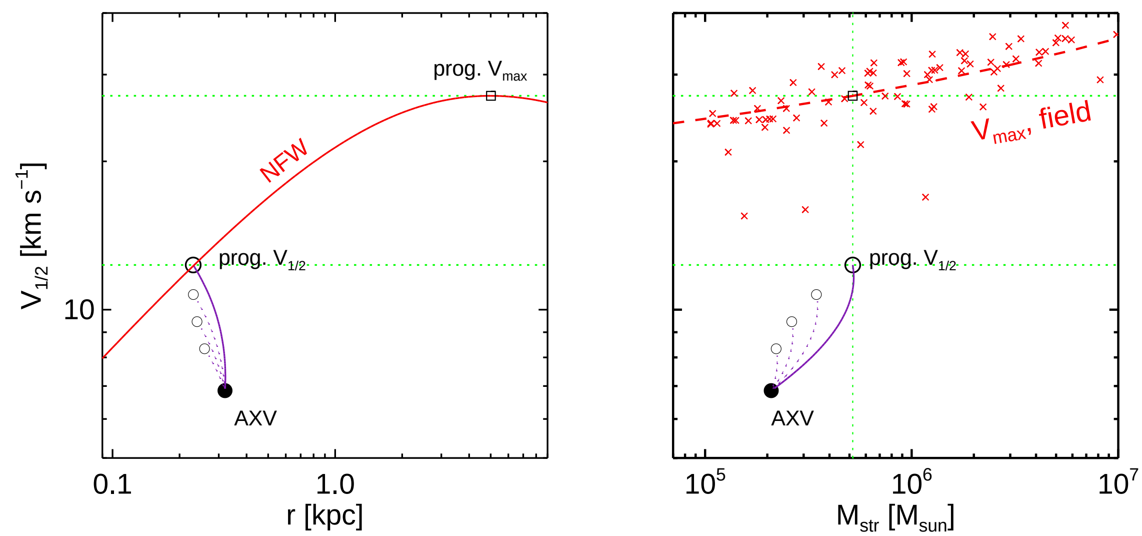

Figure 4.3 An example of finding the progenitor of a satellite, And XV, by tracking the properties of the progenitor in $V_{1/2} - r_{1/2}$ and $V_{1/2} - M_{\rm str}$ planes, according to the tracking paths derived by Peñarrubia et al. (2008). *Left*: The filled circle represents the observed properties of And XV. Each of the open circles is a potential progenitor of And XV. As they get stripped they follow the dashed curves, derived in P08, and end up at the observed values of And XV. The largest open circle represents the true progenitor to And XV; it is consistent with a $V_{\rm max} = 27\,{\rm km\ s^{-1}}$ halo. *Right*: Tidal evolutionary tracks of the same objects as the left panel, but in the $V_{1/2} - M_{\rm str}$ plane. The crosses correspond to $V_{\rm max}$ of field galaxies in APOSTLE, and the dashed line is a fit to their $V_{\rm max} - M_{\rm str}$ relation (see Fig. 4.1). Based on the fit, the stellar mass of the assigned progenitor to And XV implies a $V_{\rm max} = 27\,{\rm km\ s^{-1}}$.

mass but keeping the half-light radius almost unchanged. The dashed line on the top-right panel represents a constant surface brightness below which no galaxy has been detected so far. We can note that stripping the smallest galaxies will bring them quickly below the threshold.

In the next section we predict the properties of the progenitors of the satellites, and examine the stripping scenario in more details.

4.5.2 Satellites and their progenitors

4.5.2.1 Finding the progenitors

P08 analyzed how tides affect galaxies whose stellar density profiles follow a King model and are embedded in NFW haloes. They show that the change in the stellar mass, size, and central velocity dispersion of a galaxy due to tidal stripping, depends *only* on how much total mass is removed from the inner regions (e.g. half-light radius or king's core radius) of the progenitor; this statement is true regardless of the orbital parameters and the concentration of stars relative to the halo [8]. P08 parametrised the change in stellar mass, central velocity dispersion, and the parameters of King profile, as a function of a single parameter: the total mass loss within the king's core radius. We use these tidal evolutionary tracks to predict the properties of the progenitors of MW and M31 satellites, in particular their stellar mass, half-light radius, and velocity dispersion or $V_{1/2}$.

We are going to assume the change in $V_{1/2}$ is the same as the change in central velocity dispersion derived by P08. We also derive the change in half-light radius from the change in King model parameters given in P08.

Fig. 4.3 illustrates our method using an example, And XV. The filled circle on the left panel marks the present day observed $V_{1/2}$ and $r_{1/2}$ of And XV, while the open symbols represent potential progenitors. According to P08, tidal stripping will evolve each of the progenitors along the dashed/solid lines. Without knowing how much And XV has been stripped, one can keep increasing the mass of the progenitor, i.e. increasing $V_{1/2}^{\rm prog}$. As the potential progenitor gets more massive, its stellar mass ($M_{\rm str}^{\rm prog}$), also increases by an amount predicted by P08. This can be seen in the right panel, showing the tidal evolution in the $M_{\rm str}-V_{1/2}$ plane. The red crosses correspond to the $V_{\rm max}$ (not $V_{1/2}$) of APOSTLE field galaxies, with the dashed line being the fit to the $V_{\rm max}-M_{\rm str}$ relation.

The stellar mass of the progenitor combined with the $V_{\rm max}-M_{\rm str}$ relation can be used to predict the circular velocity of any potential progenitor at all radii, given the NFW density profile[9]. When the predicted circular velocity based on $V_{\rm max}(M_{\rm str}^{\rm prog})$ is consistent with $V_{1/2}^{\rm prog}$ at $r_{1/2}^{\rm prog}$, shown on the left panel, we consider the progenitor found. The largest open circles on both panels of Fig. 4.3 correspond to the progenitor of And XV found in our method; $V_{1/2}$ and $r_{1/2}$ of the progenitor are consistent with an NFW halo of $V_{\rm max} = 27\,{\rm km\ s^{-1}}$, expected based on the stellar mass of the progenitor and $V_{\rm max}-M_{\rm str}$ fit to APOSTLE field galaxies.

[8]Errani et al. (2015) performed similar study but with Plummer sphere profile for stellar density, embedded within Dehnen DM profile. They find a very small dependence of the tidal stripping on the concentration of the stars relative to the DM halo. This small dependence is negligible compared to the other factors which can cause uncertainty in our procedure.

[9]The NFW profile can be uniquely expressed as a function of $V_{\rm max}$ or M_{200}, since the NFW concentration, $c_{\rm NFW} \equiv R_{200}/r_{\rm s}$ is a function of M_{200} with a relatively small scatter (Ludlow et al., 2014). We adopt the $c_{\rm NFW}\,(M_{200})$ relation from Ludlow et al. (2016)

We repeat this procedure for all MW and M31 satellites with velocity dispersion measurements. For a few satellites, the procedure above would require more than two orders of magnitude of stellar mass loss from the progenitor. In such cases, we stop tracking when the progenitor is 100 times brighter, since the tidal evolutionary tracks become uncertain at extreme degrees of stripping, and also the scatter in $V_{\rm max} - M_{\rm str}$ becomes important. We are also neglecting the uncertainty in the observed properties. We note that some satellites live in haloes more massive than expected if we ignore the uncertainties in $V_{1/2}$ (note the satellites lying above the shaded area in top-left panel of Fig. 4.2). Our tracking procedure leaves these satellites unchanged.

Niederste-Ostholt et al. (2010) show that Sag dSph and its debris have combined luminosity of $10^8 L_\odot$. We use this value for the progenitor of Sag dSph, and derive $V_{1/2}$ and $r_{1/2}$ of the progenitor based on P08 tidal tracks.

We do not track the baryon dominated satellites M32, NGC 205, NGC 147, and NGC 185, due to the non-negligible effect of baryons in the inner regions of their haloes, which is not captured in our procedure. Additionally they do not have any counterparts in APOSTLE. The subgrid physics model of EAGLE/APOSTLE, prevents gas from cooling to the very centre of the DM haloes and form compact galaxies (Crain et al., 2015).

The bottom-left panel of Fig. 4.2 shows the result of our tracking procedure by presenting the progenitors of the same satellites as in the top-left panel. Symbols shapes and colours are the same as the top panel, and the LG field dwarfs are repeated. By construction, according to our method of tracking, the progenitors have higher $V_{1/2}$ and follow the grey area, i.e. they live in haloes of $V_{\rm max} = 20 - 35\,{\rm km\ s^{-1}}$. The purple curves represent tidal evolutionary paths of three examples, Cra II, And XIX, and Boo I, starting at the position of their progenitors and ending at the present day observed values. The crosses on the curves represent change of stellar mass by 1 and 2 orders of magnitude. As the progenitors lose mass through tidal stripping, their $V_{1/2}$ decreases, but $r_{1/2}$ changes by less than a factor of two even though stellar mass has changed by two orders of magnitude.

These three examples with the addition of And XXI and And XXV are the most extreme cases of stripping according to our prediction. These galaxies have lost at least 99 per-cent of their stellar mass in the past.

In the next sections, I explore the general trends observed amongst dwarf galaxies in the light of the stripping and the progenitors we predicted for them.

4.5.2.2 Stellar mass-size relation

In the bottom-right panel of Fig. 4.2 we examine how the $M_{\rm str} - r_{1/2}$ relation changes for the progenitors. Filled symbols, including LG field, nearby galaxies, and SPARC sample, are repeated from the top-right panel, while the open symbols represent the progenitors. The purple curves illustrate the tracking paths of the same three examples as in the bottom-left panel. We note that the progenitors of the stripped satellites (blue open symbols) are indistinguishable from the field galaxies. In particular the progenitors of extreme outliers in the top-right panel, such as And XIX, And XXIII, and Cra II, are now amongst the isolated objects. In other words, the same degree of stripping which places satellites in haloes of $V_{\rm max} \sim 25\,{\rm km\ s^{-1}}$, consistent with APOSTLE field $M_{\rm str} - V_{\rm max}$ relation, will move them on the $M_{\rm str} - r_{1/2}$ trend of isolated galaxies. We emphasize that our tracking procedure does not put any constraint on the $M_{\rm str} - r_{1/2}$ relation, and this result shows the success of our prediction for the satellites.

One may note that the progenitor of And XIX is still below the average relation. As mentioned earlier, we stopped tracking And XIX when the progenitor is 100 times more massive in stars. In principle the progenitor can be more massive. On the other hand, the size of this galaxy is very uncertain. There is another measurement of $r_{1/2}$ available in the literature for this galaxy which is 3 times smaller, $r_{1/2} = 1.3$ kpc. The latter measurement would place the progenitor of And XIX well within the rest of the satellites.

4.5.2.3 Metallicity trends

Dwarf galaxies are known to follow particular trends in metallicity-velocity dispersion and metellicity-stellar mass planes (Mateo, 1998). One might fear that the progenitors we are predicting will not follow these trends, in particular for the extremely stripped objects. In this section we explore these trends.

The top panel of Fig. 4.4 presents mean [Fe/H] versus $V_{1/2}$ for LG satellites and field objects. The symbol types and colours are similar to Fig. 4.2. It is clear that the stripped population (blue symbols) defined in Fig. 4.2, are not following the same trend in metallicity compared to field galaxies and the rest of the satellites. The stripped satellites have lower $V_{1/2}$ at a fixed [Fe/H]. Interestingly, $V_{1/2}$ predicted for the progenitors of the satellites is in excellent agreement with the field galaxies and decreases the scatter in $V_{1/2} - [Fe/H]$ significantly, as can be seen in the bottom

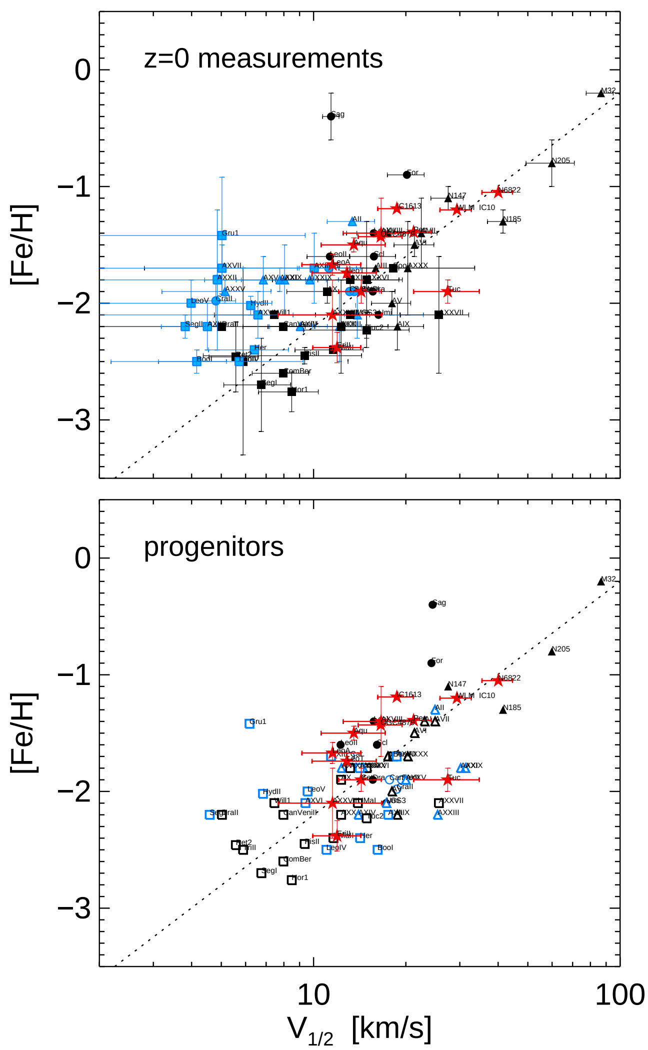

Figure 4.4 *Top*: Mean [Fe/H] versus $V_{1/2}$ of dwarf galaxies in the LG. Symbol types and colors are similar to Fig. 4.2. The stripped satellites (blue symbols), are saparated from the rest of the population, particularly the field LG galaxies (red symbols). *Bottom*: [Fe/H] vs stellar $V_{1/2}$ of the progenitors, and field galaxies. They all follow a single trend, which is much tighter, at low velocity dispersion, than the top panel. We assumed the metallicity remains constatant as the satellites get stripped. The dashed line in both panels are for guidance.

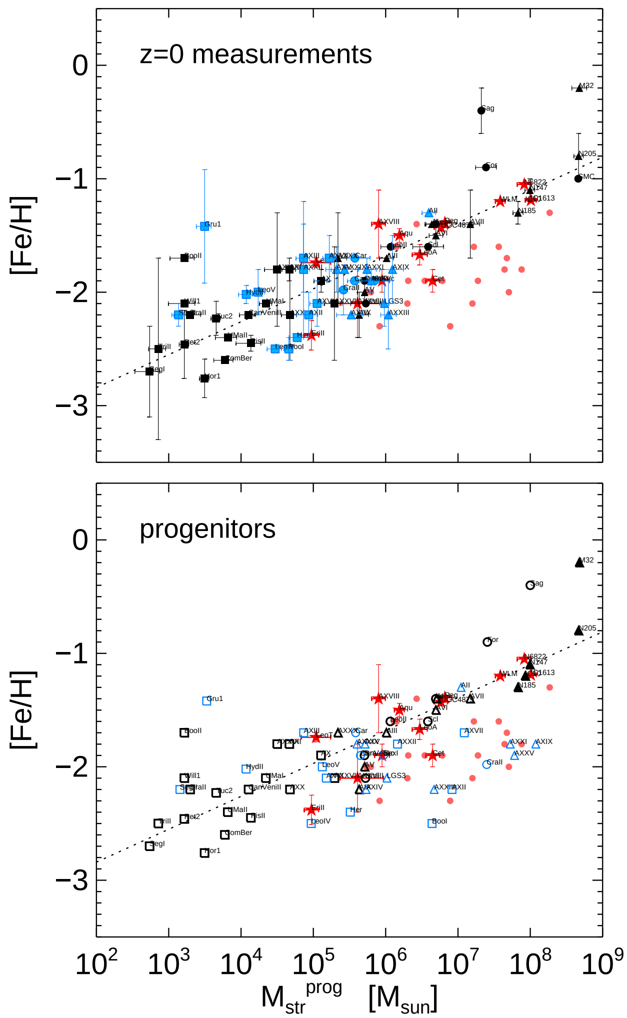

Figure 4.5 *Top*: [Fe/H] - stellar mass relation for satellites. The symbol types and colors are the same as previous figures. *Bottom*: [Fe/H] versus stellar mass of the progenitors for the satellites, and for the LG field and nearby galaxies. Metalicities are assumed constatant as the satellites get stripped.

panel of Fig. 4.4. Here we assumed the stripping does not change the median [Fe/H], and the progenitors have the same mean metallicity as the satellites, mainly for the sake of simplicity. Moreover, any other modelling for predicting the metallicity of the progenitors will be similarly uncertain. The change of metallicity is not expected to be large; metallicities of dwarf galaxies in APOSTLE change by less than ~ 0.2 dex as they get stripped, even when the satellite have lost 99 per-cent of its stellar mass.

The only galaxy which still remains far from the trend is Gru 1 with a high metallicity and low velocity dispersion.

Fig. 4.5 compares the [Fe/H]-stellar mass relation of the satellites (top panel) and their progenitors (bottom panels). The dotted line is the fit to [Fe/H]-$M_{\rm str}$ relation of LG dwarfs given in Kirby et al. (2013). We understand that Kirby et al. (2013) derive this relation for metallicities measured spectroscopically from individual stars (which in that work included MW satellites and LG field galaxies), but individual star metallicities are not available for many of the M31 satellites. Where available, average [Fe/H] from co-added spectra of stars were used for M31 satellites (Collins et al., 2013), otherwise photometric metallicities were adopted, similar to Nearby galaxies.

The stripped satellites, on the stellar mass-metallicity plane, do not appear different from the field galaxies or unstripped ones as clear as in the velocity dispersion-metallicity plane. Progenitors of the satellites, shown on the bottom panel using open symbols, follow the overall trend; even though the most extreme cases of stripping appear below the LG field, but amongst the nearby galaxies. The difference in the technique used to derive these metallicities, make interpretation of this result difficult. Except for Cra II and Boo I, the metellicity of other extremely stripped satellites were measured using the method of co-adding stellar spectra. Using their photometric metallicities, the technique used for nearby galaxies, would not change this plot, and the extremely stripped objects will still be amongst the nearby galaxies.

Considering the scatter in the stellar mass-[Fe/H] relation in Fig. 4.5 and different techniques used for [F/H] measurements, with the addition of neglecting any changes in metallicity due to stripping, we conclude that the progenitors we predict for the satellites are overall consistent with the trend. A better understanding of this relation and the agreement of our predicted progenitors with this relation can be achieved by having precise metellicity measurements for M31 satellites and other nearby galaxies using resolved stellar spectra. The metallicity gradient are also important in individual galaxies in order to understand the role of stripping on change of metallicity.

Understanding the origin of [Fe/H]-velocity dispersion and [Fe/H]-stellar mass relation of dwarfs is important for galaxy formation models. Gallazzi et al. (2006) conclude that average metellicity of elliptical galaxies correlates better with their velocity dispersion than their stellar mass. This can be understood by the deeper potential well of more massive galaxies that can retain their gas and metals. As pointed out by Kirby et al. (2013), this scenario does not work for dwarf galaxies which have small sizes and their $V_{1/2}$ does not reflect the mass of their halo. Moreover, the progenitors plotted on the bottom panel of Fig. 4.4 live in similar haloes, and their $V_{1/2}$ reflects the size of the galaxies (see bottom left panel of Fig. 4.2). Smaller $V_{1/2}$, thus, implies smaller size and living more deeply inside the potential well of the halo; one would, therefore, expect an opposite trend between metallicity and $V_{1/2}$ if it was driven by the potential depth. Given that $V_{1/2}$ is probing $r_{1/2}$ for the progenitors and there is a $r_{1/2} - M_{\rm str}$ relation, we suggest that the [Fe/H]-$V_{1/2}$ relation of the progenitors is reflecting the stellar mass-metallicity relation. A point which needs further investigations, beyond the scope of this paper.

4.5.2.4 Dynamical mass-to-light ratios

The total Mass-to-light ratios, within 3D half-light radius, of dwarf galaxies in the LG are presented in the top panel of Fig. 4.6, as a function of stellar mass. It has long been known that fainter galaxies are more dark matter dominated (see, McConnachie, 2012, and references therein). This fact sounds trivial according to the steep shape of the $V_{\rm max} - M_{\rm str}$ relation in the dwarf regime. Given the fact $M_{\rm halo}$ or $V_{\rm max}$ is not measured for dwarf galaxies and Fig. 4.6 shows the mass-to-light ratios within (3D) half-light radius, interpretation of the trend in the top panel becomes less trivial. Tidal stripping also adds to the complication.

There is no clear distinction between stripped satellites and field galaxies in the mass-to-light ratio trend. In particular extremely stripped dwarfs according to our prediction, e.g. Cra II, And XIX, and And XXI, lie in the middle of this relation around stellar mass of $10^5 - 10^6\,{\rm M}_\odot$ and $\log(2M/V) \sim -2.2$.

Bottom panel of Fig. 4.6 shows that a trend similar to the one in the top panel holds for the mass-to-light ratio of the progenitors. As pointed out by P08, the reason is behind how tidal stripping moves galaxies in this plane; purple curves show how progenitors of Cra II, And XIX, and Boo I change as they lose their mass and reach

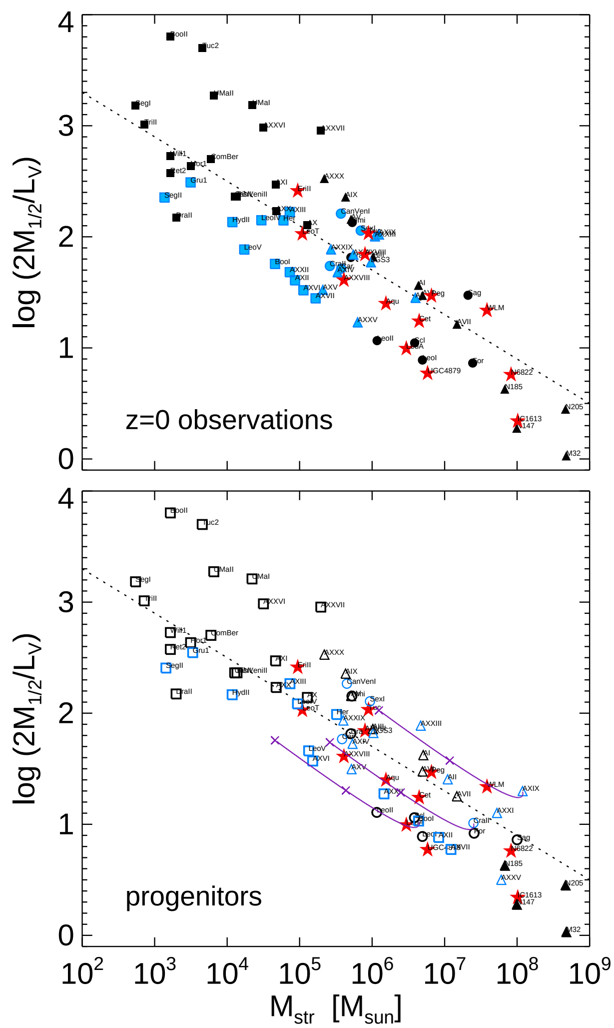

Figure 4.6 *Top*: Mass-to-light ratio versus stellar mass of the LG satellites and field dwarfs. Symbol types and colours are the same as Fig. 4.2. The stripped satellites follow the same trend as the rest of the population. *Bottom*: The same as above but for the progenitors of the satellites. The purple curves, similar to the previous figure, show the tidal stripping path of three progenitors. Since tidal stripping moves galaxies along the trend, mass-to-light ratio versus stellar trend does not change as a result of stripping.

the present day value. Stripping indeed move galaxies almost parallel to the relation and even the most extreme cases of stripping stay on the trend after loosing 99 per cent of their stellar mass.

Without the complication of tidal stripping, the trend in mass-to-light ratio versus stellar Mass is easier to understand for field/unstripped galaxies. Since all the progenitors live in similar haloes, their $V_{1/2}$ is correlated with their $r_{1/2}$. Fig. 4.2 shows that $r_{1/2}$ probes the rising part of the NFW rotation curve where the correlation has the form of $V_{\rm circ} \propto r^{1/2}$. This proportionality between $V_{1/2}$ and $r_{1/2}$ simplifies the mass-to-light ratio: $M_{1/2}/L \propto V_{1/2}^2 r_{1/2}/L \propto r_{1/2}^2/L$. Given the overall power-law correlation between stellar mass ($\sim$ luminosity) and $r_{1/2}$ shown on the right panels of Fig. 4.2, mass-to-light ratio simply becomes $M_{1/2}/L \propto L^{\alpha}$.

Based on the fit shown as the dotted line in right panels of Fig. 4.2, $\alpha = -0.4$. The relation $M_{1/2}/L \propto M_{\rm str}^{-0.4}$ is shown on both panels of Fig. 4.6 as dotted line; the zero point is arbitrary. We note that the scatter in $r_{1/2}$ at a fixed stellar mass is significant (Fig. 4.2), and it get translated into a large scatter in M/L at a fixed stellar mass. The galaxies with low stellar mass and high mass-to-light ratios which appear off the dashed line, either deviate from the $V_{1/2} \propto r^{1/2}$ trend on the bottom-left panel of Fig. 4.2 such as Boo II, or deviate from the $M_{\rm str} - r_{1/2}$ relation such as Tuc 2 and UMa I.

We conclude that our simple method of tracking satellites and find the properties is successful. It naturally explains the properties of some extreme satellites including Cra II and And XIX by associating them with extreme cases of stripping, but without changing the observed trends amongst dwarf galaxies. Our predicted progenitors actually decreases scatter in some relations including stellar mass-size (Fig. 4.2) and [Fe/H]-velocity dispersion (Fig. 4.4).

4.5.2.5 Extremely stripped satellites and their spatial distribution

As mentioned previously, according to our prediction some of the MW and M31 satellites have been highly affected by tides and lost a significant amount of stellar mass. One question that arises is that how common are such satellites in ΛCDM? Additionally, what do their orbits look like? We address these questions in this section using APOSTLE satellite population.

Te left panel of Fig. 4.7 presents stellar mass of the MW and M31 satelllites versus their progenitors, as black symbols. We additionaly show the peak of stellar mass

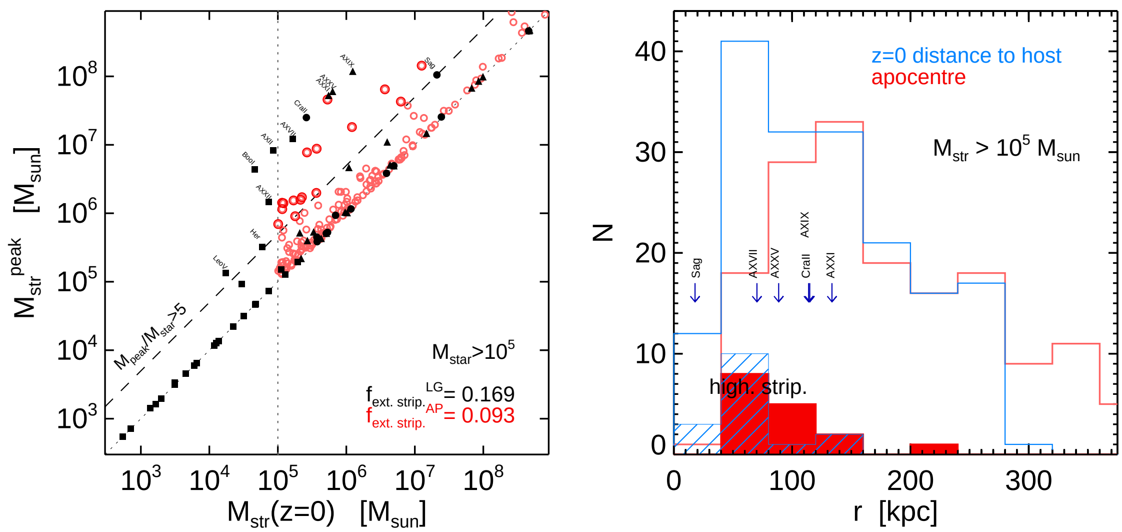

Figure 4.7 *Left*: Stellar mass of the progenitor versus present day stellar mass for APOSTLE satellites brighter than $M_{\rm str} = 10^5\,{\rm M}_\odot$ at z=0, and LG satellites, shown as red circles and black symbols respectively. For APOSTLE satellites, progenitor stellar mass is the maximum stellar mass of the main progenitor in the past. In both simulations and observations, stellar mass has not changed for most of the satellites. The dashed line marks change of stellar mass by a factor of 5, and the legend shows the fraction of satellites, with $M_{\rm str} > 10^5\,{\rm M}_\odot$, which lie above the dashed line. *Right*: The distributions for distance of APOSTLE satellites ($M_{\rm str} > 10^5\,{\rm M}_\odot$) to their host, and the apocentre of the their orbit, shown as red and blue histograms, respectively. The filled histograms correspond to the highly stripped satellites, i.e. the ones which lie above the dashed line on the left panel. The arrows mark the present day distance of highly stripped satellites of the LG to their host, the MW or M31.

for APOSTLE satellites in their lifetime, versus their $z = 0$ stellar mass. We track APOSTLE satellites back in time using merger trees and follow the main branch. Satellites of 8 primaries in four APOSTLE-L1 runs are used in this plot. Due to the resolution limit, we do not show simulated satellites with z=0 stellar mass below $10^5\,\mathrm{M}_\odot$.

Majority of the satellites both in APOSTLE and the LG, are on the one-to-one line, i.e. they have not lost a notable amount of stellar mass. The dashed line separates satellites with progenitors of at least $5\times$ more massive (in stellar mass). The fraction of satellites with $z = 0$ stellar mass greater than $10^5\,\mathrm{M}_\odot$ which lie above the dashed line in APOSTLE (darker red circles) is ~ 10 per cent on average, and it varies between 4 and 15 per cent amongst 8 primaries considered here. It is possible that resolution limits have caused underestimation of this fraction; extremely stripped objects with low mass might be left unidentified by halo finders, or their stellar mass might not be very reliable. On the other hand, the extremely stripped objects are expected to be rare; the progenitor of a $M_{\rm str} = 10^6\,\mathrm{M}_\odot$ satellites which has lost 99 per cent of its stellar mass, is a $M_{\rm str} \sim 10^8\,\mathrm{M}_\odot$ dwarf galaxy which is rare to begin with around a MW/M31 like analog, due to the shape of the stellar mass function.

According to our predicion for the LG, the fraction of highly stripped satellites (i.e. above the dashed line) with present stellar mass of $10^5\,\mathrm{M}_\odot$ or higher, is ~ 15 per cent. The highly stripped satellites in the LG include Sagatarrius dSph, Crater II, Bootes I, and Hercules around MW, and Andromeda XII, XVII, XIX, XXI, XXII, and XXV around M31.

Highly stripped satellites are expected to have multiple small pericentric passages. Proper motions, however, are not available for the highly stripped satellites of the LG, without their 6D phase-space information not much can be inferred about their orbits. We, therefore, only compare their present day distances to their host, MW and M31, with those of APOSTLE satellites.

The spatial distribution of APOSTLE satellites and their most recent apocentres are shown in the right panel of Fig.4.7 as blue and red histograms, respectively. The most recent apocentres are the most likely locations where satellites can be found, due to the longer time they spend around the apocentre. Filled histograms correspond to the highly stripped satellites in APOSTLE, i.e. peak of stellar mass is at least $5\times$ larger than the present day stellar mass. These satellites are typically located at distances below 100 kpc, but some of them are found as far 150 kpc. The median of their apocentre is at 80 kpc, and goes out to 220 kpc. Some of the highly stripped

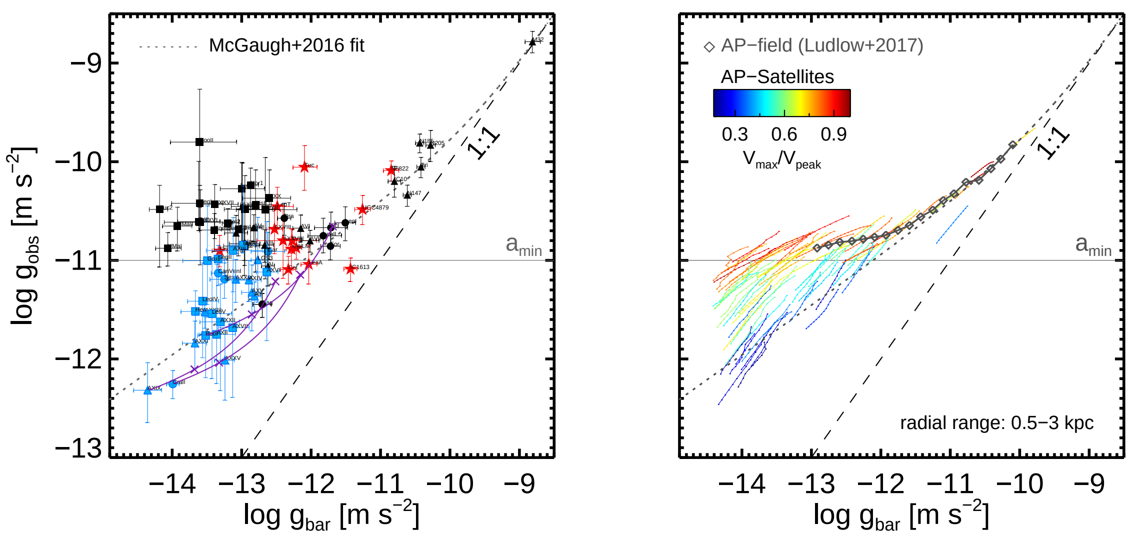

Figure 4.8 *Left*: Observed acceleration at $r_{1/2}$ vs the acceleration due to baryons, for LG satellites and field dwarfs with velocity dispersion measurements. We observe a large scatter on this plane, in contrast to the expectation from MOND, and the mass descrepancy-acceleration relation for SPARC sample of irregular/disky galaxies which follow the dotted line, fitted by McGaugh et al. (2016). Symbol types and colors are the same as previous figures. Stripped satellites (the blue symbols) present low total accelerations. *Right:* Total acceleration versus the contribution from baryons for APOSTLE satellites, in the radial range (0.5, 3) kpc. We plot a random subsample of satellites for clarity, and color code each satellite by its degree of stripping measured as $V_{\rm max}/V_{\rm peak}$. APOSTLE field galaxies follow a relatively tight correlation in this plane, plotted as grey lines with a fit to them presented by Ludlow et al. (2017). The satellites, however, introduce scatter to the MDAR, and the deviation from the relation depends on the degree of stripping.

simulated satellites which are found at large distances and large apocentres are the cases where stripping happened in another object before they fell into their primary host.

The arrows in the right panel point to the present day (3D) distances of the highly stripped satellites to the MW or M31. Since there is a stellar mass cut of $10^5\,\mathrm{M}_\odot$ for the simulated satellites, we use the same cut for the satellites of MW and M31 in this panel. The closest point to the centre is Sagitarrius dSph at the distance of 18 kpc from the Galactic centre. We do not discuss Sagitarrius here; its orbit has been studied extensively in other works, particularly using its stream (Niederste-Ostholt et al., 2010). The distance range of other highly stripped satellites to the MW or M31 is 70 to 140 kpc; even though these distances are not particularly small, stripping is still quite plausible, given the distributions of highly stripped satellites in APOSTLE (the red and blue filled histograms).

With the current available information we can not put any strong constraints on the orbits of the striped satellites of MW and M31. We can, however, predict that future measurements for proper motion of these satellites are expected to put them on relatively tight bound orbits with small, $\sim$ 20 kpc, pericentres, short periods, and early infall times. We emphasize again that such orbital characteristics are not necessary, but rather most likely, for a highly stripped satellite.

4.6 MOND versus tidal stripping in ΛCDM

4.6.1 Mass descrepancy-acceleration relation

The predictions of MOND and ΛCDM for the MDAR of low mass, low surface brightness objects are quite different. As shown by Navarro et al. (2016) and Ludlow et al. (2017), *isolated* dwarf galaxies are expected to lie at the minimun observed acceleration of $a_{\rm min} \sim 10^{-11}\,\mathrm{m\,s^{-2}}$. This is a consequence of the steep shape of the stellar mass-halo mass relation at the low mass, combined with the relatively small size of dwarf galaxies and constant central acceleration of NFW haloes. The MOND prediction for acceleration of these objects is, however, much lower than $10^{-11}\,\mathrm{m\,s^{-2}}$.

The left panel of Fig. 4.8 illutrates the MOND prediction as the dotted line in the $g_{\rm obs} - g_{\rm bar}$ plane, where $g_{\rm obs} = V_{\rm circ}^2/r$ is the centripetal acceleration and $g_{\rm bar} = G\,M_{\rm bar}/r^2$ is the contribution of baryons in the acceleration. Dwarf galaxies of the LG are also plotted in this panel based on their $V_{1/2}$, $r_{1/2}$, and $M_{\rm str}$:

$$g_{\rm obs} = V_{1/2}^2/r_{1/2}, \quad g_{\rm bar} = G\,M_{\rm str}/r_{1/2}^2 \tag{4.3}$$

There are some important points to note here: (a) the large scatter in the MDAR relation of these dwarf galaxies; (b) dSph satellites which are not stripped according to our prediction, follow a narrow range of g_{obs} just above $a_{\rm min}$, despite spanning three orders of magnitud in surface brightness; (c) stripped stallites of our prediction, marked with blue, are located below $a_{\rm min}$; and (d) cases of extreme stripping, including Cra II and And XIX, lie close to the MOND curve.

All these points are easily understood using the tidal stripping model we proposed in the previous section, combined with the predictions of Navarro et al. (2016): isolated dwarf galaxies live in a very narrow range of halo mass with $V_{\rm max} \sim 25$; given that NFW acceleration profiles are flat towards the centre, all these dwarf galaxies probe the central acceleration of a $V_{\rm max} \sim 25\,{\rm km\ s^{-1}}$ halo, $\sim a_{\rm min} \sim 10^{-11} m\,s^{-2}$, regardless of their size and stellar mass. We can see this for APOSTLE field galaxies in the right hand panel of Fig. 4.8; their MDAR relations is flat at low accelerations. We see that LG satellites which have not been stripped follow a similar trend, but with a larger scatted due to observational uncertainties. The satellite with an unusually high acceleration, Boo II, has a very large error bar on its velocity dispersion measurement, reflected here as a large uncertainty in its total acceleration.

By removing mass from the galaxies, tidal stripping moves each dwarf galaxy to accelerations below $a_{\rm min}$ and creates scatter in the original MDAR relation. Tidal stripping moves galaxies along trajectories similar to te purple curves, shown on the left panel of Fig. 4.8. These trajectories are directly derived from the ones we used previously for the change of stellar mass, $r_{1/2}$, and $V_{1/2}$ due to stripping (see bottom panels of Fig. 4.2. The same as previous figures, the purple curves connect the present day observations of Cra II, And XIX and Boo I, as three examples, to the location of their predicted progenitors. We note that the progenitors of Cra II and And XIX are located below $a_{\rm min}$. This is due to the fact that, as mentioned earlier, we stopped tracking these satellites when the progenitors were two orders of magnitude brighter. Observationals uncertainties must also be taken into account.

The right panel of Fig. 4.8 illustrates the role of stripping in creating scatter in the $g_{\rm obs} - g_{\rm bar}$ plane, by showing APOSTLE satellites. Each thin colored line corresponds to an individual satellite, where we plot $g_{\rm obs} = V_{\rm circ}^2/r$ versus $g_{\rm bar} = G\,M_{\rm bar}(< r)/r^2$ in the radial range $0.5 - 3$ kpc. The lower bound of 0.5 kpc was motivated by the

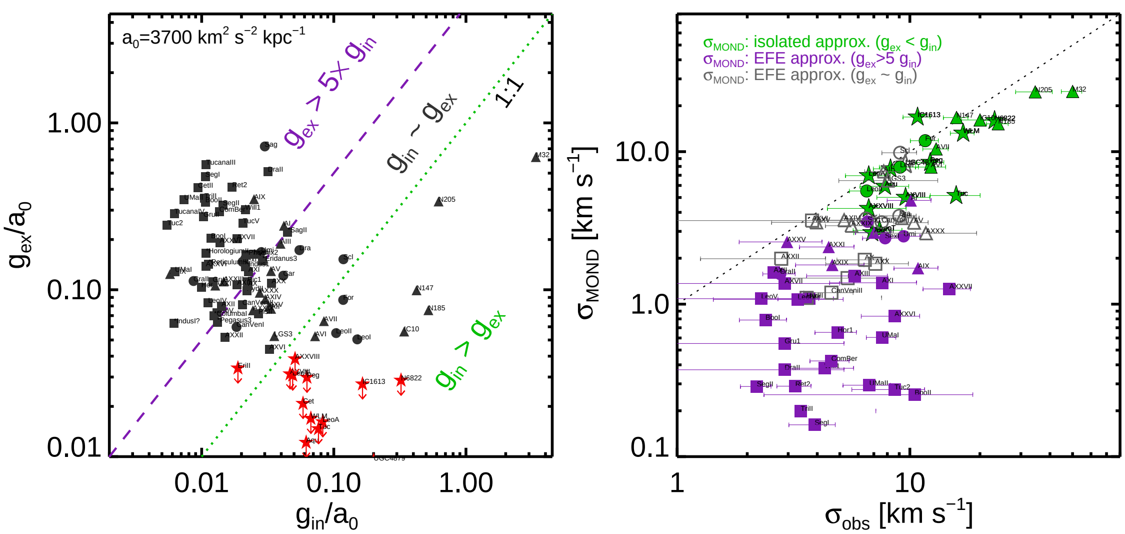

Figure 4.9 *Left*: External acceleration due to the host, $g_{\rm ex}$, versus internal acceleration, $g_{\rm in}$ of the LG dwarfs in the MOND regime. Symbol types and colors are the same as Fig. 4.1. The dashed and dotted lines divide the plane into three regions where the internal accelration is larger than the external one ($g_{\rm in} > g_{\rm ex}$), the two are comparabel ($g_{\rm in} \sim g_{\rm ex}$), and external acceleration is dominant ($g_{\rm ex} > 5 \times g_{\rm in}$). *Right*: MOND predictions for the velocity dispersion of the LG dwarfs based on their stellar mass, versus their observed velocity dispersion. For cases where $g_{\rm in} > g_{\rm ex}$, we use the isolated approximation to derive MOND velocity dispersion (green sumbols); where $g_{\rm ex} > g_{\rm in}$ we use the EFE approximation. Depending on how dominant the external acceleration is, we use filled and open purple symbols, for $g_{\rm ex} > 5 \times g_{\rm in}$ and $g_{\rm in} \sim g_{\rm ex}$, respectively.

converngence radius, defined by Power et al. (2003), of APOSTLE-L1 simulations[10], while the outer bound of 3 kpc is motivated by the largest $r_{1/2}$ of LG dwarfs. Each curve is color coded to show the degree of stripping measured by the ratio between the $z = 0$ $V_{\rm max}$ of satellites and the peak of $V_{\rm max}$ for their main progenitors, $V_{\rm max}/V_{\rm peak}$. As expected, satellites which have not been affected by tides follow the total acceleration of field galaxies, just above $a_{\rm min}$; and the more stripped ones have moved to lower accelerations and created the scatter.

An interesting point to note is that the most stripped simulated satellites are located close to the MOND prediction for MDAR. In other words there is an envelope of minimum $g_{\rm tot}$ at any given $g_{\rm bar}$ which runs close to the MOND relation. We see a similar behaviour amongst the LG satellites as well (point "d" mentioned above). This can be understood by noting the shape of the tidal stripping trajectories in the $g_{\rm obs} - g_{\rm bar}$ plane (purple curves on the left panel). Galaxies start from the relation of APOSTLE field on the right panel, and when they get striped they move along the stripping trajectories which will creat a lower edge to the $g_{\rm obs} - g_{\rm bar}$ relation of satellites. The lower edge coincides with the MOND relation.

We conclude that the overal behaviour of dwarf satellites galaxies in the $g_{\rm obs} - g_{\rm bar}$ plane can be well explained within ΛCDM framework and tidal stripping.

We observe more scatter than expected for LG field galaxies (red star symbols). Firstly, we note that the $g_{\rm bar}$ derived for LG field galaxies did not take into account their gas content, for simplicity. Given that the gas content of some of these galaxies is comparable to their stellar mass (McConnachie, 2012), their $g_{\rm bar}$ will increase at most by ~ 0.3 dex. These galaxies include IC1613, Peg dIrr, WLM, Leo A, Leo T, Aqu.

Two galaxies are real outliars compared to ΛCDM predictions: Tuc and IC 1613. We noticed in the left panels of Fig. 4.2 that velocity dispersion of Tucana is too high. Indeed it has the highest velocity dispersion of any dwarf galaxies with stellar mass below $10^7\,\mathrm{M}_\odot$. Given that its velocity dispersion is based on 20 member stars, we suggest more data should be obained to confirm its velocity dispersion. The other case, IC 1613, is a peculiar galaxy which is too close to the $g_{\rm bar} = g_{\rm obs}$ line; i.e. it has too much baryons for its circular velocity. This point has already been discussed in detail in Oman et al. (2016) using IC 1613 HI rotation curve. If enclosed mass estimates turn out to be accurate for these galaxies, their inconsistency with

[10]The Power et al. convergence radius for simulated galaxies of APOSTLE-L1, is in the range $0.5 - 1$ kpc.

APOSTLE and ΛCDM raises questions for our model of galaxy formation.

4.6.2 MOND predictions for velocity dispersion of LG dwarfs

We finally look at the MOND predictions from another angle; estimating the velocity dispersion of dwarf galaxies according to MOND. We follow the procedure of McGaugh & Milgrom (2013). Here we bring a brief summary. In the case of an isolated galaxy, the velocity dispersion is given by:

$$\sigma_{\rm iso} = (\frac{4}{81} M_{\rm str} G a_0)^{1/4} \tag{4.4}$$

where a_0 is the characteristics acceleration of MOND, $a_0 = 1.2 \times 10^{-10}\,{\rm m\,s^{-2}} \sim 3700 km^2 s^{-2} kpc^{-1}$, below which MONDian effects become considerable.

For satellite galaxies which live in the gravitational field of their host, the velocity disperion depends as well on the acceleration field of the host, known as the "external field effects" or EFEs. The importance of the EFEs for a given satellite, depends on the external acceleration due to the host compared to the internal acceleration due to the baryons contained in the satellite, $g_{\rm ex}/g_{\rm in}$. The External acceleration can be estimated as $g_{\rm ex} \sim V^2_{\rm rot,host}/d_{\rm host}$, where $V_{\rm host}$ is the circular velocity of the host at the distance of the satellite, $d_{\rm host}$. We assume flat rotation curves for the MW and M31 with $V_{\rm MW} = 220\,{\rm km\ s^{-1}}$ and $V_{\rm M31} = 230\,{\rm km\ s^{-1}}$.

The internal acceleration is given by $g_{\rm in} = 3\,\sigma^2_{\rm iso}/r_{1/2}$, where $\sigma_{\rm iso}$ is calculated from Eq. 4.4, and $r_{1/2}$ is the usual 3D (deprojected) half-light radius of the galaxy. In the regime where the external field of the host is completely dominant over the internal acceleration, the velocity dispersion of the satellite can be estimated as,

$$\sigma_{EFE} \sim (G_{\rm eff}\, M_{\rm str}/r_{1/2})^{1/2}, \quad \text{where } G_{\rm eff} \sim G\, a_0/g_{\rm ex} \tag{4.5}$$

The left panel of Fig. 4.9 shows the $g_{\rm ex}$ versus $g_{\rm in}$, in units of a_0, for all dwarf galaxies in the LG with velocity dispersion measurements available. Symbol types and colors are similar to Fig. 4.1. For the LG field galaxies, $g_{\rm ex}$ is calculated based on the distance to the nearest primary, MW or M31, and the primay rotation curve is still considered flat yielding an upper limit for $g_{\rm ex}$; hence the downward arrows for the field dwarfs.

LG field galaxies and relatively dense satellites, such as NGC 205 and M32, are in the regime where internal acceleration is dominant. For these galaxies, we use Eq. 4.4

to estimate the MOND prediction for their velocity dispersion, $\sigma_{\rm MOND}$. For most of the satellites, however, external acceleration is larger than the internal one. We use the condition $g_{\rm ex} > 5\, g_{\rm in}$, the dashed line, to distiguish between the cases where EFEs are fully dominant, and cases with comparable $g_{\rm in}$ and $g_{\rm ex}$. Eq. 4.5 can be used for the former, wherease it will not be very accurate for the latter.

The right-hand panel of Fig. 4.9 shows MOND velocity dispersion predictions versus the observed values. The filled green symbols correspond to the galaxies for which we can use Eq. 4.4 to calculate $\sigma_{\rm MOND}$ ($g_{\rm in} > g_{\rm ex}$), and the filled purple symbols are those with dominant EFEs ($g_{\rm ex} > 5\, g_{\rm in}$) where Eq. 4.5 works. We apply Eq. 4.5 to galaxies with comparabale internal and external acceleration ($g_{\rm in} \sim g_{\rm ex}$) as well, but we are cautious that this equation is not accurate for this regime and we represent these galaxies as open symbols.

For many of the galaxies, MOND prediction is inconsistent with the observed values by more than 1-sigma. In particular, almost all the ultra faint dwarfs (the square symbols) have observed velocity dispersions much higher than predicted from MOND, which is negligible due to the low stellar mass of these objects.

We note that if satellites are affected by tides at the time of observation, hence in non-equilibrium, the formalism outlined above for estimating $\sigma_{\rm MOND}$ is not applicable. Most satellites are, however, on elliptical orbits where the tidal effects are important only close to pericentric passage. The satellites reach equilibrium after their pericentric passage on a relatively short time scale compared to their orbital period. If satellites lose their stars due to tidal stripping during the pericentric passage, after they reach equilibrium the method outlined above is applicable. In order to investigate the importance of tidal effects, we compute $\alpha = [g_{\rm in}/(g_{\rm ex} r_{1/2}/d_{\rm host})]^{1/3}$ for all satellite, following Brada & Milgrom (2000). Tidal effects are important for a given satellite if $\alpha \lesssim 1$. We, however, find that $\alpha > 1$ for all the satellites we consider here. The tidal effects are therefore unlikely to be able to resolve the large discrepancy between the observed velocity dispersions and the MOND predictions shown in Fig. 4.9.

We also note that measured velocity dispersion of ultra faint dwarfs, and some of the faint M31 satelllites, are susceptible to observational uncertainties which are not accounted for in the error bars quoted in the literature (and shown in our plots), such as correction for binary stars. We, however, believe that the result shown on the right hand panel of Fig. 4.9 is qualitatively accurate given that the whole population is inconsistent with MOND predictions.

4.7 Discussion and conclusion

APOSTLE cosmological hydrodynamical simulations of LG analogs predict that isolated dwarf galaxies follow a tight stellar mass-halo mass, or equivalently stellar mass-$V_{\rm max}$, relation that is very steep in the dwarf galaxies regime. According to this relation, isolated dwarf galaxies below the stellar mass of $10^7\,{\rm M}_\odot$ live in haloes in a narrow $V_{\rm max}$ range of $25 \pm 5\,{\rm km\ s}^{-1}$, whereas satellites of the same stellar mass live in lower mass haloes due to mass loss caused by tidal stripping.

Enclosed mass within (deprojected) half-light radii of dSph satellites of MW and M31, derived from their velocity dispersions, shows that while many of them follow the mass profile of $V_{\rm max} \sim 25\,{\rm km\ s}^{-1}$ haloes, some of them lie well below this "universal" mass profile, at times significantly. These low mass satellites are predicted to be tidally stripped according to APOSTLE galaxy formation model. Additionally, the half-light radii of these low mass galaxies are on average larger for their stellar mass. In other words, their half-light radii imply a larger stellar mass, supporting the tidal stripping scenario as their origin.

We track the stellar mass, half-light radius and velocity dispersion of LG satellites back in time using the study of Peñarrubia et al. (2008), who showed that the change of these parameters due to tidal stripping, for a galaxy embedded in a NFW halo, depends only on *how much (not how)* total mass is removed from the galaxy radius. By construction, the progenitors we find for the satellites match the stellar mass-halo mass of APOSTLE field galaxies. We show that the same degree of stripping needed to explain the mass deficit of satellites relative to the universal mass profile, will bring their stellar mass-half light radius relation in agreement with the rest of the galaxies.

According to our prediction, peculiar galaxies Cra II, And XIX, XXI, XXV, have been extremely stripped and have lost about 99 per cent of their *stellar mass* in the past; the reason behind their low velocity dispersion and large half light radii. This prediction has interesting consequences. These galaxies must have fell into their hosts, MW or M31, very early on and completed a few close (i.e. < 50) pericentric passages. The stellar mass loss due to stripping must have contributed to the stellar halo of the MW and M31, and their associated stellar streams may be observable. It is possible, however, that the early infall caused the stellar streams to be dissolved into the stellar halo by present day.

If stripped in the halo of M31, we predict that And XIX must have the most prominent stellar stream; its progenitor has stellar mass of $10^8\,{\rm M}_\odot$ and 99 per cent of this stellar mass must be in the stellar halo of M31. Other highly stripped satellites around M31 include And XXI, and XXV, with progenitors of stellar mass $\sim 5 \times 10^7\,\mathrm{M}_\odot$. Around the MW, Cra II is the extreme example with a progenitor at least as bright as Fornax dSph, but the present day luminosity is comparable to Draco.

Amongst the ultra faint dwarfs of the MW, Boo I is predicted to have been highly stripped according to our method and lost 99 per cent of its stellar mass. Then Leo V and Her are predicted to have lost 80 per cent of their stellar mass. All three satellites have been observed to have tidal features around them (Collins et al., 2017; Roderick et al., 2015, 2016).

We note that the prediction for stellar streams around the MW/M31 or the orbits of highly stripped satellites, will not hold if any of these satellite was stripped before falling into the MW or M31. This scenario is possible and is seen amongst APOSTLE satellites which fell into the primaries as satellites of a third massive satellite. We note the important role that massive satellites, i.e. LMC and M33, can play amongst the satellites.

We examined the total mass-to-light ratio and metallicity relations of the progenitors we predict for the LG satellites, and conclude that our prediction is not in contradiction with the observed trends. We also show that the relatively large (~ 100 kpc) distances of the heavily stripped objects to their host, is not contradictory to their degree of stripping. APOSTLE heavily stripped satellites are found at distances as large as ~ 150 kpc from their hosts.

Without tidal stripping, the properties of satellites such as Cra II, And XIX or XXV, can not be explained easily in ΛCDM. In particular DM density cores caused by baryonic feedback can not help to explain the low mass (enclosed within half light radius) of these galaxies; they are too faint for baryonic feedback to be effective enough to alter DM distribution. DM cores produced in (some) hydrodynamical simulations so far, appeared in dwarf galaxies with stellar mass above $\sim 10^7\,\mathrm{M}_\odot$. Warm dark matter models may be consistent with galaxies with low circular velocity at half-light radius (Lovell et al., 2017), but they will have difficulty explaining the higher circular velocity galaxies. In particular, the ultra faint population of MW satellites have relatively high circular velocities. More investigation of self-interacting DM models is needed in order to test their predictions for the whole satellite population of MW and M31.

The last alternative is Modified Newtonian Dynamics, MOND. Indeed Cra II was shown to be in very good agreement with MOND McGaugh (2016); Caldwell et al.

(2017). We investigate the MOND predictions for the LG dSphs.

LG satellites show a large scatter in their mass discrepancy-acceleration relation (MDAR), in contrast with the MOND predictions. The scatter and the behaviour of satellites on the MDAR plane can be easily understood within ΛCDM combined with tidal stripping: all dwarf galaxies that are not stripped follow a small range of total acceleration around $a_{\rm min} \sim 10^{-11}\,{\rm m\,s^{-2}}$ corresponding to the characteristic central acceleration of the "universal" profile. Mass loss through tidal stripping brings the total observed acceleration of dwarf galaxies below $a_{\rm min}$ and creates scatter in their MDAR relation. we argue that tidal stripping can explain the location of satellites such as Cra II on the MDAR plane. We find LG field galaxies are consistent with APOSLE MDAR relation, except for Tuc and IC 1613.

Finally, by comparing the MOND prediction for the velocity dispersion of dSph galaxies to their observed values, we find that MOND fails for majority of the dwarf galaxies, in particular for ultra faint dwarfs. The low stellar mass of these objects would predict negligible velocity dispersion ($< 1\,{\rm km\ s^{-1}}$) for these systems, but their measured velocity dispersions are typically between ~ 5 to $\sim 10\,{\rm km\ s^{-1}}$.

We end by emphasizing that, *if* measured properties of extreme galaxies such as Cra II and And XIX, are accurate, these galaxies have to be extremely stripped in order to be consistent with ΛCDM galaxy formation framework. Therefore, these galaxies with the addition of Tuc and IC 1613 will be excellent tests for current models of galaxy formation and cosmology. Obtaining more data for these galaxies is crucial in the future.

4.8 Appendix A: the size difference of the MW and M31 satellites

McConnachie & Irwin (2006) points out the difference in the half-light radius distributions M31 and MW satellites; M31 satellites tend to be larger. New measurements have become available since then, and new dwarfs were discovered. In a more recent work (Brasseur et al., 2011) argues that the half-light radii of the MW and M31 satellite populations are statistically consistent (see, also, Tollerud et al., 2012).

We revisit this issue using the progenitors we predict for the dwarf galaxies. The top panel of Fig. 4.10 shows half-light radius versus stellar mass of MW satellites (green circles) and M31 satellites (magenta triangles) in the stellar mass range of

$M_{\rm str} = 10^5 - 10^8\,{\rm M}_\odot$ (this figure is the zoomed-in version of the left panels in Fig. 4.2). As pointed out by previous works, no correlation is seen between $r_{1/2}$ and $M_{\rm str}$ in this plot due to the large scatter in size of dwarf galaxies (see, e.g. McConnachie, 2012).

One can note the difference in the size of M31 and MW satellites, pointed out by McConnachie & Irwin (2006): half of the MW satellites are smaller than 400 pc in the stellar mass range of $M_{\rm str} = 10^5 - 10^8\,{\rm M}_\odot$, while only two of the M31 satellites are smaller than 400 pc. Interestingly, progenitors of these satellites, shown on the bottom panel, do not appear different and form a single correlation between $r_{1/2}$ and $M_{\rm str}$.

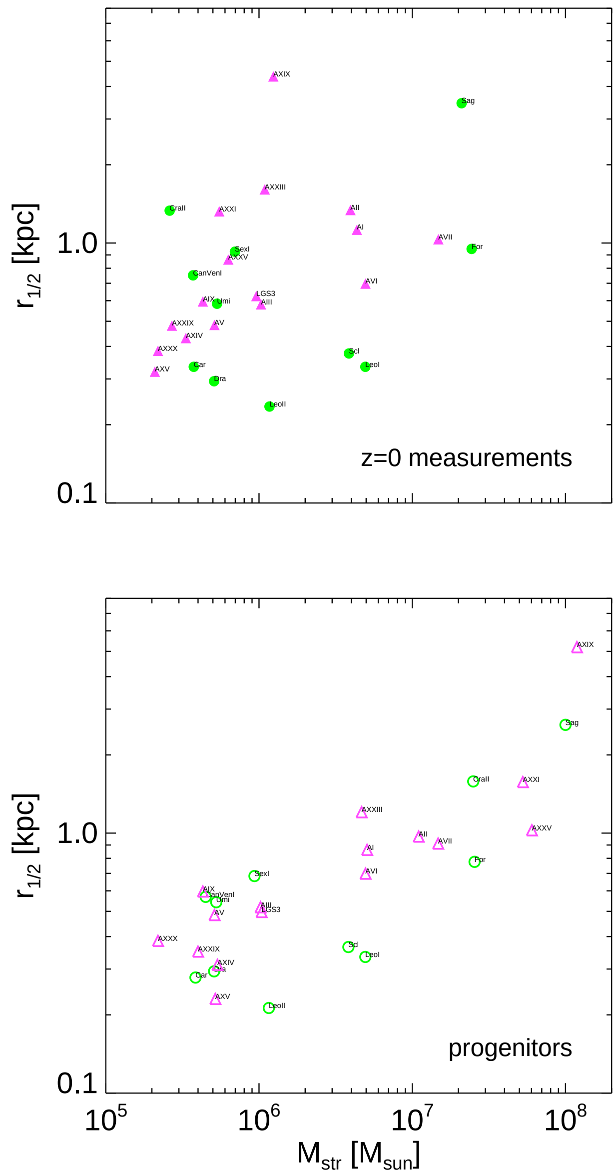

Figure 4.10 half-light radii of the MW and M31 classical dSphs (*top*) and their progenitors (*bottom*). There is no correlation in the top panel and the M31 satellites tend to be larger, whereas the progenitors of both satellite population lie on a single correlation.

Chapter 5

Conclusion

In this dissertation I address ΛCDM predictions for the mass of the LG, as well as its dwarf galaxy members, using cosmological hydrodynamical simulations.

I use large cosmological dark matter only simulations of Millennium and Millennium-II to show that the kinematic properties of the MW-M31 pair and other LG members favour a mass of $2 \times 10^{12}\,\mathrm{M}_\odot$, but with a large scatter. This mass is smaller than what is expected from the separation and relative radial velocity of the MW-M31 pairs. The small relative tangential velocity observed for the MW-M31 has an important role in bringing down the expected mass. In fact, according to the simulations, pairs with separation and radial velocity of the MW-M31 tend to have larger tangential velocities.

I use the observed kinematics of the LG members and the mass constraint of $2 \times 10^{12}\,\mathrm{M}_\odot$, to select 12 LG candidates for the high resolution, hydrodynamical simulations of the APOSTLE project. APOSTLE suite uses the subgrid galaxy formation model of EAGLE, and zoom-in techniques to simulate the LG candidates at three levels of resolutions, with the highest resolution level resolving dwarf galaxies down to the stellar mass of $10^5\,\mathrm{M}_\odot$. The simulations reproduce the luminosity function of the LG very well.

I show that the mass of classical ($M_{\rm str} > 10^5\,\mathrm{M}_\odot$) dwarf spheroidals of the MW, derived from their half-light radii and velocity dispersions, is in excellent agreement with the predictions of the simulations. This result addresses the debates raised in the past regarding the inconsistency of dwarf spheroidal masses and ΛCDM predictions. I revisit the too-big-to-fail problem and show that this problem is resolved in our simulations, without requiring to change the DM density profile to core. Four different factors play role in solving the too-big-to-fail problem, and bringing the observations and simulations into agreement: (a) the uncertainties in the mass of the dwarf were underestimated in the pas; (b) stellar mas-halo mass relation of APOSTLE is different than one ones used in the literature such as Guo et al. (2010) or Behroozi et al. (2013); (c) dwarf galaxies in hydrodynamical simulations grow into lower mass haloes compared to their dark matter only counterparts; and (d) virial mass of the MW analogs in APOSTLE are on the lower side.

Galaxy formation models within the ΛCDM predict that dwarf galaxies in isolation must inhabit haloes of $V_{\rm max} \sim 20-30\,{\rm km\ s^{-1}}$. Many of the satellites dwarf galaxies of the MW and M31, however, live in lower mass haloes. I show that these satellites are consistent with losing their mass through tidal stripping. Some of the satellites must have been tidally stripped to a large degree if they were originally living in haloes of $V_{\rm max} \sim 20-30\,{\rm km\ s^{-1}}$. The most extreme examples include Cra II, And XIX, XXI, and XXV. These galaxies must have lost almost 99 per cent of their stellar mass if their progenitors were consistent with APOSTLE field galaxies. This scenario comes with testable predictions, including (i) the extremely stripped objects must be accompanied with stellar streams; (ii) they must have stopped forming stars a long time ago; (iii) they must have had multiple small pericentric passages.

I conclude that the mass of dwarf galaxies in the LG are consistent with galaxy formation within the ΛCDM cosmology. Stellar mass-halo mass relation of APOSTLE isolated dwarf galaxies combined with tidal stripping can explain the observed mass of the LG dwarfs.

5.1 Future prospects

The predicted mass of the LG in this thesis spans a wide range. More sophisticated modelling of the dynamics around the LG is required to constrain the mass further. In particular influence of objects surrounding the LG and density field on a larger scale must be taken into account. One interesting question remaining to be answer is on the relative radial and tangential velocity of the MW-M31 pair. Their measured tangential velocity is very small, compared to what is expected from a sample of pairs chosen from cosmological simulations. There is one high tangential velocity measurement from less direct methods. More data and re-measurement of M31 tangential velocity using longer base-line is warranted.

Constraints on the mass of the LG is related to the TBTF problem as well. If the virial mass of the MW is larger than $2 \times 10^{12}\,{\rm M_\odot}$, reconciling the TBTF problem in

ΛCDM will be difficult.

The dwarf galaxies I identified as extreme cases of tidal stripping are excellent tests for the ΛCDM cosmology, or current models of galaxy formation within the ΛCDM framework. Without a significant mass loss, properties of these dwarfs can not be explained within our current knowledge of galaxy formation in ΛCDM.

An important to note is that our analysis depends highly on the measured velocity dispersion of these objects. The current measurements are not very reliable, in particular for the M31 satellites. Therefore, further observations aiming for higher number of member stars are required to confirm the previous measurements. Additionally deriving star formation histories of these dwarfs is very helpful in determining whether tidal stripping is plausible; if these galaxies went through large degrees of stripping, they must have stopped forming stars early on. Proper motion measurement for constraining the orbits and searching for stellar streams in the vicinity of these dwarfs are additional steps towards understanding the origin of these objects.

Moreover, higher resolution cosmological simulations and more advanced subgrid galaxy formation physics are needed to take the discussion forward and gain a better undestanding of the evolution of dwarf and ultra faint dwarf galaxies.

The emergence of large cosmological hydrodynamical simulations such as EAGLE and Illustris have opened up a new window in computational cosmology. I believe the next generations of the simulations (which are currently being developed) combined with more observational data will form exciting years for astrophysical research of galaxy formation; in particular, in the era of dwarf galaxies which is the most sensitive to the cosmological model and the nature of DM. Research in the particle physics and the DM particle detectors will also greatly help to discover (if any!) DM particles in the next couple of years.

Bibliography

Adams, J. J. et al. 2014, Astrophysical Journal, 789, 63

Anderson, L. et al. 2014, Monthly Notices of the RAS, 441, 24

Arraki, K. S., Klypin, A., More, S., & Trujillo-Gomez, S. 2014, Monthly Notices of the RAS, 438, 1466

Barber, C., Starkenburg, E., Navarro, J. F., McConnachie, A. W., & Fattahi, A. 2014, Monthly Notices of the RAS, 437, 959

Battaglia, G. et al. 2005, Monthly Notices of the RAS, 364, 433

Bean, A. J., Ellis, R. S., Shanks, T., Efstathiou, G., & Peterson, B. A. 1983, Monthly Notices of the RAS, 205, 605

Bechtol, K. et al. 2015, Astrophysical Journal, 807, 50

Behroozi, P. S., Marchesini, D., Wechsler, R. H., Muzzin, A., Papovich, C., & Stefanon, M. 2013, Astrophysical Journal, Letters to the Editor, 777, L10

Belokurov, V., Irwin, M. J., Koposov, S. E., Evans, N. W., Gonzalez-Solares, E., Metcalfe, N., & Shanks, T. 2014, Monthly Notices of the RAS, 441, 2124

Belokurov, V. et al. 2007, Astrophysical Journal, 654, 897

Benson, A. J., Bower, R. G., Frenk, C. S., Lacey, C. G., Baugh, C. M., & Cole, S. 2003, Astrophysical Journal, 599, 38

Benson, A. J., Cole, S., Frenk, C. S., Baugh, C. M., & Lacey, C. G. 2000, Monthly Notices of the RAS, 311, 793

Benson, A. J., Lacey, C. G., Baugh, C. M., Cole, S., & Frenk, C. S. 2002, Monthly Notices of the RAS, 333, 156

Bertschinger, E. 1985, Astrophysical Journal, Supplement Series, 58, 39

Blumenthal, G. R., Pagels, H., & Primack, J. R. 1982, Nature, 299, 37

Boesgaard, A. M. & Steigman, G. 1985, Annual Review of Astronomy and Astrophysics, 23, 319

Bond, J. R., Efstathiou, G., & Silk, J. 1980, Physical Review Letters, 45, 1980

Bosma, A. & van der Kruit, P. C. 1979, Astronomy and Astrophysics, 79, 281

Bovy, J. & Rix, H.-W. 2013, Astrophysical Journal, 779, 115

Boyarsky, A., Ruchayskiy, O., & Iakubovskyi, D. 2009, "J. Cosmology Astropart. Phys.", 3, 005

Boyarsky, A., Ruchayskiy, O., Iakubovskyi, D., & Franse, J. 2014, Physical Review Letters, 113, 251301

Boylan-Kolchin, M., Besla, G., & Hernquist, L. 2011a, Monthly Notices of the RAS, 414, 1560

Boylan-Kolchin, M., Bullock, J. S., & Kaplinghat, M. 2011b, Monthly Notices of the RAS, 415, L40

— 2012, Monthly Notices of the RAS, 422, 1203

Boylan-Kolchin, M., Bullock, J. S., Sohn, S. T., Besla, G., & van der Marel, R. P. 2013, Astrophysical Journal, 768, 140

Boylan-Kolchin, M., Springel, V., White, S. D. M., Jenkins, A., & Lemson, G. 2009, Monthly Notices of the RAS, 398, 1150

Brada, R. & Milgrom, M. 2000, Astrophysical Journal, 541, 556

Brasseur, C. M., Martin, N. F., Macciò, A. V., Rix, H.-W., & Kang, X. 2011, Astrophysical Journal, 743, 179

Brooks, A. M. & Zolotov, A. 2014, Astrophysical Journal, 786, 87

Bulbul, E., Markevitch, M., Foster, A., Smith, R. K., Loewenstein, M., & Randall, S. W. 2014, Astrophysical Journal, 789, 13

Bullock, J. S., Kravtsov, A. V., & Weinberg, D. H. 2000, Astrophysical Journal, 539, 517

Caldwell, N. et al. 2017, Astrophysical Journal, 839, 20

Campbell, D. J. R. et al. 2016, ArXiv e-prints

Cautun, M., Frenk, C. S., van de Weygaert, R., Hellwing, W. A., & Jones, B. J. T. 2014, Monthly Notices of the RAS, 445, 2049

Chan, T. K., Kereš, D., Oñorbe, J., Hopkins, P. F., Muratov, A. L., Faucher-Giguère, C.-A., & Quataert, E. 2015, Monthly Notices of the RAS, 454, 2981

Cole, S. 1991, Astrophysical Journal, 367, 45

Collins, M. L. M. et al. 2013, Astrophysical Journal, 768, 172

— 2014, Astrophysical Journal, 783, 7

Collins, M. L. M., Tollerud, E. J., Sand, D. J., Bonaca, A., Willman, B., & Strader, J. 2017, Monthly Notices of the RAS, 467, 573

Corbelli, E., Thilker, D., Zibetti, S., Giovanardi, C., & Salucci, P. 2014, Astronomy and Astrophysics, 572, A23

Crain, R. A. et al. 2015, Monthly Notices of the RAS, 450, 1937

Creasey, P., Sameie, O., Sales, L. V., Yu, H.-B., Vogelsberger, M., & Zavala, J. 2017, Monthly Notices of the RAS, 468, 2283

Davis, M., Efstathiou, G., Frenk, C. S., & White, S. D. M. 1985, Astrophysical Journal, 292, 371

Davis, M. & Nusser, A. 2016, in IAU Symposium, Vol. 308, The Zeldovich Universe: Genesis and Growth of the Cosmic Web, ed. R. van de Weygaert, S. Shandarin, E. Saar, & J. Einasto, 310–317

Deason, A. J. et al. 2012, Monthly Notices of the RAS, 425, 2840

Di Cintio, A., Brook, C. B., Macciò, A. V., Stinson, G. S., Knebe, A., Dutton, A. A., & Wadsley, J. 2014, Monthly Notices of the RAS, 437, 415 di Cintio, A., Knebe, A., Libeskind, N. I., Yepes, G., Gottlöber, S., & Hoffman, Y. 2011, Monthly Notices of the RAS, 417, L74

Dicke, R. H., Peebles, P. J. E., Roll, P. G., & Wilkinson, D. T. 1965, Astrophysical Journal, 142, 414

Dolag, K., Borgani, S., Murante, G., & Springel, V. 2009, Monthly Notices of the RAS, 399, 497

Drlica-Wagner, A. et al. 2015, Astrophysical Journal, 813, 109

Ellis, J., Hagelin, J. S., Nanopoulos, D. V., Olive, K., & Srednicki, M. 1984, Nuclear Physics B, 238, 453

Errani, R., Peñarrubia, J., & Tormen, G. 2015, Monthly Notices of the RAS, 449, L46

Fattahi, A. et al. 2016a, Monthly Notices of the RAS, 457, 844

Fattahi, A., Navarro, J. F., Sawala, T., Frenk, C. S., Sales, L. V., Oman, K., Schaller, M., & Wang, J. 2016b, ArXiv e-prints

Ferrero, I., Abadi, M. G., Navarro, J. F., Sales, L. V., & Gurovich, S. 2012, Monthly Notices of the RAS, 425, 2817

Forero-Romero, J. E., Hoffman, Y., Bustamante, S., Gottlöber, S., & Yepes, G. 2013, Astrophysical Journal, Letters to the Editor, 767, L5

Frenk, C. S., White, S. D. M., Davis, M., & Efstathiou, G. 1988, Astrophysical Journal, 327, 507

Gallazzi, A., Charlot, S., Brinchmann, J., & White, S. D. M. 2006, Monthly Notices of the RAS, 370, 1106

Gao, L., De Lucia, G., White, S. D. M., & Jenkins, A. 2004, Monthly Notices of the RAS, 352, L1

Garrison-Kimmel, S., Boylan-Kolchin, M., Bullock, J. S., & Lee, K. 2014, Monthly Notices of the RAS, 438, 2578

Garrison-Kimmel, S., Rocha, M., Boylan-Kolchin, M., Bullock, J. S., & Lally, J. 2013, Monthly Notices of the RAS, 433, 3539

Gómez, F. A., Besla, G., Carpintero, D. D., Villalobos, Á., OrsquoShea, B. W., & Bell, E. F. 2015, Astrophysical Journal, 802, 128

González, R. E., Kravtsov, A. V., & Gnedin, N. Y. 2014, Astrophysical Journal, 793, 91

Gottloeber, S., Hoffman, Y., & Yepes, G. 2010, ArXiv e-prints

Governato, F., Baugh, C. M., Frenk, C. S., Cole, S., Lacey, C. G., Quinn, T., & Stadel, J. 1998, Nature, 392, 359

Governato, F. et al. 2012, Monthly Notices of the RAS, 422, 1231

Grand, R. J. J. et al. 2017, Monthly Notices of the RAS, 467, 179

Guo, Q., Cole, S., Eke, V., & Frenk, C. 2011, Monthly Notices of the RAS, 417, 370

Guo, Q., Cooper, A. P., Frenk, C., Helly, J., & Hellwing, W. A. 2015, Monthly Notices of the RAS, 454, 550

Guo, Q., White, S., Li, C., & Boylan-Kolchin, M. 2010, Monthly Notices of the RAS, 404, 1111

Hammer, F., Puech, M., Chemin, L., Flores, H., & Lehnert, M. D. 2007, Astrophysical Journal, 662, 322

Helmi, A., White, S. D., & Springel, V. 2002, Phys. Rev. D, 66, 063502

Hopkins, P. F. 2013, Monthly Notices of the RAS, 428, 2840

Hopkins, P. F. et al. 2017, ArXiv e-prints

Irwin, M. & Hatzidimitriou, D. 1995, Monthly Notices of the RAS, 277, 1354

Jeltema, T. & Profumo, S. 2015, Monthly Notices of the RAS, 450, 2143

Jenkins, A. 2010, Monthly Notices of the RAS, 403, 1859

— 2013, Monthly Notices of the RAS, 434, 2094

Jenkins, A., Frenk, C. S., White, S. D. M., Colberg, J. M., Cole, S., Evrard, A. E., Couchman, H. M. P., & Yoshida, N. 2001, Monthly Notices of the RAS, 321, 372

Jiang, F. & van den Bosch, F. C. 2015, Monthly Notices of the RAS, 453, 3575

Kahn, F. D. & Woltjer, L. 1959, Astrophysical Journal, 130, 705

Karachentsev, I. D. & Kashibadze, O. G. 2006, Astrophysics, 49, 3

Karachentsev, I. D. & Makarov, D. A. 1996, Astronomical Journal, 111, 794

Kauffmann, G., Colberg, J. M., Diaferio, A., & White, S. D. M. 1999, Monthly Notices of the RAS, 303, 188

Kim, D. & Jerjen, H. 2015, Astrophysical Journal, Letters to the Editor, 808, L39

Kim, D., Jerjen, H., Mackey, D., Da Costa, G. S., & Milone, A. P. 2015, Astrophysical Journal, Letters to the Editor, 804, L44

Kirby, E. N., Bullock, J. S., Boylan-Kolchin, M., Kaplinghat, M., & Cohen, J. G. 2014, Monthly Notices of the RAS, 439, 1015

Kirby, E. N., Cohen, J. G., Guhathakurta, P., Cheng, L., Bullock, J. S., & Gallazzi, A. 2013, Astrophysical Journal, 779, 102

Klypin, A., Kravtsov, A. V., Valenzuela, O., & Prada, F. 1999, Astrophysical Journal, 522, 82

Koch, A., Kleyna, J. T., Wilkinson, M. I., Grebel, E. K., Gilmore, G. F., Evans, N. W., Wyse, R. F. G., & Harbeck, D. R. 2007, Astronomical Journal, 134, 566

Komatsu, E. et al. 2011, Astrophysical Journal, Supplement Series, 192, 18

Koposov, S. E., Belokurov, V., Torrealba, G., & Evans, N. W. 2015, Astrophysical Journal, 805, 130

Kravtsov, A., Vikhlinin, A., & Meshscheryakov, A. 2014, ArXiv e-prints

Laevens, B. P. M. et al. 2015a, Astrophysical Journal, 813, 44

— 2015b, Astrophysical Journal, Letters to the Editor, 802, L18

— 2014, Astrophysical Journal, Letters to the Editor, 786, L3

Leaman, R. 2012, Astronomical Journal, 144, 183

Lelli, F., McGaugh, S. S., & Schombert, J. M. 2016, Astronomical Journal, 152, 157

Li, Y.-S. & White, S. D. M. 2008, Monthly Notices of the RAS, 384, 1459

Lovell, M. R., Gonzalez-Perez, V., Bose, S., Boyarsky, A., Cole, S., Frenk, C. S., & Ruchayskiy, O. 2017, Monthly Notices of the RAS, 468, 2836

Ludlow, A. D. et al. 2017, Physical Review Letters, 118, 161103

Ludlow, A. D., Bose, S., Angulo, R. E., Wang, L., Hellwing, W. A., Navarro, J. F., Cole, S., & Frenk, C. S. 2016, Monthly Notices of the RAS, 460, 1214

Ludlow, A. D., Navarro, J. F., Angulo, R. E., Boylan-Kolchin, M., Springel, V., Frenk, C., & White, S. D. M. 2014, Monthly Notices of the RAS, 441, 378

Madau, P., Shen, S., & Governato, F. 2014, Astrophysical Journal, Letters to the Editor, 789, L17

Martin, N. F., de Jong, J. T. A., & Rix, H.-W. 2008, Astrophysical Journal, 684, 1075

Martin, N. F. et al. 2016, Astrophysical Journal, 833, 167

— 2015, Astrophysical Journal, Letters to the Editor, 804, L5

Mashchenko, S., Couchman, H. M. P., & Wadsley, J. 2006, Nature, 442, 539

Massey, R., Kitching, T., & Richard, J. 2010, Reports on Progress in Physics, 73, 086901

Mateo, M., Olszewski, E. W., & Walker, M. G. 2008, Astrophysical Journal, 675, 201

Mateo, M. L. 1998, Annual Review of Astronomy and Astrophysics, 36, 435

McConnachie, A. W. 2012, Astronomical Journal, 144, 4

McConnachie, A. W. & Irwin, M. J. 2006, Monthly Notices of the RAS, 365, 902

McConnachie et al. 2009, Nature, 461, 66

McGaugh, S. & Milgrom, M. 2013, Astrophysical Journal, 766, 22

McGaugh, S. S. 2016, Astrophysical Journal, Letters to the Editor, 832, L8

McGaugh, S. S., Lelli, F., & Schombert, J. M. 2016, Physical Review Letters, 117, 201101

McLaughlin, D. E. 1999, Astrophysical Journal, Letters to the Editor, 512, L9

Milgrom, M. 1983, Astrophysical Journal, 270, 371

Misgeld, I. & Hilker, M. 2011, Monthly Notices of the RAS, 414, 3699

Moore, B. 1994, Nature, 370, 629

Moore, B., Ghigna, S., Governato, F., Lake, G., Quinn, T., Stadel, J., & Tozzi, P. 1999a, Astrophysical Journal, Letters to the Editor, 524, L19

Moore, B., Governato, F., Quinn, T., Stadel, J., & Lake, G. 1998, Astrophysical Journal, Letters to the Editor, 499, L5

Moore, B., Quinn, T., Governato, F., Stadel, J., & Lake, G. 1999b, Monthly Notices of the RAS, 310, 1147

Moster, B. P., Naab, T., & White, S. D. M. 2013, Monthly Notices of the RAS, 428, 3121

Navarro, J. F., Benítez-Llambay, A., Fattahi, A., Frenk, C. S., Ludlow, A. D., Oman, K. A., Schaller, M., & Theuns, T. 2016, ArXiv e-prints

Navarro, J. F., Eke, V. R., & Frenk, C. S. 1996a, Monthly Notices of the RAS, 283, L72

Navarro, J. F., Frenk, C. S., & White, S. D. M. 1996b, Astrophysical Journal, 462, 563

— 1997, Astrophysical Journal, 490, 493

Navarro, J. F. et al. 2010, Monthly Notices of the RAS, 402, 21

Neto, A. F. et al. 2007, Monthly Notices of the RAS, 381, 1450

Niederste-Ostholt, M., Belokurov, V., Evans, N. W., & Peñarrubia, J. 2010, Astrophysical Journal, 712, 516

Oñorbe, J., Boylan-Kolchin, M., Bullock, J. S., Hopkins, P. F., Kereš, D., Faucher-Giguère, C.-A., Quataert, E., & Murray, N. 2015, Monthly Notices of the RAS, 454, 2092

Oh, S.-H., Brook, C., Governato, F., Brinks, E., Mayer, L., de Blok, W. J. G., Brooks, A., & Walter, F. 2011, Astronomical Journal, 142, 24

Olsen, K. A. G., Zaritsky, D., Blum, R. D., Boyer, M. L., & Gordon, K. D. 2011, Astrophysical Journal, 737, 29

Oman, K. A. et al. 2015, Monthly Notices of the RAS, 452, 3650

Oman, K. A., Navarro, J. F., Sales, L. V., Fattahi, A., Frenk, C. S., Sawala, T., Schaller, M., & White, S. D. M. 2016, ArXiv e-prints

Ostriker, J. P. & Steinhardt, P. 2003, Science, 300, 1909

Palma, C., Majewski, S. R., Siegel, M. H., Patterson, R. J., Ostheimer, J. C., & Link, R. 2003, Astronomical Journal, 125, 1352

Papastergis, E., Giovanelli, R., Haynes, M. P., & Shankar, F. 2015, Astronomy and Astrophysics, 574, A113

Parry, O. H., Eke, V. R., Frenk, C. S., & Okamoto, T. 2012, Monthly Notices of the RAS, 419, 3304

Peñarrubia, J., Benson, A. J., Walker, M. G., Gilmore, G., McConnachie, A. W., & Mayer, L. 2010, Monthly Notices of the RAS, 406, 1290

Peñarrubia, J., Ma, Y.-Z., Walker, M. G., & McConnachie, A. 2014, Monthly Notices of the RAS, 443, 2204

Peñarrubia, J., Navarro, J. F., & McConnachie, A. W. 2008, Astrophysical Journal, 673, 226

Peacock, J. A. et al. 2001, Nature, 410, 169

Peebles, P. J. E. 1986, Nature, 321, 27

Peebles, P. J. E., Phelps, S. D., Shaya, E. J., & Tully, R. B. 2001, Astrophysical Journal, 554, 104

Peebles, P. J. E., Tully, R. B., & Shaya, E. J. 2011, ArXiv e-prints

Penzias, A. A. & Wilson, R. W. 1965, Astrophysical Journal, 142, 419

Piffl, T., Binney, J., McMillan, P. J., Steinmetz, M., & et al. 2014, Monthly Notices of the RAS, 445, 3133

Planck Collaboration et al. 2015, ArXiv e-prints

— 2016, Astronomy and Astrophysics, 594, A13

Pontzen, A. & Governato, F. 2012, Monthly Notices of the RAS, 421, 3464

— 2014, Nature, 506, 171

Power, C., Navarro, J. F., Jenkins, A., Frenk, C. S., White, S. D. M., Springel, V., Stadel, J., & Quinn, T. 2003, Monthly Notices of the RAS, 338, 14

Preskill, J., Wise, M. B., & Wilczek, F. 1983, Physics Letters B, 120, 127

Read, J. I., Wilkinson, M. I., Evans, N. W., Gilmore, G., & Kleyna, J. T. 2006, Monthly Notices of the RAS, 367, 387

Riess, A. G. et al. 1998, Astronomical Journal, 116, 1009

Rocha, M., Peter, A. H. G., Bullock, J. S., Kaplinghat, M., Garrison-Kimmel, S., Oñorbe, J., & Moustakas, L. A. 2013, Monthly Notices of the RAS, 430, 81

Roderick, T. A., Jerjen, H., Mackey, A. D., & Da Costa, G. S. 2015, Astrophysical Journal, 804, 134

Roderick, T. A., Mackey, A. D., Jerjen, H., & Da Costa, G. S. 2016, Monthly Notices of the RAS, 461, 3702

Rogstad, D. H. & Shostak, G. S. 1972, Astrophysical Journal, 176, 315

Rubin, V. C. & Ford, Jr., W. K. 1970, Astrophysical Journal, 159, 379

Rubin, V. C., Thonnard, N., & Ford, Jr., W. K. 1978, Astrophysical Journal, Letters to the Editor, 225, L107

Ruchayskiy, O. et al. 2016, Monthly Notices of the RAS, 460, 1390

Sales, L. V., Navarro, J. F., Abadi, M. G., & Steinmetz, M. 2007, Monthly Notices of the RAS, 379, 1464

Sales, L. V. et al. 2016, ArXiv e-prints

Sanders, R. H. & McGaugh, S. S. 2002, Annual Review of Astronomy and Astrophysics, 40, 263

Sawala, T., Frenk, C. S., Crain, R. A., Jenkins, A., Schaye, J., Theuns, T., & Zavala, J. 2013, Monthly Notices of the RAS, 431, 1366

Sawala, T. et al. 2016a, Monthly Notices of the RAS, 457, 1931

— 2015, Monthly Notices of the RAS, 448, 2941

— 2016b, Monthly Notices of the RAS, 456, 85

Sawala, T., Scannapieco, C., Maio, U., & White, S. 2010, Monthly Notices of the RAS, 402, 1599

Scannapieco, C. et al. 2012, Monthly Notices of the RAS, 423, 1726

Schaller, M., Dalla Vecchia, C., Schaye, J., Bower, R. G., Theuns, T., Crain, R. A., Furlong, M., & McCarthy, I. G. 2015a, Monthly Notices of the RAS, 454, 2277

Schaller, M. et al. 2015b, Monthly Notices of the RAS, 451, 1247

— 2015c, Monthly Notices of the RAS, 452, 343

Schaye, J. et al. 2015, Monthly Notices of the RAS, 446, 521

Schönrich, R., Binney, J., & Dehnen, W. 2010, Monthly Notices of the RAS, 403, 1829

Simon, J. D. & Geha, M. 2007, Astrophysical Journal, 670, 313

Simon, J. D. et al. 2011, Astrophysical Journal, 733, 46

Smith, M. C. et al. 2007, Monthly Notices of the RAS, 379, 755

Sohn, S. T., Anderson, J., & van der Marel, R. P. 2012, Astrophysical Journal, 753, 7

Somerville, R. S. 2002, Astrophysical Journal, Letters to the Editor, 572, L23

Sorce, J. G., Courtois, H. M., Gottlöber, S., Hoffman, Y., & Tully, R. B. 2014, Monthly Notices of the RAS, 437, 3586

Spergel, D. N. & Steinhardt, P. J. 2000, Physical Review Letters, 84, 3760

Springel, V. 2005, Monthly Notices of the RAS, 364, 1105

Springel, V., Frenk, C. S., & White, S. D. M. 2006, Nature, 440, 1137

Springel, V. et al. 2008, Monthly Notices of the RAS, 391, 1685

— 2005, Nature, 435, 629

Springel, V., White, S. D. M., Tormen, G., & Kauffmann, G. 2001a, Monthly Notices of the RAS, 328, 726

Springel, V., Yoshida, N., & White, S. D. M. 2001b, New Astronomy, 6, 79

Stinson, G. S., Brook, C., Macciò, A. V., Wadsley, J., Quinn, T. R., & Couchman, H. M. P. 2013, Monthly Notices of the RAS, 428, 129

Strigari, L. E., Bullock, J. S., Kaplinghat, M., Simon, J. D., Geha, M., Willman, B., & Walker, M. G. 2008, Nature, 454, 1096

Strigari, L. E., Frenk, C. S., & White, S. D. M. 2010, Monthly Notices of the RAS, 408, 2364

— 2017, Astrophysical Journal, 838, 123

Tegmark, M. et al. 2004, Phys. Rev. D, 69, 103501

Teyssier, M., Johnston, K. V., & Kuhlen, M. 2012, Monthly Notices of the RAS, 426, 1808

Tollerud, E. J. et al. 2012, Astrophysical Journal, 752, 45

Tollerud, E. J., Boylan-Kolchin, M., & Bullock, J. S. 2014, Monthly Notices of the RAS, 440, 3511

Tonry, J. L., Dressler, A., Blakeslee, J. P., Ajhar, E. A., Fletcher, A. B., Luppino, G. A., Metzger, M. R., & Moore, C. B. 2001, Astrophysical Journal, 546, 681

Torrealba, G., Koposov, S. E., Belokurov, V., & Irwin, M. 2016, Monthly Notices of the RAS, 459, 2370

Trayford, J. W. et al. 2015, ArXiv e-prints

Tully, R. B. et al. 2013, Astronomical Journal, 146, 86

Tully, R. B., Rizzi, L., Shaya, E. J., Courtois, H. M., Makarov, D. I., & Jacobs, B. A. 2009, Astronomical Journal, 138, 323

Vale, A. & Ostriker, J. P. 2004, Monthly Notices of the RAS, 353, 189

van der Marel, R. P., Alves, D. R., Hardy, E., & Suntzeff, N. B. 2002, Astronomical Journal, 124, 2639

van der Marel, R. P., Fardal, M., Besla, G., Beaton, R. L., Sohn, S. T., Anderson, J., Brown, T., & Guhathakurta, P. 2012, Astrophysical Journal, 753, 8

Vera-Ciro, C. A., Helmi, A., Starkenburg, E., & Breddels, M. A. 2013, Monthly Notices of the RAS, 428, 1696

Viel, M., Becker, G. D., Bolton, J. S., Haehnelt, M. G., Rauch, M., & Sargent, W. L. W. 2008, Physical Review Letters, 100, 041304

Viel, M., Haehnelt, M. G., & Springel, V. 2010, "J. Cosmology Astropart. Phys.", 6, 015

Vogelsberger, M., Zavala, J., & Loeb, A. 2012, Monthly Notices of the RAS, 423, 3740

Vogelsberger, M., Zavala, J., Simpson, C., & Jenkins, A. 2014, Monthly Notices of the RAS, 444, 3684

Walker, M. G., Mateo, M., Olszewski, E. W., Gnedin, O. Y., Wang, X., Sen, B., & Woodroofe, M. 2007, Astrophysical Journal, Letters to the Editor, 667, L53

Walker, M. G., Mateo, M., Olszewski, E. W., Peñarrubia, J., Wyn Evans, N., & Gilmore, G. 2009a, Astrophysical Journal, 704, 1274

Walker, M. G., Mateo, M., Olszewski, E. W., Sen, B., & Woodroofe, M. 2009b, Astronomical Journal, 137, 3109

Walker, M. G. & Peñarrubia, J. 2011, Astrophysical Journal, 742, 20

Wang, J., Frenk, C. S., & Cooper, A. P. 2012a, Monthly Notices of the RAS, 366

Wang, J., Frenk, C. S., Navarro, J. F., Gao, L., & Sawala, T. 2012b, Monthly Notices of the RAS, 424, 2715

Wang, J. & White, S. D. M. 2007, Monthly Notices of the RAS, 380, 93

Wang, W., Han, J., Cooper, A., Cole, S., Frenk, C., Cai, Y., & Lowing, B. 2015, ArXiv e-prints

Watkins, L. L., Evans, N. W., & An, J. H. 2010, Monthly Notices of the RAS, 406, 264

Weisz, D. R. et al. 2011, Astrophysical Journal, 739, 5

Wetzel, A. R., Hopkins, P. F., Kim, J.-h., Faucher-Giguère, C.-A., Kereš, D., & Quataert, E. 2016, Astrophysical Journal, Letters to the Editor, 827, L23

Wheeler, C., Oñorbe, J., Bullock, J. S., Boylan-Kolchin, M., Elbert, O. D., Garrison-Kimmel, S., Hopkins, P. F., & Kereš, D. 2015, Monthly Notices of the RAS, 453, 1305

White, S. D. M. 1976, Monthly Notices of the RAS, 177, 717

White, S. D. M., Frenk, C. S., & Davis, M. 1983, Astrophysical Journal, Letters to the Editor, 274, L1

White, S. D. M. & Rees, M. J. 1978, Monthly Notices of the RAS, 183, 341

Whiting, A. B., Hau, G. K. T., Irwin, M., & Verdugo, M. 2007, Astronomical Journal, 133, 715

Willman, B. & Strader, J. 2012, Astronomical Journal, 144, 76

Wolf, J., Martinez, G. D., Bullock, J. S., Kaplinghat, M., Geha, M., Muñoz, R. R., Simon, J. D., & Avedo, F. F. 2010, Monthly Notices of the RAS, 406, 1220

Woo, J., Courteau, S., & Dekel, A. 2008, Monthly Notices of the RAS, 390, 1453

Xue, X. X. et al. 2008, Astrophysical Journal, 684, 1143

Zolotov, A. et al. 2012, Astrophysical Journal, 761, 71

Zwicky, F. 1933, Helvetica Physica Acta, 6, 110